The Pennsylvania State University

The Graduate School

Department of Mechanical and Nuclear Engineering

CHANNEL TWO-PHASE FLOW AND PHASE CHANGE IN POLYMER ELECTROLYTE FUEL CELLS

A Dissertation in

Mechanical Engineering

by

Suman Basu

Submitted in Partial Fulfillment
of the Requirements
for the Degree of

Doctor of Philosophy

December 2008

The dissertation of Suman Basu was reviewed and approved* by the following:

Chao-Yang Wang
Distinguished Professor of Mechanical Engineering
Dissertation Advisor
Chair of Committee

Fan-Bill Cheung
Professor of Mechanical and Nuclear Engineering

Daniel Haworth
Professor of Mechanical Engineering

Turgay Ertekin
Professor of Petroleum and Natural Gas Engineering

Karen A. Thole
Professor of Mechanical Engineering
Head of the Department of Mechanical Engineering

*Signatures are on file in the Graduate School

ABSTRACT

Gas-liquid two-phase flow in channels of a polymer electrolyte fuel cell (PEFC) remains a major challenge in water management. During the PEFC assembly the flexible gas diffusion layer (GDL), either carbon paper or carbon cloth, is compressed for excellent electronic and thermal contact with bipolar plates. Therefore, it intrudes into the end gas channels (i.e. channels near the tightening bolts) and cause non-uniform distribution of reactants in the PEFC. This maldistribution of flow in parallel channels decreases the ability of the flow to carry away liquid water in the intruded channels. Therefore more liquid water is accumulated in these channels and even less flow goes through, resulting in severe flow maldistribution among parallel channels

A one-dimensional analytical model based on multiphase-mixture formulation is developed in this thesis to elucidate the two-phase flow maldistribution in the cathode channels. The channels of dimensions on the order of 0.5-1 mm are considered as structured porous media. Relative humidity (RH) at the inlet and flow stoichiometry are found to be the two key parameters strongly influencing the flow maldistribution. Interestingly, our analysis shows that decreasing the inlet RH worsens flow maldistribution.

This model is then applied to a two-dimensional (extendable to three-dimension) numerical model for the cathode flow channels only. The effects of electrochemical reactions are considered in the model through uniform water injection along channels. This stand-alone channel model could simulate the liquid saturation distribution in the parallel channels as well as predict the two-phase pressure drop.

The stand-alone channel two-phase model is then integrated with a two-phase PEFC model previously developed in our laboratory. The predicted surface coverage by liquid water at the GDL-channel interface is validated against experimental results for a wide range of parameters showing excellent agreement. The anode channels are modeled using the same two-phase model, capturing the dry-wet-dry transition existing in the anode. The effect of reactant maldistribution in the gas channels is found to have important effect on the current density distribution, implying non-uniform catalyst utilization. Therefore it would almost certainly accelerate the aging of the PEFC, exacerbating the already existing low durability issue. Interestingly, the amounts of liquid water in anode and cathode channels are found to be of the same order for the whole range of parameters.

Another important physical phenomena occurring in a PEFC is liquid-vapor phase change, i.e. evaporation and condensation. To date, these phenomena have not been explored by the fuel cell community. In the present work, a two-phase, non-isothermal numerical model is used to elucidate the phase-change rate inside the cathode GDL of a PEFC. We could locate the major condensation and evaporation sites and quantify phase-change rate. Relative humidity at the inlet flow and thermal conductivity of the cathode GDL are found to have major influence on the rate of phase change. Condensation under the cooler land could be reduced substantially by decreasing the inlet relative humidity or increasing the GDL thermal conductivity. Inlet relative humidity effect is more pronounced near the inlet of the cell whereas the GDL thermal conductivity affects the phase change rate more uniformly throughout the flow length.

TABLE OF CONTENTS

LIST OF FIGURES

LIST OF TABLES

Nomenclature

A Area

C_i local concentration of species I, mol/m^3

D_i diffusion coefficient of species I, m^2/s

d diameter

I current density, A/cm^2

K Permeability of the porous media

k relative permeability of the phase

M molecular weight

mf_l^k mass fraction of species k in liquid phase

n normal direction

P pressure, Pa

S source term in the governing equations

s liquid water saturation / volume fraction

T absolute temperature, K

u velocity

V volume

x x coordinate, μm

y y coordinate, μm

z z coordinate, μm

Greek letters

α net water transport coefficient

ρ density

ε porosity

γ correction factor

κ electrolyte conductivity, S/m

λ relative mobility

σ surface tension coefficient (N/m)

ξ Stoichiometry at gas channel inlet (anode or cathode)

ν kinematic viscosity

Subscripts and superscripts

g gas phase

l liquid species

Eff effective

sat saturation

r relative

c convective correction

mem membrane

in inlet

ph phase

avg average

H_2O water

O_2 oxygen

ACKNOWLEDGEMENTS

I am indebted to my advisor Prof. Chao-Yang Wang for his constant encouragement and support throughout my PhD. I thank my other committee members Prof. Fan-Bill Cheung, Prof. Daniel C. Haworth and Prof. Turgay Ertekin for their kind considerations. Dr. Ken S. Chen's support and inputs to my research are gratefully acknowledged.

I thank all my friends and colleagues for making my stay in Penn State enjoyable and work fruitful. I am grateful to my parents and other family members for their support during harder times in past three years.

Most of all, I am indebted to my wife Devadrita for her patience, support and understanding. Without her I could not have achieved whatever little I have achieved.

Chapter 1

Introduction

The portability, compactness, high power output at low temperature and no emission issue has made Polymer Electrolyte Fuel Cell (PEFC) one of the most potential replacements for the IC Engines. High cost of the PEFC materials has made the focus of the industries shift towards fuel cell design and engineering for better performance, improved durability, cost reduction, and better cold-start characteristics. This new focus has led to an urgent need for identification, understanding, prediction, control, and optimization of various transport and electrochemical processes that occur on disparate length scales in fuel cells. Recent studies have shown that among all the transport phenomena the two-phase transport of water in a PEFC to maintain a balanced presence of water is most critical to the cell performance.

Background

The idea of generating electricity by reverse electrolysis of water was known for almost two centuries. Using a simple experimental setup, Sir William Grove demonstrated production electricity by reverse electrolysis for the first time in 1839. But the low cost and high energy density of fossil fuels had sidelined fuel cell as a viable source of energy production. In 1960s the need for a compact, lightweight and non-toxic source of electricity in the manned space orbiter of NASA rejuvenated the

once obscure Fuel Cell technology. The byproduct of the Fuel Cell even solved the problem of drinking water for the astronauts[1, 2].

PEFC technology was developed at General Electric in the early 1960 through the work of Thomas Grubb and Leonard Niedrach[1]. This early PEFC used polystyrene sulphonic acid membrane as the electrolyte. But oxidative degradation of the C-H bond of the electrolyte limited the durability of PEFC to only several hundred hours. The malfunction and poor durability of PEFC in the Gemini mission led to replacement of PEFC by Alkaline Fuel Cell in the forthcoming Apollo mission. Also low proton conductivity of the membrane necessitates a high Pt loading, thereby making PEFC extremely expensive.

But GE continued working on Proton Exchange Membrane (PEM) cells and in the mid-1970s developed PEM water electrolysis technology for undersea life support, leading to the US Navy Oxygen Generating Plant. The British Royal Navy adopted this technology in early 1980s for their submarine fleet. Other groups also began looking at PEM cells. In the late 1980s and early 1990s, Los Alamos National Lab and Texas A&M University experimented with ways to reduce the amount of platinum required for PEM cells [2]. These efforts lead to tremendous advancements PEFC technology, namely reduction of Pt loading, discovery and implementation of **Nafion**® as the membrane material. Although these improvements have brought PEFC in the competitive range of cost, still it remains near the higher end of the cost spectra[3].

In the recent years, PEFC research is approached from three points of view – cost, performance and durability. Material is the main cost in a PEFC stack and as the price of the fossil fuel soars PEFC cost will become more and more cost wise competitive.

Advanced materials usually ensure good performance at favorable operating conditions and these have been more or less achieved. But production and phase change of water in very cold operating conditions and also efficiency wise most favorable operating conditions (i.e. low current density conditions) poses a huge challenge to the commercial usage of PEFC. Last but not the least is the issue of durability. At present the durability of a PEFC stack is of the order of 1000 hours of operations while for commercialization the life expectancy should increase by one order of magnitude.

The Membrane Electrode Assembly (MEA) constitutes the major part of the cost. The most efficient catalysts known till date involve Pt or its alloys. Although the efforts made in the last decade has decreased the Pt loading by two orders of magnitude in the catalyst layers, the cost of the PEFC still remains high. As there is no known substitute for Pt in the role of catalyst, new dispersion methods are investigated to optimize the use of Pt. The cost of the membrane material **Nafion**® is very high as well. None of the potential cheaper substitute materials (e.g. Raipore, PSSA) can perform as efficiently and reliably as the **Nafion**®. Therefore research is ongoing with the aim of improving the properties of cheaper membrane materials to suit the conditions of PEFC.

Performance, in terms of current density of the PEFC has been improved more than one order of magnitude from the first operational NASA PEFC. Electrochemically enhanced electrodes and thinner membranes have increased the PEFC performance by decreasing the activation potential and ionic resistance. But then again, the preferred operating range of the PEFC is low current density operation due to its high energy efficiency. Another recent trend is low-humidity operation with the aim to simplify auxiliary equipment but not without the risk of drying out the membrane. These trends

and requirements make the water balance in PEFC of critical importance. Additionally, proper understanding of water transport would minimize the mass-transport loss and ultimately lead to a design that can avoid both flooding and dry out in all operating conditions. A smooth operation over a wide range would not only enhance the reliability of PEFC in general but also it will enhance the durability of PEFC greatly. Extremely low temperature operating condition poses another challenge of ice formation. As a significant percentage of potential users are likely to run the PEFC in such conditions, for commercial usage this is extremely important. Also, increase in volume during ice formation can potentially tear parts of membrane and catalyst layer, decreasing the durability of the PEFC.

Durability of PEFC is mainly due to the degradation of the catalyst and membrane. In this regard, the thermal and electrochemical stability of **Nafion**® has brought the durability of PEFC to the order of one thousand hours. However for a profitable production this durability should increase by one order of magnitude. The main aims in this regard are to improve the availability of Pt surface area for improved CO tolerance, better corrosion resistant material for bipolar plate. Good cell design and optimized operating conditions, which will in turn result from investigation of PEFC performance, can improve the durability significantly.

The three focuses of PEFC research outlined above are very much interrelated. In some cases improvement in one aspect results in improvement in the other aspect (e.g. optimized design of cell would enhance the durability of PEFC as well) but in some other cases improvement in one aspect might spell trouble for the other (e.g. low catalyst loading decreases cost but also reduced the CO tolerance of the cell and therefore

durability). A careful and balanced approach is necessary for the improvement in the design of PEFC. A lot of research work has been done on all three aspects. However the focus of the industry at this point is performance and durability enhancement. Performance of a PEFC depends on its transport properties and among all these, two-phase transport of water is the most important. A good water balance not only improves the cell performance but also it has profound effect on durability. Although water balance in the PEFC has been investigated extensively no effort has been made to study the liquid water transport as part of the reactant and product flow. The aim of this thesis is to understand the process and effects of two-phase water transport in the gas channels and to investigate gas-liquid phase change phenomena in PEFC.

Introduction to PEFC

Structure of a PEFC

A typical PEFC and its operation are schematically displayed in Figure **1-1.** The main structural components of a PEFC and their functions are discussed in this section.

The outermost part of the PEFC is the two bipolar plates which act as connection between two adjacent cells in a PEFC stack. The bipolar plates are grooved in the inside to form channels to distribute the reactant and remove the product from the PEFC. These plates also provide structural strength to the cell assembly. High electrical conductance, easy machinability and low density of graphite make it a suitable candidate for bipolar plate material. But its porous structure and brittleness are main drawbacks. On the other

hand steel does not have these drawbacks but it is heavy and could corrode easily. However surface coated steel could be an optimized choice.

The parts adjacent to the bipolar plates are the gas diffusion layers (GDLs)**.** The GDLs are porous media of either carbon paper or carbon cloth of thickness from 100 to 300 μm. These layers allow the reactants to diffuse evenly to the catalyst layers and form the electronic connection between bipolar plate and electrode. Usually GDLs are made hydrophobic to facilitate liquid water removal by impregnating with PTFE. Microporus Layer (MPL) is sometimes added to the inside of the GDL for making the distribution of reactant more even all along the catalyst layer. This even distribution of reactant ensures optimal use of catalyst, increasing durability and even production of water, reducing the risk of flooding with liquid water.

The catalyst layers are adjacent to the inside of the GDLs and here the electrochemical reaction takes place. These are the thinnest layer (10 μm) but costliest due to the presence of Pt catalyst. The catalyst layer consists of three phases C/Pt or Pt alloy catalyst, the ionomer and the gas phase. Carbon acts both as support of Pt catalyst and electronic conductor. The ionomer transports the proton and species transport takes place through the gas phase.

The main part of the PEFC, from which it gets its name, is the proton conducting membrane. The membrane acts as the separator to the anode and cathode flows while letting only the proton pass. **Nafion**® is the best available material for the membrane. It is characterized by hydrophobic fluorinated long main chains and hydrophilic sulfonic acid chains[3]. Chemical stability, mechanical strength, acidic nature and high proton

conductivity (due to high water absorption) are expected properties of a good membrane and **Nafion**® provides all.

Operation of a PEFC

Humidified fuel and air are fed to the PEFC through the anode and cathode gas channels respectively and the product escapes mainly through the cathode gas channels. The reactants diffuse to the catalyst layers through GDLs and the following reactions take place in the catalyst layer on the Pt surface.

Hydrogen oxidation reaction (HOR) in the anode

$$H_2 \rightarrow 2H^+ + 2e^- \quad (\mathbf{1.1})$$

Oxygen reduction reaction (ORR) in the cathode

$$O_2+4H^++4e^- \rightarrow 2H_2O \quad (\mathbf{1.2})$$

The protons reach the membrane after production in the anode catalyst layer where the membrane lets it through to the cathode catalyst layer. In the cathode catalyst layer oxygen diffuses in from the cathode gas channel through the cathode GDL and electron is conducted from the external circuit through the bipolar plate and the GDL. The oxygen reduction reaction takes place and product water is formed. In the cathode catalyst layer some water is brought from the anode with the proton due to electro-osmotic drag. But as water is being produced in the cathode catalyst layer some of it diffused back in to the anode due to the resulting water concentration gradient (back-diffusion). Produced water is carried away by both anode and cathode gas but the flow

rate of cathode being higher it can carry much more amount of water. For a good operating cell the back diffusion and electro osmotic drag should balance each other at a situation where the membrane is wet, GDLs are partially wet i.e. there is adequate water in all portions of the cell.

The electrochemical and transport process described above has three major physical resistances or limitations. First of all is the activation loss. Even the open circuit voltage is less than the theoretically calculated maximum voltage. The reason for that is the fuel crossover through the membrane resulting in an internal current. A portion of the voltage is lost in driving the reaction that transfers the electron to and from the electrode. These wastages cause loss of voltage. The ohmic drop is the linear drop of voltage as a penalty for proton transport. Ohmic loss is proportional to the current density. Finally there is mass transport loss. The cell has a limited ability of transporting different species i.e. reactants and products. At high current density required amount of species could not be transported to all the locations and product water could not be transported away, resulting in zero reactant concentration at reaction surface. This leads to a nonlinear loss in voltage. At very high current density voltage loss due to mass transport loss equals the produced voltage i.e. the cell dies.

At low current density the activation loss is the dominating factor as the proton and species transport are small. This loss is controlled by electro kinetic parameters such as reaction temperature, catalyst surface area, reaction Tafel slope and exchange current density.

With the increase in current density the ohmic losses increase and slowly this becomes the major loss of the system. Ohmic loss is mainly ascribed to the ionic

resistance as the electronic resistance is far lesser than ionic resistance. Proper hydration of cell can decrease the ohmic resistance. Water being the product species, proper water management can alleviate this loss. Thinner membranes are helpful in this regard as well.

If current density increases so much that the reaction rate exceeds the species transport rate then the mass transport limitation would dominate the PEFC performance. Diffusivity of GDL and catalyst layers, and the composition and pressure of the oxidant gas determines the mass transport limit. At high current density due to high concentration of water vapor condensation takes place and that blocks many pore spaces in the GDLs and catalyst layers, thereby decreasing the mass transport. But proper design of flow field can enhance the mass transport limitation of a PEFC.

In addition to these with time due to catalyst degradation and other irreversibility the cell performance degrades.

Two-Phase Flow in the Gas Channels

Gas-liquid, two-phase flow in channels of a (PEFC) remains a major challenge in water management. The cathodes are susceptible to flooding due to diffusion of water either formed due to ORR in the catalyst layer or electro-osmotic dragging of water from the membrane. At low temperature operations water might condense if the partial pressure of water vapor drops below vapor pressure of water at that temperature. At present fuel cells are operated under low humidity condition enough to maintain the polymer hydration. But the water transport characteristics become highly intricate under such conditions e.g. the variation in water concentration is high down the channel as the

cell is self-humidifying the inlet gases. On the other hand the flow rate in anode gas channel is much smaller and therefore its ability to flush liquid water is much lower than cathode gas channel. This makes anode channel more vulnerable to flooding. Especially in low current density and low stoichiometry operating conditions when cathodes ability to flush out liquid water is limited there is increased chance of water accumulation in the anode channels as a result of strong back-diffusion.

Channel Flooding

Channel flooding refers to a situation where a substantial fraction of liquid water accumulates in gas channels, thus causing two-phase flow and pressure drop increase and fluctuations. Experimental evidence indicated that the channel flooding is most severe at low current densities where gas velocity is low and insufficient to drain liquid water out of the fuel cell channels. Thus, channel flooding is a main cause of the mass transport loss and operational instability in the low current density and low flowrate operation. This operational regime is exceptionally important for PEFC engines due to its potential of high energy conversion efficiency.

Flow Maldistribution

In a multilayer PEFC it is important to ensure an even distribution of reactant in all the flow channels. GDL intrusion at the end channels causes an area maldistribution exacerbating the situation. Maldistribution of flow in the parallel channel leads to

profound performance and durability implications, such as (1) loss of active areas; (2) fuel starvation and hence oxygen reduction reaction on the anode side thus leading to carbon corrosion on the cathode side; and (3) O_2 starvation and hence H_2 evolution on the cathode side and furthermore H_2/O_2 reaction thus leading to hot spot formation. Directly, less flow means less reactant and hence reaction rate is non-uniform in the catalyst layer. The indirect problem is that less flow would mean less momentum and hence more susceptible to blockage due to water vapor condensation. This leads to a serious loss of efficiency of the fuel cell as the whole channel is lost due to blockage. The reason is the cycle of liquid clogging and subsequent flush out in the flooded channel. Hence for a stable fuel cell, flooding of the channels must be avoided.

Phase Change in a PEFC

Liquid-vapor phase change, or specifically evaporation/condensation, plays a pivotal role in the coupled water and thermal management of polymer electrolyte fuel cell. Water, produced in the cathode catalyst layer, is transported away through the GDL to the flow channels in both liquid and gas phase, while major part of the waste heat is transported by conduction through highly conducting bipolar plates. The coolest portion of the MEA+GDL assembly is adjacent to the bipolar plate. Thus, water vapor tends to condense over the surface of bipolar plate. This sets up a “heat-pipe” between the hot cathode catalyst layer under channels and GDL adjacent to cool bipolar plate, thereby enhancing transport of heat.

While a large body of literature exists to study two-phase transport in PEFCs analytically, experimentally and numerically, a direct examination of the phase change phenomena has been absent. This work intends to shed first light on physical characteristics and their interrelation with fuel cell operation. Another objective of this work is to prompt the development of in-situ and direct measurement of the phase change rate as an important parameter to PEFC operation.

Literature Review

Review of PEFC modeling and experiments

PEFC research demands understanding of materials science, interfacial science, transport phenomena, electrochemistry, and catalysis. A PEFC model should efficiently couple transport phenomena with electrochemical kinetics and charge transport of both electrons and ions. The modeling effort is further complicated by disparate length and time scales involved in different phenomena in the PEFC. The numerical modeling effort starts with physicochemical model development with the help of advanced and efficient algorithms. These are followed by materials characterization with the ultimate aim of model validation at detailed levels[4]. Detailed model validation has been increasingly acknowledged by the PEFC research community, because the global current-voltage curve is largely inadequate to validate comprehensive PEFC models.

Comprehensive PEFC modeling started with the one dimensional models of Bernardi and Verbugge[5] and Springer et al.[6, 7]. As a starting point they focused on MEA

and GDL. Bernardi and Verbugge[5] modeled MEA and cathode GDL with a combination of Bulter-Volmer equation for electrochemical kinetics and the Stefen-Maxwell equation for the gas-phase multi-component transport. Only hydrogen and phase potential equations were considered in the anode side. Although hydrogen and oxygen diffusion and phase potential equation was solved in the MEA, water transport was ignored there.

Detailed description of water transport in the membrane was included in Springer et al.'s [6, 7] model. They experimentally measured the water-diffusion coefficient, drag coefficient and membrane proton-conductivity as function of water content. These results were empirically included in the model to capture the water transport in the membrane as a result of molecular diffusion and electro-osmotic drag. The model, although simple and one dimensional, had the capability to capture the basic mechanism of PEFC given the experimental data.

PEFC models were extended to two-dimension by Fuller and Newman [8, 9, 10, 11] and Nguyen and White [12, 13]. Fuller and Newman computed simple water and heat transfer in two-dimensional MEA in depth and axial direction operating on reformed methanol in order to investigate water and thermal management along with fuel utilization. Nguyen and White's model included MEA, GDLs and gas channel but catalyst layers were excluded and membrane properties were extrapolated from the water activity of the adjacent anode flow. They studied the water and heat transport and the effect of membrane transport data available in literature on these.

The first three dimensional model was developed by Um et al.[14, 15] and Dutta et al. [16, 17]. Um et al.[14, 15] proposed a single domain three-dimensional model including the effect of electric potential and water transport in the membrane. This model, although

developed for simple geometry, had the capability to handle complex geometry. On the other hand Dutta et al. [16, 17] used mass fraction equations with variable density to compute mass exchange between two sides of a twenty channel serpentine fuel cell excluding the MEA. The water transport in the MEA was modeled analytically with constant transport property assumption and simple difference equations to approximate the differential equation. Their model consisted of solving difference equation in the gas channels and GDLs on both sides with coupling boundary condition for the electrochemical kinetics of the MEA. One major assumption in their model was uniform electrolyte potential and water content across the membrane. But the experimental study of Buchy and Scherer[18] and numerical quasi 3-d model of Kulikovsky[19] showed significant variation of water content across the Nafion membrane around the fully hydrated level. In the same line Meng and Wangs'[20] study indicated for thinner membranes like N112 the ionic resistance of the membrane is of the same order as that of the catalyst layer and therefore it is improper to neglect the resistance due to the catalyst layer.

Um et al. [14, 15]'s model was extended by Pasaogullari and Wang [21] to compute two-phase transport of water in the GDLs. Although water is essential for membrane ionic conductivity too much water can initiate water condensation. This liquid water was found to block the pore space of the GDLs and catalyst layers, hampering the species transport and experiments (Yang et al.[22], Zhang et al.[23]) indicated that channel clogging was a possibility (as shown in Figure **1-2)**. Given the low startup temperatures (~ 25^{o}C) for automobile applications two-phase flow is unavoidable for automobile fuel cells. Therefore understanding and prediction of this is critical for a good PEFC design. Two-phase transport in a PEFC consists of three sub modes: 1) liquid water coverage model in

catalyst layers, 2) Two-phase transport in GDL and MPLs along with the coverage model for GDL and 3) Two-phase flow in the gas channels. All the efforts of two-phase flow modeling in PEFC were on the first two sub modes (Wang et al.[24]; Natarajan and Nguyen[25]; Nam and Kaviany[26]; Mazumder and Cole[27]; Pasaogullari and Wang[28]; Bigersson et al.[29]; Meng and Wang[30]; Wang and Wang[31]; Promislow et al[32]).

Presence of liquid water in the gas channels of a PEFC makes the flow situation complicated. Wang et al.[24] s' study of two-phase flow and transport in PEFCs using two dimensional multiphase mixture model gave an estimate of a threshold current density for first appearance of water. Maharudrayya et al.[33] presented an one-dimensional analytical solution of pressure-drop for U- and Z- type parallel channels for single phase flow. This model could be used for selecting dimensions for the headers and channels to minimize the maldistribution of the gas flow at the inlet. Experimental investigation of two-phase flow pressure drop in the PEM fuel cell channels by Lee et al.[34] concluded that a friction factor closely resembling the friction factor for laminar flow in a circular channel could be used. But their investigation considered a single point injection of the liquid, which is not the case for a fuel cell channel. From experimental and numerical investigation of Barreras et al.[35], it was found that the inlet flow enters the parallel channels of a PEFC preferentially due to the formation of the recirculation bubbles at the inlet. They concluded that making the angle of the inlet header more than right angle to the parallel channels could alleviate maldistribution.

Review of two-phase flow in porous media

The only difference between a random porous medium such as GDL and a regularly structured porous medium such as gas channels lies in the pore morphology. However, it was long recognized that geometric analogy between porous media and capillary tubes could be employed to build up flow theories in irregular porous media. The highly tortuous disordered porous media were simplified as a bundle of straight capillary tubes, thus reducing the study of porous media to investigation of a two-phase flow in a single capillary tube. However two-phase nature makes it difficult to theoretically prove the exact analogy between a capillary channel and a porous medium.

The two-phase flow in geothermal processes and petroleum reservoirs poses a similar problem as the two-phase flow in the PEFC. The flow beds feature the random solid particles with two-phase flows in pores. Some of the packed beds are filled with meso-scale particles making the size of the pores for internal two-phase flow to be of the order of ~ 1mm and this dimension is similar to that of PEFC gas channels (Chaouche et al.[36]; Or and Tuller[37]; Wang et al. [24]). This type of beds could be treated as a capillary porous media along with other small-pore bed and Darcy's law could be applied as a macroscopic tool to analyze and design the two-phase flow in porous media. Therefore the Darcy law based porous medium flow theory is applicable to both types of porous media. This approach was successfully applied to develop a two-phase flow model in micro heat pipes by Wang et al.[38]; was reviewed extensively by Olbricht[39]; and was most recently applied to simulate micro-channel heat exchangers in electronics cooling by Imke[40]. In this approach called the Multiphase Mixture Model (M^2 model), all two-phase

flow features such as the liquid-gas interface and two-phase flow patterns are lumped into capillary pressure and relative permeability (Wang and Cheng[41, 42]). Thus, one must "calibrate" these two-phase flow properties before one can apply M^2 model to the channel region and simulate the liquid saturation distribution along the channel. Liquid stuck in the corners due to wall adhesion can not be flushed by flow and therefore is called irreducible liquid saturation. For liquid saturation below this value, liquid remains in several disconnected pockets in the porous media. The irreducible liquid saturation can be calculated from the empirical relations by Saez and Carbonell[43].

Since the absolute permeability of a channel could be analytically determined for only a few cross-sections, it is determined by numerical experiments as suggested by Dullien [44]. For complex channel geometries such as U-turn, pin-structured and branched flow-fields, the absolute permeability could still be computed with reasonable accuracy by CFD codes as long as the flow is laminar. Similarly, the exponent of the liquid saturation in the relative permeability correlation is obtained through numerical experiments. Brooks and Corey[45] approximated Burdine's equations depending on experimental results and came up with expressions for relative permeability that would depend only on the phase saturation and an exponent. The unknown exponent was determined by fitting a curve between capillary pressure and effective saturation. A similar process is followed in the present investigation.

To date, no model other than Wang et. al.[46] existed in the literature that can treat channel flooding. While mist flow model and film flow model was developed for the extreme cases of high gas velocity (liquid volume fraction < 0.1%) and low gas velocity/highly hydrophilic channel wall (liquid volume fraction < 10%), respectively, a

general model covering a wide range of liquid fraction and capable of capturing flow maldistribution was absent. The most urgent need in PEFC modeling was to develop a two-phase flow and flooding model for fuel cell channels, allowing the liquid water saturation to be predicted at levels as high as 20-30%. Thus, such a model will enable channel flooding, two-phase flow maldistribution in multiple, parallel channels, and the flow-field effect on liquid water removal to be captured.

The novel approach of treating fuel cell channels as a structured porous medium with straight capillary pores (Wang et. al.[46]) is continued here. The pore size is proportional to the channel dimension and is sufficiently small that the Reynolds number is small to warrant the laminar flow regime. The porous medium permeability can then be determined by hydraulic conductance of laminar flow through a flow channel of various cross sections.

Review of two-phase flow in micro channels

To ensure a uniform distribution is difficult in parallel channels, even with single-phase flow at the inlet. From their experimental investigation of single-phase flow in parallel micro-channels, Yin et al.[47] developed a pressure drop model for the whole heat exchanger. Remarkably, the Moody chart was found to be valid inside the channels. Triplett et al.[48], Damiandes and Westwater [49], and Fukano and Kariyasaki[50] extensively studied the gas liquid two-phase flow in long horizontal micro-channels with different cross sections. These situations are mostly unrealized in the fuel cells. Triplett et al [51] used the available empirical correlations (Butterworth, Lockhart and Martinelli) to compare the

experimental pressure drop with the one dimensional numerical solution. As expected the correlations could not model the separated flows (slug and annular) effectively.

Research preformed on parallel micro-channel heat-exchangers under two-phase flow is extensive. However, mostly such flows include flow boiling not the condensation. Nevertheless the flow regimes are expected to be same for similar configurations and similar flow rates. Hestroni et al.[52] studied the two-phase flow patterns in parallel micro-channels of 'Z' and 'S' configurations. The configuration in this case was similar to that of PEFC excluding the electrochemical reactions and the shape of the channels. Unlike the flow pattern in the air-water flow, the steam water flow showed explosive nucleation. At low heat fluxes micro bubbles were formed and were swept downstream, which was also confirmed by Jiang et al.[53]. At high heat flux however an unstable vapor core was formed resulting in a quasi-periodical rewetting and refilling of the channels, reported first by Kandlikar[54]. As a result the channel did not remain totally blocked. Two flow regimes were observed, droplet flow and annular flow with dynamic characteristics and that resulted in sharp pressure fluctuations. Balasubramaniam and Kandlikar[55] found that in parallel micro and mini channels dominant mode of phase change was nucleate boiling – both in bulk flow and in liquid film. An explosive growth of these bubbles caused flow reversal resulting in severe flow maldistribution. This mechanism also resulted in a fluctuating pressure drop with a single dominant frequency which increased with surface temperature i.e. increased with heat transfer. Kandlikar and Balasubramaniam[56] also showed that presence of buoyancy exacerbates the situation in downward flows by introducing a reverse flow thereby causing a severe maldistribution in the parallel channels. Lee and Mudawar[57] studied pressure drop characteristics in parallel micro-

channels of evaporators in a refrigeration cycle. Interestingly the macro-channel separated flow models yielded better comparison with the results than the recent small channel correlation. More importantly it was found that manipulating a throttling valve upstream of the channels; the pressure oscillation could be controlled.

Proposed techniques for getting uniform flow in the parallel channels

Hrnjak[58] addressed the problem of maldistribution of two-phase flow in parallel micro-channel heat exchangers. One approach was to branch the inlet header, which was virtually impossible, as hundreds of parallel channels are needed in heat exchangers.

In the case of PEFC branching might prove to be effective although this would require more volume and pressure penalty was high. Another approach was to use a conical header as shown schematically in Figure **1-3**. This configuration was very efficient with the pressure drop as well. But this design would require fundamental change in the PEFC design and the packing efficiency of the PEFC stack would decrease substantially. Another approach was to use a strong jet at the inlet (Figure **1-4)** so that mixing took place to ensure misty flow (micro bubbles) instead of annular or plug flow. This would enhance the performance much but energy requirement to drive the flow would increase significantly. In the case of PEFC this might not be as effective because existing flows are mostly laminar and the parasitic power required to drive the flow would decrease the operating efficiency of the PEFC.

Webb and Chung[59] studied the two-phase flow distribution in parallel channels for different kind of header and channel geometries. It is very difficult to obtain a uniform

flow distribution in all the channels and gravity separation in horizontal headers made the maldistribution even more pronounced. This investigation showed that employing obstacle at the inlet as displayed in Figure **1-5**, could alleviate maldistribution.

Another approach was to use branch headers for directing the flow to different sets of channels. Two such branched header designs patented by Toshihara[60] and Haussman[61] are displayed in Figure **1-6** and Figure **1-7**. Based on these works, the use of a small diameter distribution tube with small spaced exit holes along its length seems to be a viable concept to obtain good flow distribution.

Review of Phase-Change in PEFC

In two-phase modeling of PEFC local thermodynamic equilibrium is often assumed between the liquid and gas phases at the evaporation/condensation interface. This assumption indicates that very small super-saturation of water vapor exists in the gas phase when condensation or evaporation occurs. This chemical equilibrium is at the micro-scale and in the vicinity of an interface. The existence of interfacial equilibrium at a phase-change interface does not mean zero phase-change rate. Indeed, finite phase-change rate can co-exist with the interfacial equilibrium condition. Analogously, an extremely facile electrochemical reaction yields negligibly small overpotential or an equilibrium condition, but there is still reaction current occurring at the electrochemical interface.

In general, in the literature [62, 63,26] the phase change rate can be expressed as:

$$r_{H_2O} = H(C_{H_2O} - C_{sat}) \qquad (\mathbf{1.3})$$

where H is directly proportional to the area of the interfacial surface where phase change occurs. In porous layers of fuel cells, the liquid-vapor interfacial area is usually sufficiently large that

$$C_{H_2O} - C_{sat} = \frac{r_{H_2O}}{H} \to 0$$

yielding equilibrium phase change. On the other hand, if H is not sufficiently large, there exists non-equilibrium phase change. Wang et al.[62] show that the coefficient H is proportional to aD_{H2O}/r_p, where r_p is the pore radius, a the liquid-vapor interfacial area (proportional to $1/r_p$) and D_w the water-vapor diffusivity in gas. For a GDL with pore radius of 10 μm and water vapor diffusivity of the order of 10^{-5} m^2/s, H-value is on the order of $10^5 s^{-1}$. Recent calculations by Meng[63] clearly indicates that the interfacial equilibrium is reached when H approaches $5 \times 10^3 s^{-1}$. Therefore, the interfacial thermodynamic equilibrium should be quite valid in PEFCs, particularly in the GDL regions. Mathematicians call this the "big-H regularization"[64]. Following the same order of magnitude analysis the time scale to reach local interfacial equilibrium is found to be only 10 μs (using a characteristic length scale of 10 μm and diffusivity of 10^{-5} m^2/s), sufficiently short to justify the assumption even in transient models that deal with physical events longer than 10 ms[65].

Presence of liquid water in a PEFC affects the heat transfer in a very interesting manner. The heat pipe effect increases the effective thermal conductivity of the material [66]. At constant current density total hear transferred through the GDL is also constant. If the conductivity of the GDL decreases then the thermal resistance increases, thereby increasing the temperature in the Cathode Catalyst Layer. The effective thermal

conductivity due to phase change (or the heat pipe effect) remains constant. Therefore, at lower GDL conductivity fraction of heat transferred due to heat pipe effect increases. Due to the favorable heat pipe effect temperature gradient increases at a lower rate than reduction in thermal conductivity of GDL while transferring the same amount of heat.

Figures

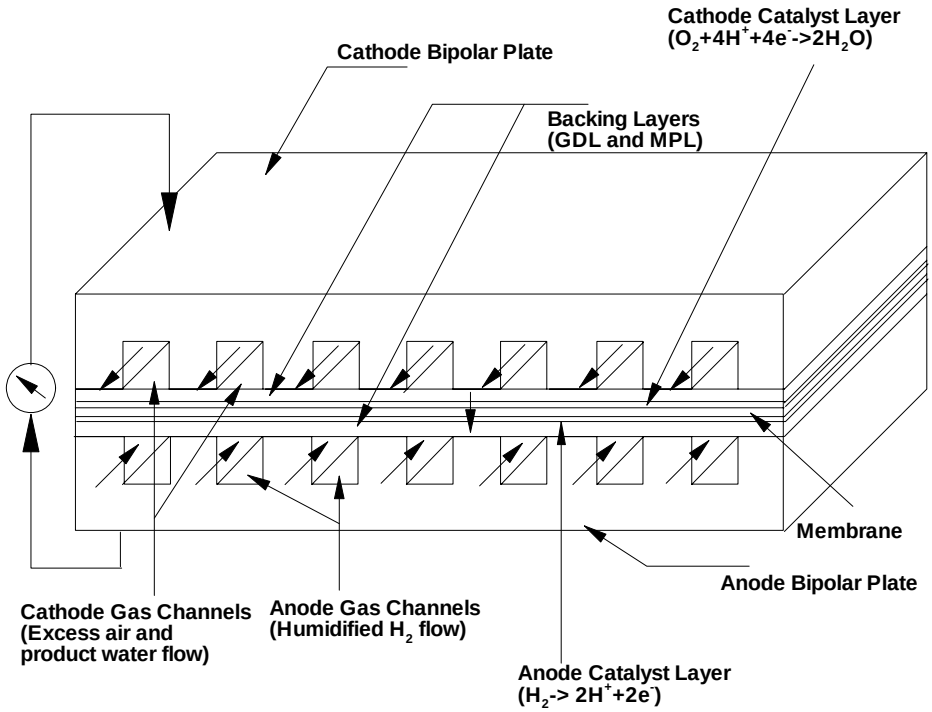

Figure **1-1**: Schematic of a typical parallel channel counter-flow PEFC.

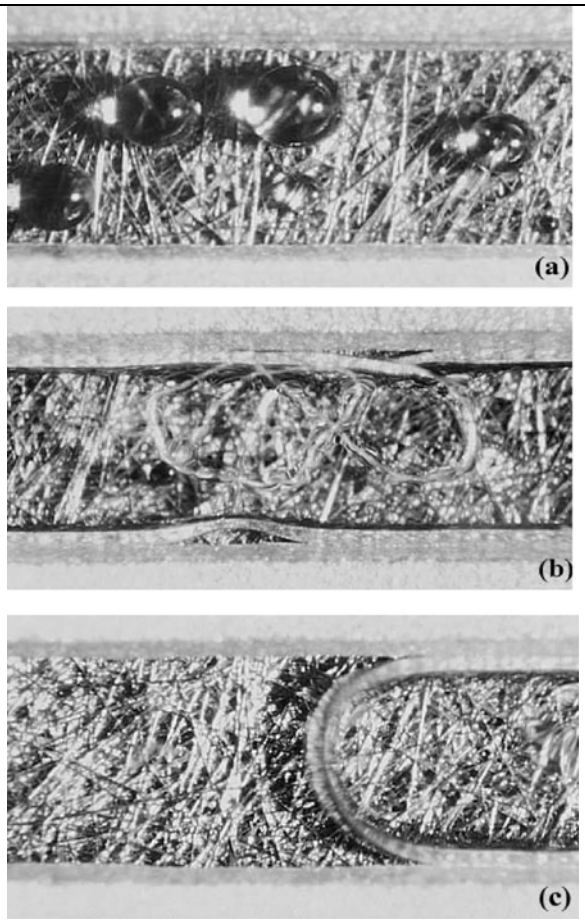

Figure **1-2**: Close-up photograph of liquid water distribution in a PEFC Channel [23].

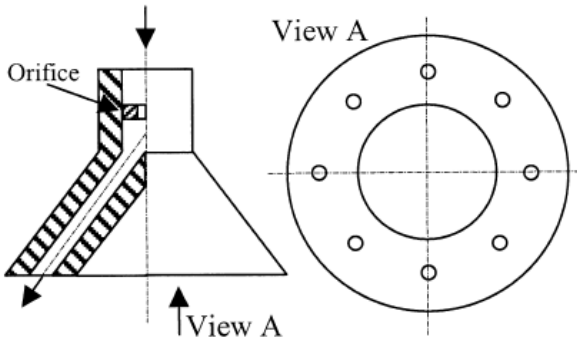

Figure **1-3**: Conical Branch Inlet Header [58].

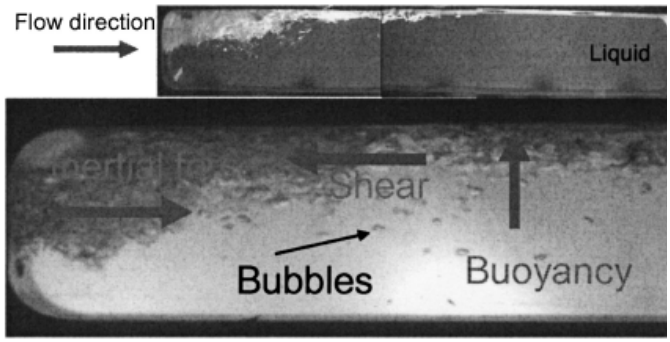

Figure **1-4**: Jet of gas to make sure the flow regime remain misty [58].

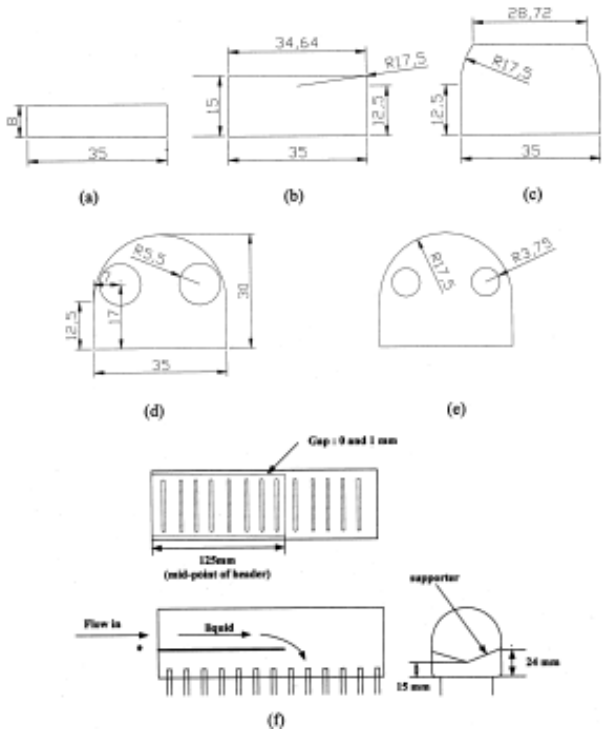

Figure **1-5**: Obstacles at inlet to header to smooth out the maldistribution [59].

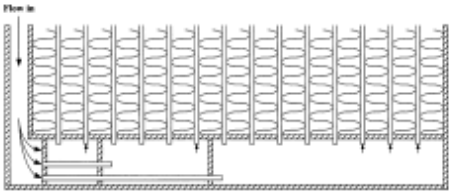

Figure **1-6**: Heat Exchanger Header by Toshihara [60].

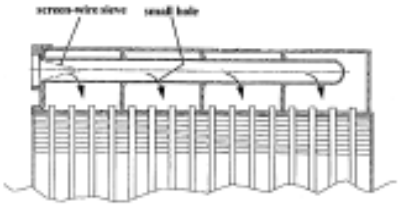

Figure **1-7**: Inlet Distributor Tube with Sieve Mesh Distribution [61].

Chapter 2

Analytical Model of Flow Maldistribution in the Cathode Gas Channels

Introduction

Gas-liquid two-phase flow through the gas channels of a polymer electrolyte fuel cell (PEFC) is of great concern as reactant oxygen is supplied and product water is removed solely through the cathode channels. GDL (gas diffusion layer) intrusion in the gas channels, which is inherent to the PEFC fabrication process (shown in Figure **2-1)**, increases the flow resistance in some of the channels and consequently results in lower rates of flows through these. A one-dimensional analytical model is developed in this chapter to elucidate the fundamentals of flow maldistribution in the cathode gas channels that result from GDL intrusion. Relative humidity (RH) at the inlet and the stoichiometric flow ratio or simply stoichiometry are identified as the two key parameters that have strong influence on the flow maldistribution in PEFC channels. Interestingly, our analysis shows that decreasing the inlet RH can worsen flow maldistribution. Since GDL intrusion in the channel is inevitable, a good flow-field design should be one that is inherently resistant to flow maldistribution. Employing the analytical model developed in the present work, the number of flow channels and turns are optimized in order to minimize the detrimental effect of GDL intrusion.

Analytical Model

In the present work, we consider a cathode gas channel of a PEFC with 'y' being the flow direction as shown in Figure **2-2**. A constant source term is assumed for both mass and water species. Mass conservation is applied in the control volume covering the entire channel cross-section from y=0 to y=L. To enable an analytical treatment, the following assumptions are made:

1) Flow in the channel is taken to occur predominantly in the y direction. That is, $\vec{u} = (0, u, 0)$.

2) The momentum transfer across the GDL-Channel interface is negligible as compared with the momentum due to gas flow in the channel.

3) The net water transport coefficient is assumed to be zero.

Mass conservation of the mixture in the channel along the flow direction yields:

$$\frac{\partial(\rho u)}{\partial y} = \frac{M^{H_2} I}{2FL_x} \qquad (\mathbf{2.1})$$

The source term is due to the mass of H_2 added to the cathode channel due to the production of H_2O [46]. Integrating Eq. **2.1** in the flow direction we get,

$$A_{xz}\rho u = A_{xz}(\rho u)_{in} + \frac{L_z M^{H_2}}{2F}\int_0^y I dy \qquad (\mathbf{2.2})$$

Since

$$(\rho u)_{in} = \rho_g \xi_c \frac{I_{avg} A_{mem}}{4FC_{in}^{O_2} A_{xz}} \qquad (\mathbf{2.3})$$

combining Eq. **2.2** and Eq. **2.3** we get,

$$\rho u = \frac{I_{avg} A_{mem} M^{H_2}}{4FA_{xz}} \left[\frac{\rho_g}{C_{in}^{O_2} M^{H_2}} \xi_c + 2 \int_0^y \frac{I}{I_{avg}} \frac{dy}{L} \right] \quad \textbf{(2.4)}$$

For convenience, we define the following non-dimensional variables and numbers:

$$Y = \frac{y}{L} \quad \textbf{(2.5a)}$$

$$\bar{I} = \frac{I}{I_{avg}} \quad \textbf{(2.5b)}$$

$$\psi = \frac{\rho_g}{C_{in}^{O_2} M^{H_2}} \quad \textbf{(2.5c)}$$

$$\zeta = \frac{I_{avg} A_{mem} M^{H_2}}{4FA_{xz}} \quad \textbf{(2.5d)}$$

The number $\frac{2}{\psi}$ represents fractional increase in density if all the oxygen produces water and all of the product water is carried into the cathode channel. The number 2ζ represents the mass flux of hydrogen into the cathode channel due to water production.

Using the non-dimensional variables and numbers as defined in Eq. **2.5** we can reduce Eq. **2.4** to a compact form as follows:

$$\rho u = \zeta \left[\psi \xi_c + 2 \int_0^Y \bar{I} dY \right] \quad \textbf{(2.6)}$$

which can be simplified further by introducing the following two additional assumptions:

4) As we are not concerned with resolving the details of the electrochemical reactions in the present work, current production is taken to be independent of axial location y; that is,

$I = Const.$

5) When the stoichiometry of oxygen is greater than or equal to unity, we take the current density to be I_{avg} A/m^2. But when the stoichiometry is less than unity we assume 100% oxygen utilization. Therefore, the current density becomes $\xi_c I_{avg}$ A/m^2. So we have:

$\bar{I}(\xi_c, Y) = 1.0$ for $\xi_c \geq 1.0$

$\bar{I}(\xi_c, Y) = \xi_c$ for $\xi_c < 1.0$

Applying these assumptions to Eq. **2.6**, we get:

$$\rho u(\xi_c, Y) = \zeta[\psi\xi_c + 2Y] \text{ for } \xi_c \geq 1.0 \quad \textbf{(2.7 a)}$$

$$\rho u(\xi_c, Y) = \zeta\xi_c[\psi + 2Y] \text{ for } \xi_c < 1.0 \quad \textbf{(2.7b)}$$

The phase mobility of liquid and gas phases are defined with respect to their relative permeability and kinematic viscosity as the following[41]:

$$\lambda_l = \frac{k_{rl}/\nu_l}{k_{rl}/\nu_l + k_{rg}/\nu_g} \text{ and } \lambda_g = 1 - \lambda_l \quad \textbf{(2.8)}$$

where, $k_{rl} = s^5$ and $k_{rg} = (1-s)^{5\ 67}$. Using the continuity equation and the species conservation equation, we obtain[46]:

$$\lambda_l = \frac{\frac{\xi_c}{2}\left(\frac{C^{H_2O}}{C^{O_2}}\right)_{in} + \frac{\int_0^y Idy}{I_{avg}L} - \frac{C_{sat}^{H_2O}}{\rho_g}\left(\frac{\xi_c}{2}\left(\frac{\rho}{C^{O_2}}\right)_{in} + \frac{\int_0^y Idy}{I_{avg}L}M^{H_2}\right)}{\left(\frac{1}{M^{H_2O}} - \frac{C_{sat}^{H_2O}}{\rho_g}\right)\left(\frac{\xi_c}{2}\left(\frac{\rho}{C^{O_2}}\right)_{in} + \frac{\int_0^y Idy}{I_{avg}L}M^{H_2}\right)} \quad \textbf{(2.9)}$$

and $\lambda_l \geq 0$

Using Assumptions 4 and 5 on this, we can simplify Eq. **2.9** as

$$\lambda_l = \frac{\frac{\xi_c}{2}\left(\frac{C^{H_2O}}{C^{O_2}}\right)_{in} + Y - \frac{C_{sat}^{H_2O}}{\rho_g}\left(\frac{\xi_c}{2}\left(\frac{\rho}{C^{O_2}}\right)_{in} + YM^{H_2}\right)}{\left(\frac{1}{M^{H_2O}} - \frac{C_{sat}^{H_2O}}{\rho_g}\right)\left(\frac{\xi_c}{2}\left(\frac{\rho}{C^{O_2}}\right)_{in} + YM^{H_2}\right)} \quad \text{for } \xi_c \geq 1.0$$

$$\lambda_l = \frac{\frac{\xi_c}{2}\left(\frac{C^{H_2O}}{C^{O_2}}\right)_{in} + \xi_c Y - \frac{C_{sat}^{H_2O}}{\rho_g}\left(\frac{\xi_c}{2}\left(\frac{\rho}{C^{O_2}}\right)_{in} + \xi_c YM^{H_2}\right)}{\left(\frac{1}{M^{H_2O}} - \frac{C_{sat}^{H_2O}}{\rho_g}\right)\left(\frac{\xi_c}{2}\left(\frac{\rho}{C^{O_2}}\right)_{in} + \xi_c YM^{H_2}\right)} \quad \text{for } \xi_c < 1.0 \qquad \textbf{(2.10)}$$

$$\text{and } \lambda_l \geq 0$$

By defining the following two non-dimensional parameters,

$$\alpha = \frac{\frac{1}{M^{H_2}} - \frac{C_{sat}^{H_2O}}{\rho_g}}{\frac{1}{M^{H_2O}} - \frac{C_{sat}^{H_2O}}{\rho_g}} \qquad \textbf{(2.11a)}$$

$$\beta = \frac{\frac{C_{sat}^{H_2O} - C_{in}^{H_2O}}{2M^{H_2}C_{in}^{O_2}}}{\frac{1}{M^{H_2O}} - \frac{C_{sat}^{H_2O}}{\rho_g}} \qquad \textbf{(2.11b)}$$

we can simplify Eq. **2.10** as,

$$\lambda_l = \alpha - \frac{\beta + \frac{\alpha\psi}{2}}{\frac{Y}{\xi_c} + \frac{\psi}{2}} \quad \text{for } \xi_c \geq 1.0$$

$$\lambda_l = \alpha - \frac{\beta + \frac{\alpha\psi}{2}}{Y + \frac{\psi}{2}} \quad \text{for } \xi_c < 1.0 \qquad \textbf{(2.12)}$$

and $\lambda_l \geq 0$

In Eq. **2.11** β represents the capacity of the inlet flow to take up water in vapor form. Accordingly, for saturated flow at the inlet β is zero.

For an unsaturated flow at the inlet ($\beta > 0$), the inlet is always dry. The liquid starts to appear when in Eq. **2.12**:

$$\lambda_l = 0 \tag{**2.13**}$$

This gives,

$$Y_{dry} = Y\Big|_{\lambda_l=0} = \frac{\beta}{\alpha}\xi_c \quad \text{for } \xi_c \geq 1.0 \tag{**2.14a**}$$

$$Y_{dry} = Y\Big|_{\lambda_l=0} = \frac{\beta}{\alpha} \quad \text{for } \xi_c < 1.0 \tag{**2.14b**}$$

This is subject to the constraint $Y_{dry} \leq 1.0$. From these equations we can see that for saturated flow at the inlet, two-phase flow starts also at the inlet. Moreover, as the stoichiometry increases, the dry length of the channel would increase linearly with it.

Using the definition of liquid mobility λ_l from Eq. **2.8** we have:

$$s = \frac{1}{\left(\frac{1-\lambda_l}{\lambda_l}\left(\frac{\nu_g}{\nu_l}\right)\right)^{\frac{1}{5}} + 1} \text{ for } \lambda_l > 0$$

$$s = 0 \text{ for } \lambda_l = 0 \tag{**2.15**}$$

For steady-state, one-dimensional two-phase flow in the channels, the momentum equation (following Darcy Law) reduces to,

$$\frac{\partial P}{\partial y} = -\frac{\nu}{K}(\rho u) \tag{**2.16**}$$

Therefore, we can compute the total pressure drop as,

$$\Delta P = -\int_0^L \left(\frac{\partial P}{\partial y}\right) dy \tag{2.17}$$

In Eq. **2.16**, the permeability K is taken to be known and the flux can be computed as a function of Y from Eq. **2.7**. The value of the mixture viscosity can be obtained using the following mixture rule:

$$\nu = \left(\frac{k_{rl}}{\nu_l} + \frac{k_{rg}}{\nu_g}\right)^{-1} \tag{2.18}$$

Using Eq. **2.15** in the constitutive relation for the relative permeabilities, we get:

$$k_{rl} = s^5 = \frac{\lambda_l \nu_l}{\left[((1-\lambda_l)\nu_g)^{1/5} + (\lambda_l \nu_l)^{1/5}\right]^5} \tag{2.19}$$

and,

$$k_{rg} = (1-s)^5 = \frac{(1-\lambda_l)\nu_g}{\left[((1-\lambda_l)\nu_g)^{1/5} + (\lambda_l \nu_l)^{1/5}\right]^5} \tag{2.20}$$

Therefore, we get from Eq. **2.18**:

$$\nu = \left[((1-\lambda_l)\nu_g)^{1/5} + (\lambda_l \nu_l)^{1/5}\right]^5 \tag{2.21}$$

Using Eq. **2.19** and Eq. **2.20** in the pressure drop relation, Eq. **2.17** , we have:

$$\Delta P = \int_0^L \frac{\nu}{K}(\rho u) dy = \frac{1}{K}\int_0^L \left[((1-\lambda_l)\nu_g)^{1/5} + (\lambda_l \nu_l)^{1/5}\right]^5 (\rho u) dy \tag{2.22}$$

By defining the following non-dimensional mixture kinematic viscosity:

$$\overline{\nu} = \frac{\nu}{\nu_g} = \left[(1-\lambda_l)^{1/5} + (\lambda_l \nu_l / \nu_g)^{1/5}\right]^5 \tag{2.23}$$

We can simplify Eq. **2.22** to arrive at:

$$\Delta P = \frac{\nu_g L}{K}\zeta\int_0^L \bar{\nu}\left[\psi\xi_c + 2Y\right]dY \quad \text{for } \xi_c \geq 1.0 \tag{2.24a}$$

$$\Delta P = \frac{\nu_g L}{K}\zeta\int_0^L \bar{\nu}\xi_c\left[\psi + 2Y\right]dY \quad \text{for } \xi_c < 1.0 \tag{2.24b}$$

In the integral in Eq. **2.22**, the term (ρu) is a linear function of y, while the mixture viscosity is not an integrable function. However, for a single-phase flow Eq. **2.22** is integrable as $\bar{\nu} = 1.0$ (here, $\bar{\nu}$ is the non-dimensional mixture kinematic viscosity as defined in Eq. **2.23**).

For all parallel gas channels, the pressure drop should remain equal. Due to GDL intrusion into the channels, the cross-section area of the channel decreases. This would mean less flow in that channel; and therefore, the local stoichiometry would decrease. To keep the average stoichiometry the same, velocity would increase in the un-intruded channels. Therefore, the pressure drop would increases. The GDL intrusion is considered only at the end channels of the parallel channels. If the number of parallel channels (i.e. 'n') is large, then we can neglect the increment of the flow velocity in the unintruded channels. If δ is the fractional reduction in cross-section area of the channel and ε is the fractional reduction in local stoichiometry as a result of that, then we have the following:

For intruded channel,

$$\begin{aligned} A_{xz} &= \overline{A}_{xz}(1-\delta) \\ \xi_c &= \bar{\xi}_c(1-\varepsilon) \end{aligned} \tag{2.25}$$

The permeability of the intruded channel also decreases due to GDL intrusion. Using the Hagen-Poiseuille equation we get[38],

$$K = c\frac{d_h^2}{32} \tag{2.26}$$

Since $d_h = 4\dfrac{L_x \dfrac{L_z}{2}}{2\left(L_x + \dfrac{L_z}{2}\right)}$, Eq. **2.26** becomes upon substitution:

$$K = \frac{c}{8}\left(\frac{L_x \dfrac{L_z}{2}}{\left(L_x + \dfrac{L_z}{2}\right)}\right)^2 \tag{2.27}$$

Due to GDL intrusion, length in x-direction decreases. Therefore, for the intruded channel we get:

$$K = \frac{c}{8}\left(\frac{L_z}{2}\right)^2 \frac{(1-\delta)^2}{\left((1-\delta) + \dfrac{L_z/2}{L_x}\right)^2} \tag{2.28}$$

In the present work, we assume $\dfrac{L_z/2}{L_x} = 2.0$. Therefore, we can approximate the expression for channel permeability as,

$$K = \frac{c}{8}\left(\frac{L_x \dfrac{L_z}{2}}{\left(L_x + \dfrac{L_z}{2}\right)}\right)^2 (1-\delta)^2 = \overline{K}(1-\delta)^2 \tag{2.29}$$

where, $\overline{K}$ is the channel permeability without GDL intrusion. We have computed the exact value of channel permeability as a function of δ using a CFD code. The numerically computed K is compared to the approximate estimate expressed by Eq. **2.29** as shown in Figure **2-3** it is clear that our simple approximate formula can closely approximate the exact relation between channel permeability and GDL intrusion.

For unintruded channel,

$$A_{xz} = \overline{A}_{xz}$$

$$K = \overline{K} \qquad \textbf{(2.30)}$$

$$\xi_c = \overline{\xi}_c\left(1+\frac{2}{n-2}\varepsilon\right)$$

where, n is the number of parallel channels. So, for a parallel network of channels we have,

$$\Delta P = \Delta P\left(\overline{\xi}_c, \delta, \varepsilon\right)_{\text{int } ruded} = \Delta P\left(\overline{\xi}_c, \delta, \varepsilon\right)_{un\,\text{int } ruded} \qquad \textbf{(2.31)}$$

Using Eq. **2.25** and Eq. **2.27** on Eq. **2.24** we have:

$$\frac{\Delta P_{\text{int } ruded}}{\frac{\nu_g L}{K}\cdot\zeta} = \frac{1}{(1-\delta)^3}\int_0^1 \overline{\nu}\left(\overline{\xi}_c(1-\varepsilon), Y\right)\left[\psi\overline{\xi}_c(1-\varepsilon)+2Y\right]dY \text{ for } \overline{\xi}_c(1-\varepsilon)\geq 1.0 \qquad \textbf{(2.32a)}$$

$$\frac{\Delta P_{\text{int } ruded}}{\frac{\nu_g L}{K}\cdot\zeta} = \frac{1}{(1-\delta)^3}\int_0^1 \overline{\nu}\left(\overline{\xi}_c(1-\varepsilon), Y\right)\overline{\xi}_c\left[\psi(1-\varepsilon)+2Y\right]dY \text{ for } \overline{\xi}_c(1-\varepsilon)< 1.0 \qquad \textbf{(2.32b)}$$

Using Eq.**2.28** on Eq. **2.24**, we get,

$$\frac{\Delta P_{un\,\text{int } ruded}}{\frac{\nu_g L}{K}\cdot\zeta} = \int_0^1 \overline{\nu}\left(\xi_c\left(1+\frac{2}{n-2}\varepsilon\right), Y\right)\left[\psi\xi_c\left(1+\frac{2}{n-2}\varepsilon\right)+2Y\right]dY \qquad \textbf{(2.33)}$$

Now we can combine Eq. **2.32** and Eq. **2.33** to find a relation between area maldistribution (δ) and flow maldistribution (ε).

$$\delta = 1-\left[\frac{\int_0^1 \overline{\nu}\left(\overline{\xi}_c(1-\varepsilon), Y\right)\left[\psi\overline{\xi}_c(1-\varepsilon)+2Y\right]dY}{\int_0^1 \overline{\nu}\left(\overline{\xi}_c\left(1+\frac{2}{n-2}\varepsilon\right), Y\right)\left[\psi\xi_c\left(1+\frac{2}{n-2}\varepsilon\right)+2Y\right]dY}\right]^{\frac{1}{3}} \text{ for } \overline{\xi}_c(1-\varepsilon)\geq 1.0 \qquad \textbf{(2.34a)}$$

$$\delta = 1 - \left[\frac{\int_0^1 \bar{\nu}\left(\bar{\xi}_c(1-\varepsilon), Y\right)\bar{\xi}_c(1-\varepsilon)\left[\psi + 2Y\right]dY}{\int_0^1 \bar{\nu}\left(\bar{\xi}_c\left(1+\frac{2}{n-2}\varepsilon\right), Y\right)\left[\psi\xi_c\left(1+\frac{2}{n-2}\varepsilon\right) + 2Y\right]dY} \right]^{\frac{1}{3}} \quad \text{for } \bar{\xi}_c(1-\varepsilon) < 1.0 \qquad \textbf{(2.34b)}$$

In the case of single-phase flow we have $\bar{\nu} = 1.0$ and thus Eq. **2.34** can be integrated. Therefore, for single phase flow we have,

$$\delta = 1 - \left[\frac{\psi\bar{\xi}_c(1-\varepsilon) + 1}{\psi\bar{\xi}_c\left(1+\frac{2}{n-2}\varepsilon\right) + 1} \right]^{\frac{1}{3}} \quad \text{for} \quad \bar{\xi}_c(1-\varepsilon) \geq 1.0 \qquad \textbf{(2.35a)}$$

$$\delta = 1 - \left[\bar{\xi}_c(1-\varepsilon)\frac{\psi + 1}{\psi\bar{\xi}_c\left(1+\frac{2}{n-2}\varepsilon\right) + 1} \right]^{\frac{1}{3}} \quad \text{for} \quad \bar{\xi}_c(1-\varepsilon) < 1.0 \qquad \textbf{(2.35b)}$$

With these sets of equations, it is possible to develop a map of area maldistribution vs. flow maldistribution, which can provide a range of parameters for safe operation and the minimum or stoichiometric amount of oxygen reactant that needs to be supplied to all channels.

Since, the value of ψ is of the order of 70 we can neglect 2Y with respect to it. Implementing this approximation in Eq. **2.34** we can get,

$$\frac{\int_0^1 \bar{\nu}\left(\bar{\xi}_c(1-\varepsilon), Y\right)dY}{\int_0^1 \bar{\nu}\left(\bar{\xi}_c\left(1+\frac{2}{n-2}\varepsilon\right), Y\right)dY} = (1-\delta)^3 \frac{1+\frac{2\varepsilon}{n-2}}{1-\varepsilon} \qquad \textbf{(2.36)}$$

Let us define average kinematic viscosity for a channel as the following:

$$\widetilde{\nu} = \int_0^1 \overline{\nu} dY = Y_{dry} + \int_{Y_{dry}}^1 \overline{\nu} dY \tag{2.37}$$

The first term of the right hand side of Eq. **2.37** is due to the dry part of the channel (single-phase flow) and the second term is due to the wet part of the channel (two-phase flow). Mixture kinematic viscosity is greater than the kinematic viscosity of air $(\overline{\nu} > 1.0)$. Therefore, $\widetilde{\nu}$ is a decreasing function of Y_{dry}.

Using Eq. **2.37** on the left hand side of Eq. **2.36** of we can get,

$$\frac{\widetilde{\nu}_{\text{int}\,ruded}}{\widetilde{\nu}_{un\,\text{int}\,ruded}} = \frac{\int_0^1 \overline{\nu}\left(\overline{\xi}_c(1-\varepsilon), Y\right) dY}{\int_0^1 \overline{\nu}\left(\overline{\xi}_c\left(1+\frac{2}{n-2}\varepsilon\right), Y\right) dY} = \frac{Y_{dry}^{\text{int}\,ruded} + \int_{Y_{dry}^{\text{int}\,ruded}}^1 \overline{\nu}\left(\overline{\xi}_c(1-\varepsilon), Y\right) dY}{Y_{dry}^{un\,\text{int}\,ruded} + \int_{Y_{dry}^{un\,\text{int}\,ruded}}^1 \overline{\nu}\left(\overline{\xi}_c\left(1+\frac{2}{n-2}\varepsilon\right), Y\right) dY} \tag{2.38}$$

Total number of parallel channels (n) are usually large for most of the designs. So, the dependence of $\widetilde{\nu}_{un\,\text{int}\,ruded}$ on flow maldistribution ε is weak. Hence, the denominator of Eq. **2.38** could be taken as constant for a given operating condition. Using that we can rearrange Eq. **2.38** as:

$$\frac{\widetilde{\nu}_{\text{int}\,ruded}}{\widetilde{\nu}_{un\,\text{int}\,ruded}} = \frac{\left(Y_{dry}^{un\,\text{int}\,ruded} - \Delta Y_{dry}\right) + \int_{Y_{dry}^{un\,\text{int}\,ruded} - \Delta Y_{dry}}^1 \overline{\nu}\left(\overline{\xi}_c(1-\varepsilon), Y\right) dY}{Y_{dry}^{un\,\text{int}\,ruded} + \int_{Y_{dry}^{un\,\text{int}\,ruded}}^1 \overline{\nu}\left(\overline{\xi}_c\left(1+\frac{2}{n-2}\varepsilon\right), Y\right) dY} \tag{2.39}$$

where, $\Delta Y_{dry} (= Y_{dry}^{un\,\text{int}\,ruded} - Y_{dry}^{\text{int}\,ruded})$.

The difference in dry length between intruded and unintruded channels is important because flow resistance in two-phase flow is several times the flow resistance

in single-phase flow. Therefore, as the ΔY_{dry} increases the flow resistance in the intruded channel (with respect to the unintruded channel) also increases. For a parallel channel configuration, the total pressure drop is the same for both the intruded and the un-intruded channel. Therefore, if the flow resistance is large in the intruded channel, even a small GDL intrusion will result in appreciable flow maldistribution. This would decrease a PEFC's ability to tolerate GDL intrusion. The dry length of a channel can be determined using Eq. **2.14**.The difference of dry length ΔY_{dry} between the intruded and unintruded channel is,

$$\Delta Y_{dry} = Y_{dry}^{un\,\mathrm{int}\,ruded} - Y_{dry}^{\mathrm{int}\,ruded} = \frac{\beta}{\alpha}\bar{\xi}_c \varepsilon \frac{n}{n-2}$$

$$\frac{\beta}{\alpha}\bar{\xi}_c\left(1+\frac{2}{n-2}\varepsilon\right) \le 1.0$$

$$\Delta Y_{dry} = 1 - \frac{\beta}{\alpha}\bar{\xi}_c(1-\varepsilon) \qquad \text{for} \quad \frac{\beta}{\alpha}\bar{\xi}_c\left(1+\frac{2}{n-2}\varepsilon\right) > 1.0 > \frac{\beta}{\alpha}\bar{\xi}_c(1-\varepsilon) \tag{2.40}$$

$$\Delta Y_{dry} = 0 \qquad \text{for} \quad \frac{\beta}{\alpha}\bar{\xi}_c(1-\varepsilon) \ge 1.0$$

As ΔY_{dry} increases, the first term in the left hand side numerator of Eq. **2.39** decreases, while the second term increases. Since $\bar{\nu} > 1.0$ for the operational range, $\frac{\widetilde{\nu}_{\mathrm{int}\,ruded}}{\widetilde{\nu}_{un\,\mathrm{int}\,ruded}}$ is an increasing function of ΔY_{dry}. From the design perspective for smooth operation of a PEFC, a certain allowable flow maldistribution can be fixed. Combining Eq. **2.36** and Eq. **2.39** we get,

$$\frac{\widetilde{\nu}_{\text{int}\,ruded}}{\widetilde{\nu}_{un\,\text{int}\,ruded}} = \frac{\left(Y_{dry}^{un\,\text{int}\,ruded} - \Delta Y_{dry}\right) + \int_{Y_{dry}^{un\,\text{int}\,ruded} - \Delta Y_{dry}}^{1} \bar{\nu}\left(\bar{\xi}_c(1-\varepsilon), Y\right) dY}{Y_{dry}^{un\,\text{int}\,ruded} + \int_{Y_{dry}^{un\,\text{int}\,ruded}}^{1} \bar{\nu}\left(\bar{\xi}_c\left(1+\frac{2}{n-2}\varepsilon\right), Y\right) dY} = (1-\delta)^3 \frac{1+\frac{2\varepsilon}{n-2}}{1-\varepsilon} \qquad \textbf{(2.41)}$$

Therefore, Eq. **2.41**, we can see that given the allowable flow maldistribution (ε), the greater $\frac{\widetilde{\nu}_{\text{int}\,ruded}}{\widetilde{\nu}_{un\,\text{int}\,ruded}}$, the smaller allowable GDL intrusion (δ) is. This indicates that with increasing ΔY_{dry}, allowable GDL intrusion δ decreases. Therefore we can consider that ΔY_{dry} is the parameter that controls maldistribution. For an optimal design, ΔY_{dry} has to be minimized.

Results and Discussion

We choose a PEFC configuration with seven parallel channels with the end channels being prone to GDL intrusion. Since low stoichiometry operation minimizes the parasitic power loss, a stoichiometry of 2.0 is used here. Using Eq. **2.34** and Eq. **2.35**, we can estimate the extent of GDL intrusion for a given maldistribution in terms of stoichiometry.

It is clear from Figure **2-4**, that the extent of flow maldistribution in single-phase flow is always much severe than the extent of areal maldistribution. This effect is even more pronounced for two-phase flow as shown in Figure **2-4**. Also plotted in Figure **2-4** is the $\varepsilon = \delta$ curve to help the reader visualize how much the flow maldistribution is greater than the area maldistribution. In the present case, $\varepsilon > 0.5$ would make the local

stoichiometry in the intruded channels less than unity. This condition is undesirable for stable PEFC operations. From Figure **2-4**, we can see that this condition may occur for an area maldistribution as low as 0.2.

When flow maldistribution is 0.1, there is a visible difference in the liquid saturation profile as shown in Figure **2-5**. Dry length decreases in the intruded channel due to low flow rate. Moreover, the maximum liquid saturation increases. As flow maldistribution is increased to 0.5, difference in the liquid saturation profile is enormous as displayed in Figure **2-6**. Notably, the flow situation in the perfect channel does not change much. But the dry length decreases in the intruded channel and amount of liquid at exit is much higher. When flow maldistribution is 0.5, the local stoichiometry reaches unity. So at higher flow maldistribution than this, the liquid saturation in the intruded channel no longer depends on the local stoichiometry (Eq. **2.12**) due to low current production. In Figure **2-7**, for flow maldistribution of 0.9, this effect is shown.

Comparing Figure **2-6** and **2-7**, we can see that the saturation distributions in the intruded channels are the same in both cases. This is due to the reason pointed out earlier. But the higher flow maldistribution causes more flow in the perfect channel. Consequently, the dry length in the prefect channel increases but the overall liquid saturation decreases.

Mitigating Flow Maldistribution:

A typical distribution of dry channel length between intruded and unintruded channels is schematically shown in Figure **2-8**. The amount of GDL intrusion depends on the fabrication pressure and the GDL material. For a better material, which results in

lesser intrusion, it is easier to keep the flow maldistribution within the required range. It is also possible to tweak other parameters to keep the flow maldistribution within the required range. We have already seen that two-phase flow exacerbates flow maldistribution. The ability of the flow to transport water in form of vapor increases when the inlet RH is reduced. In the set of governing equations presented in this work, the RH reduction is reflected in the increment in β.

From Eq. **2.40**, it is clear that for a specified geometry and a fixed flow maldistribution, parameters controlling ΔY_{dry} are β (measure of dryness of the inlet flow) and global stoichiometry $\bar{\xi}_c$. Difference in dry length (ΔY_{dry}) increases linearly with β and $\bar{\xi}_c$ till the unintruded channel becomes completely dry. Then, it decreases linearly with β and $\bar{\xi}_c$, till the intruded channel becomes completely dry, resulting in $\Delta Y_{dry} = 0$. After this, both the channel becomes completely dry and ΔY_{dry} remains equal to zero. At this point the allowable GDL intrusion becomes equal to the allowable GDL intrusion for single-phase flow. Note here that, the non-dimensional group $\frac{\beta}{\alpha}\bar{\xi}_c$ is defined as a measure of the inlet condition to keep the flow dry. For convenience, we define:

$$\eta\left(T_{in}, \bar{\xi}_c\right) = \frac{\beta}{\alpha}\bar{\xi}_c \qquad \textbf{(2.42)}$$

Physically, $Y_{dry} \leq 1.0$, but η represents the dry length were the channel infinitely long. Keeping the flow maldistribution at 0.1, the dry lengths in intruded and unintruded channels are computed for varying η and the results are plotted in Figure **2-9**. The difference between the dry lengths of intruded and unintruded channels (ΔY_{dry}) is plotted

against η in Figure **2-10**. This difference is zero for fully humidified flow ($\eta = 0.0$) but it increases with increasing for η the system. This η can be increased by raising the stoichiometry or lowering the relative humidity. This trend continues till the unintruded channel becomes completely dry; in other words, the dry length in the unintruded channel becomes constant and equal to unity. If η is increased further, difference between dry length decreases rapidly till the intruded channel becomes dry also. At this point, ΔY_{dry} becomes zero again and increasing η further has no effect on ΔY_{dry}. Again, from Eq. **2.40**, we can see that it is possible to minimize ΔY_{dry} by increasing RH or decreasing stoichiometry if the unintruded channel remains wet. When the unintruded channel is dry, ΔY_{dry} can be reduced by either decreasing the relative humidity or by increasing the stoichiometry. If both intruded and unintruded channels are dry, ΔY_{dry} is zero and thus the lowest possible maldistribution is achieved.

Effect of Global Stoichiometry:

The global stoichiometry has a profound effect on the flow maldistribution for a given GDL intrusion. By examining Eq. **2.34** and Eq. **2.35**, we can see that the difference in local stoichiometry is greater at larger global stoichiometry. Therefore, the same amount of GDL intrusion results in greater flow maldistribution as the global stoichiometry increases. In Figure **2-11**, flow maldistribution is plotted against area maldistribution for various global stoichiometries. It is generally believed that using higher stoichiometry; it is possible to mitigate flow maldistribution by using higher global stoichiometry. From the analysis presented earlier, we show that for a fixed flow

maldistribution, GDL intrusion decreases as ΔY_{dry} increases. In the present case, for stoichiometry of 2.0, the unintruded channel never gets completely dry. Therefore, we remain confined in the fist part of Figure **2-10**, in which increasing stoichiometry or decreasing RH exacerbates the maldistribution situation.

We can predict the effect of global stoichiometry on smooth PEFC operation of from Figure **2-11**. Let us consider that the minimum allowable stoichiometry in every channel for smooth operation of the cell is unity. At a global stoichiometry of 1.5, local stoichiometry in the intruded channels reach unity for a GDL intrusion of 0.11. This value of GDL intrusion is termed as allowable GDL intrusion. As we increase the global stoichiometry, the allowable GDL intrusion also increases. At the global stoichiometry of 2.0, the allowable GDL intrusion is 0.17. When we increase the global stoichiometry to 3.0, the allowable GDL intrusion is 0.20. This indicates that allowable GDL intrusion does not increase appreciably even if the global saturation is raised by 50%.

Effect of Relative Humidity:

In Figure **2-12**, the flow maldistribution is plotted against GDL intrusion for various values of inlet relative humidity. The average stoichiometry is set at 2.0 for all cases. For a given flow maldistribution, we require as much allowable GDL maldistribution as possible for a good design. From Figure **2-12**, it is clear that when the relative humidity is low, the allowable GDL intrusion decreases more rapidly as compared with that when RH is high – this trend is predicted by our earlier analysis. Whereas the maximum allowable intrusion occurs for single-phase flow, the closest to that situation can be achieved using 100% RH at the inlet. But this will increase the

pressure drop, and thus cause the parasitic pressure loss to rise. A trade-off between these can be found, depending on operating conditions and allowable parasitic loss and tolerable GDL intrusion. If allowable loss of flow in the intruded channels for a stoichiometry of 2.0 is set at 10%, our computed results show that the maximum allowable GDL intrusion is 4.67% for the single-phase flow. For fully humidified flow, the maximum allowable GDL intrusion is 3.9%. When the relative humidity is decreased to 67% (dew point temperature 70^{o}C), the maximum tolerable GDL intrusion decreases to 1.9%. For a relative humidity of 45% (dew point temperature 60^{o}C), this tolerable GDL intrusion decreases to 0.1%. Therefore, in order to minimize flow maldistribution it is a good idea to keep reactant flow close to fully humidified.

In Figure **2-13**, flow maldistribution is plotted against relative humidity in which the GDL intrusion is fixed at 0.2 and the stoichiometry ranges from 2 to 4. At the stoichiometry of 2.0, the unintruded channel is always wet; therefore, decreasing the relative humidity results in increased flow maldistribution. At the stoichiometry of 3.0, when the relative humidity is decreased, the unintruded channel eventually becomes dry at RH = 40%. Decreasing the RH beyond that has a favorable effect on flow maldistribution. At a high stoihciometry of 4.0, even the intruded channel becomes almost dry; therefore, the flow maldistribution at very low RH (~3%) is equal to that of the single-phase flow maldistribution.

Effect of Flow-Field Design on Minimizing GDL Intrusion

GDL intrusion in the channels is inevitable till new materials with suitable properties can be developed. Therefore, a flow-field design that can minimize the effect

of GDL intrusion has to be identified. Since the GDL intrusion occurs at the channels that form the perimeter, for a fixed active area the perimeter of the flow field needs to be minimized. As an illustration, let's consider a serpentine flow field with n_t turns and n_c parallel channels, and the maximum length of the channel before first turn to be L in mm while the active area be A in mm^2 (as described in Figure **2-14**). Moreover, let's assume that both land and channel widths are equal to L_c mm. From these the area could be represented as,

$$2(n_t + 1)n_c L_c L = A \tag{**2.43**}$$

For this configuration, the GDL intrusion occurs at the length given by

$$L_{gdl-\text{int}rusion} = 2(2n_t n_c L_c + L) = 2\left(2n_t n_c L_c + \frac{A}{2(n_t + 1)n_c L_c}\right) \tag{**2.44**}$$

From Eq. **2.44**, we obtain the following optimal number of turns for a constant number of channels:

$$n_t = \left(\frac{A}{4n_c^2 L_c^2}\right)^{1/2} - 1 \tag{**2.45**}$$

Along the same line, for a constant number of turns, the optimal number of channels is given by

$$n_c = \left(\frac{A}{4n_t(n_t + 1)L_c^2}\right)^{1/2} \tag{**2.46**}$$

From Eq. **2.45** and Eq. **2.46**, it is possible to easily compute the optimal flow-field geometry for a PEFC that is the most resistant to the GDL intrusion. For an industrial size PEFC, the optimal shape of the active area is a square as it has the least perimeter to area ratio of all rectangular shapes.

Conclusions

GDL intrusion in the flow channels of a PEFC can pose a serious problem to its smooth operation and thus threaten its stable performance. An analytical model, which is based on the laws of mass and momentum conservation in two-phase flow, was developed to elucidate effects of the GDL intrusion in the end channels on flow maldistribution in the channels. Results computed from our analytical model show that flow maldistribution is always higher in a two-phase flow as compared with that in a single-phase flow. Our model is capable of predicting pressure, velocity and liquid saturation along the channel. Given a flow maldistribution, the difference in liquid saturation distribution can be computed from our model. Predictions computed from our model further indicate that dry length decreases in the intruded channel whereas the over all liquid saturation increases. For smooth PEFC operations, a minimum stoichiometric supply of reactant should be maintained. At higher flow maldistribution, when the reactant flow in the intruded channels is less than stoichiometric, saturation distribution in the intruded channels become independent of flow maldistribution.

By analyzing all the parameters and their respective effects, we find that differential dry-length (ΔY_{dry}) is one of the parameter controlling maldistribution. For a fixed flow maldistribution, lowering ΔY_{dry} can ensure higher tolerable GDL intrusion. Another finding is that, when both intruded and unintruded channels are wet; increasing stoichiometry or decreasing relative humidity worsens flow maldistribution. When the unintruded channel is dry, these actions produce favorable outcome: that is, reducing flow maldistribution. When both intruded and unintruded channels are dry, tolerable GDL intrusion achieves its maximum. Hereafter, it becomes independent of

stoichiometry and relative humidity. Our analysis further suggests that the effect of maldistribution is the least when the fully humidified inlet condition is used. Although channels remain drier in partially humidified conditions, the presence of liquid water varies widely between intruded and unintruded channels. This exacerbates the flow maldistribution and results in a very low allowable GDL intrusion for a given flow maldistribution. Lastly, as GDL intrusion is inevitable to a PEFC, a flow-field design inherently resistant to intrusion should be used. The optimal number of channels and turns for a desirable PEFC design are obtained by exercising our analytical model.

Figures

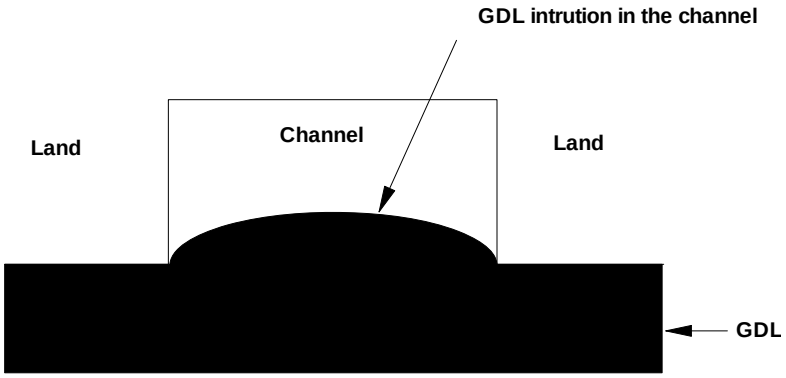

Figure **2-1**: Schematic of a typical GDL intrusion in a channel.

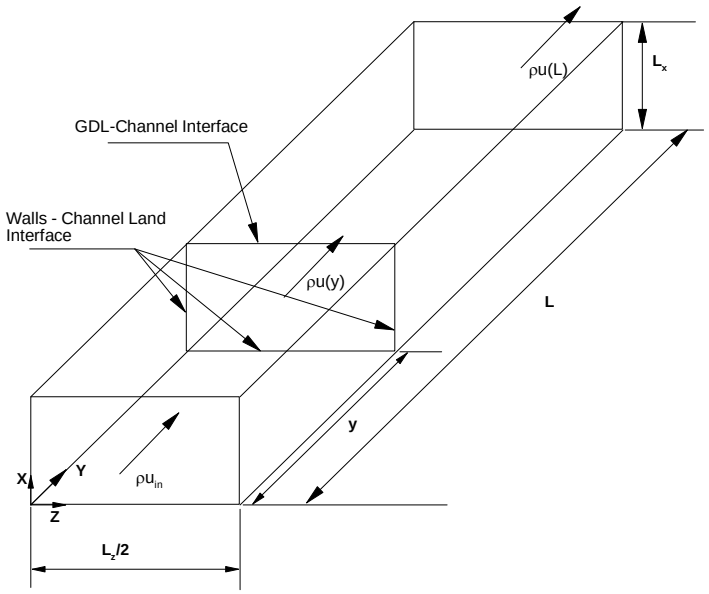

Figure **2-2**: Geometry and Control Volume.

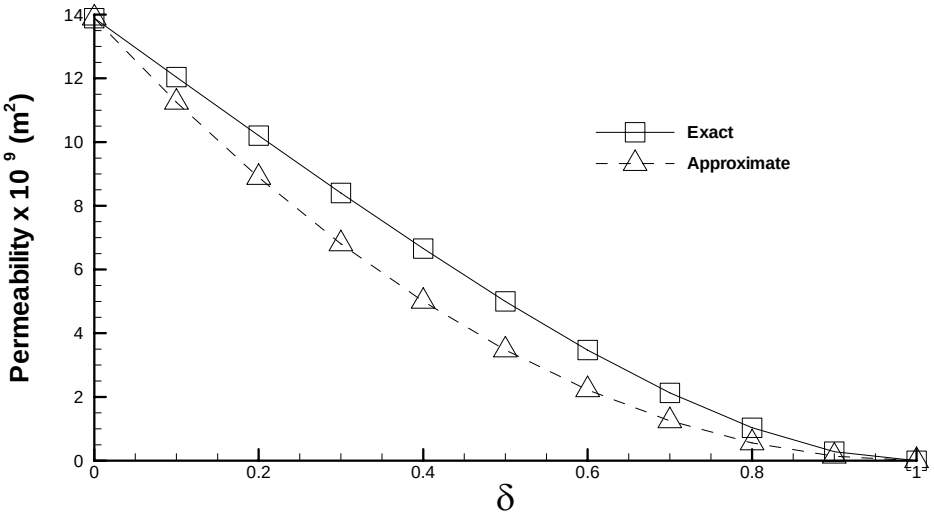

Figure **2-3**: Exact and Approximate permeability as a function of GDL intrusion.

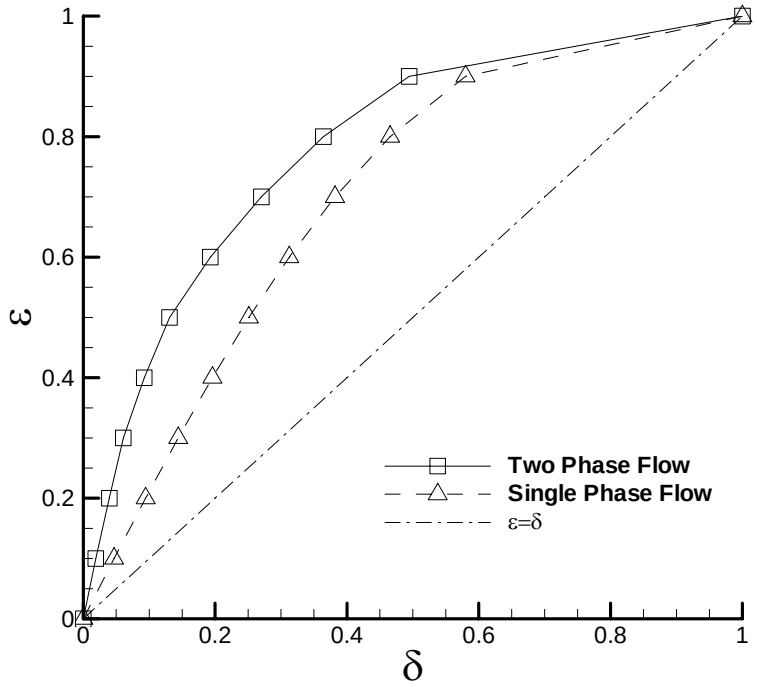

Figure **2-4**: Plot of areal maldistribution vs flow maldistribution ($\overline{\xi}_c = 2.0$, RH=67%).

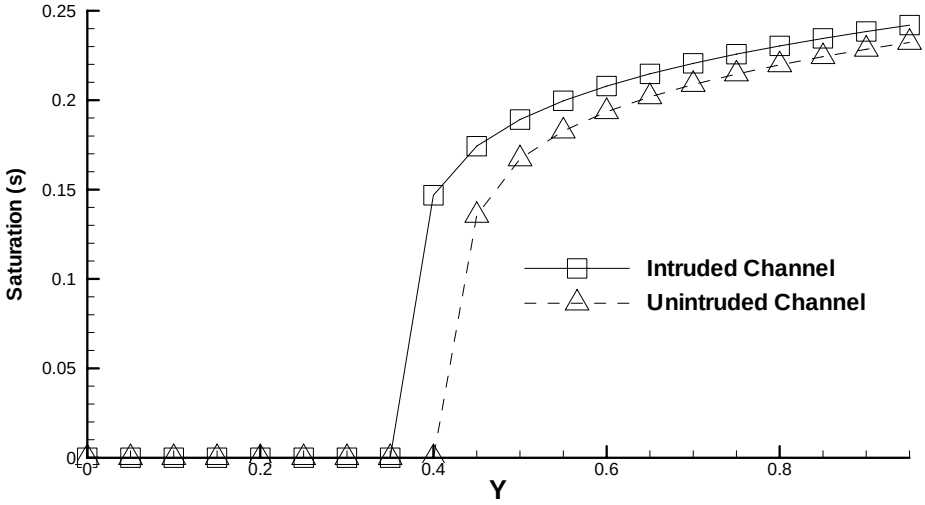

Figure **2-5**: Saturation distributions for $\varepsilon = 0.1$ ($\overline{\xi}_c = 2.0$, RH=67%)**.**

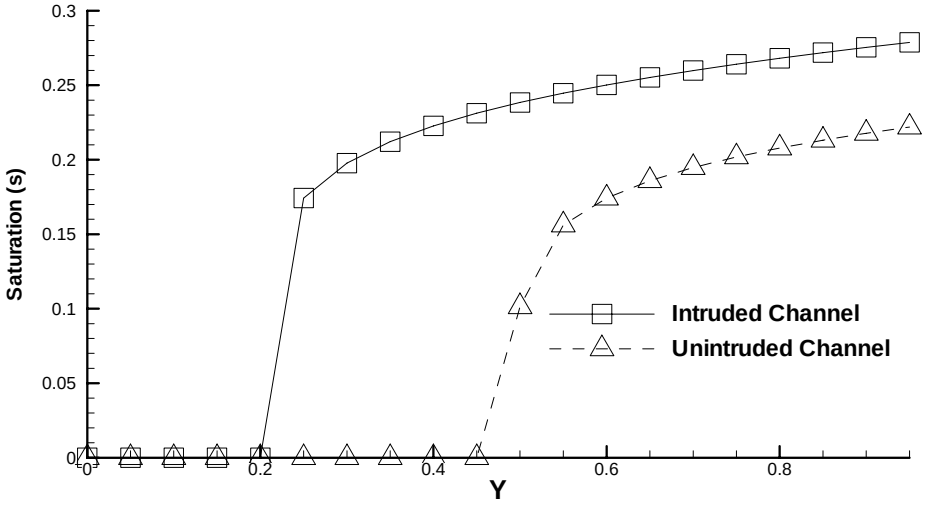

Figure **2-6**: Saturation Distribution for $\varepsilon = 0.5$ ($\bar{\xi}_c = 2.0$, RH=67%)**.**

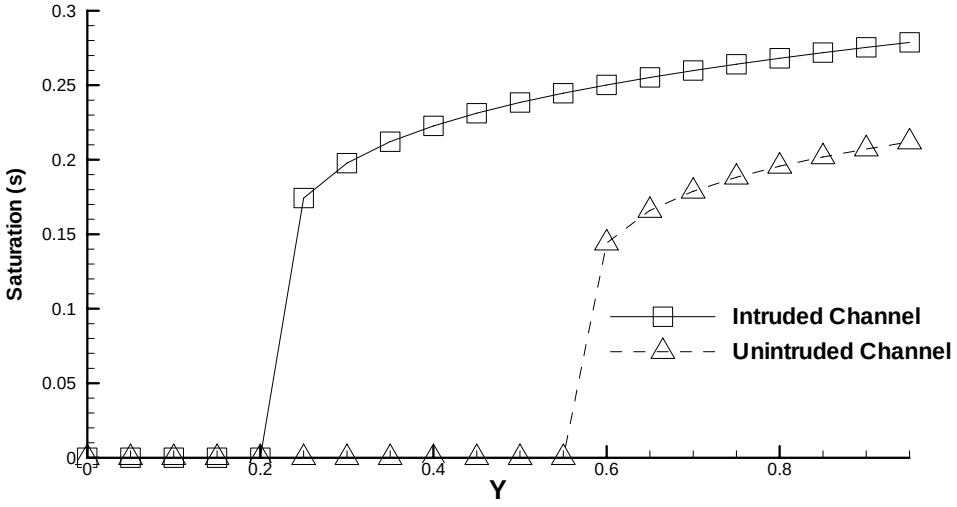

Figure **2-7**: Saturation Distribution for $\varepsilon = 0.9$ ($\bar{\xi}_c = 2.0$, RH=67%)**.**

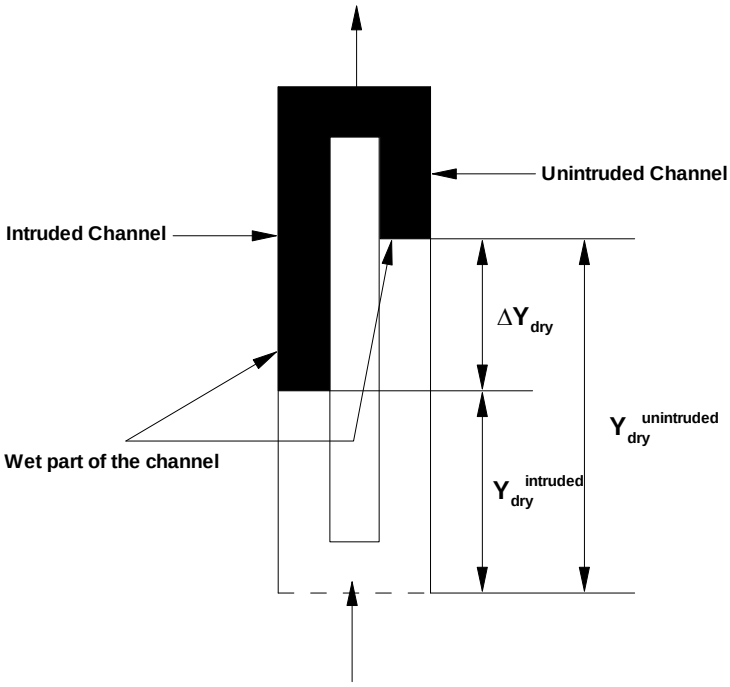

Figure **2-8**: Schematic of dry length in intruded and unintruded channels.

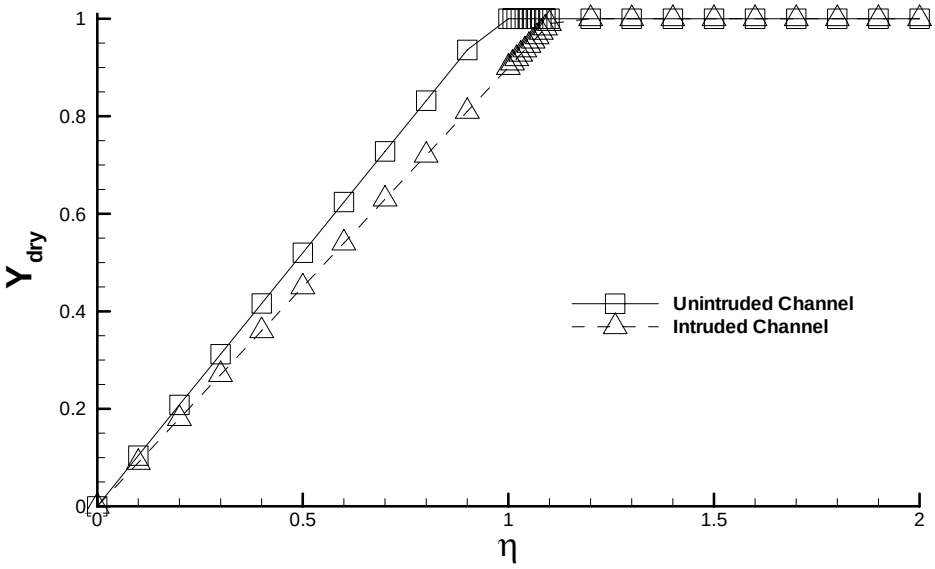

Figure **2-9**: Variation of dry length for intruded and unintruded channels at a flow maldistribution of 0.1.

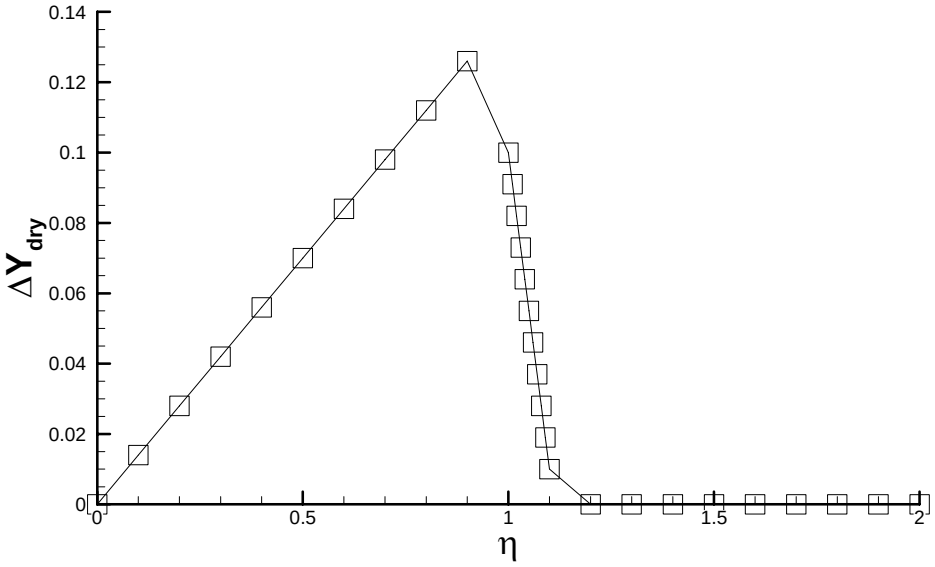

Figure **2-10**: Difference of dry length between intruded and unintruded channels at a flow maldistribution of 0.1.

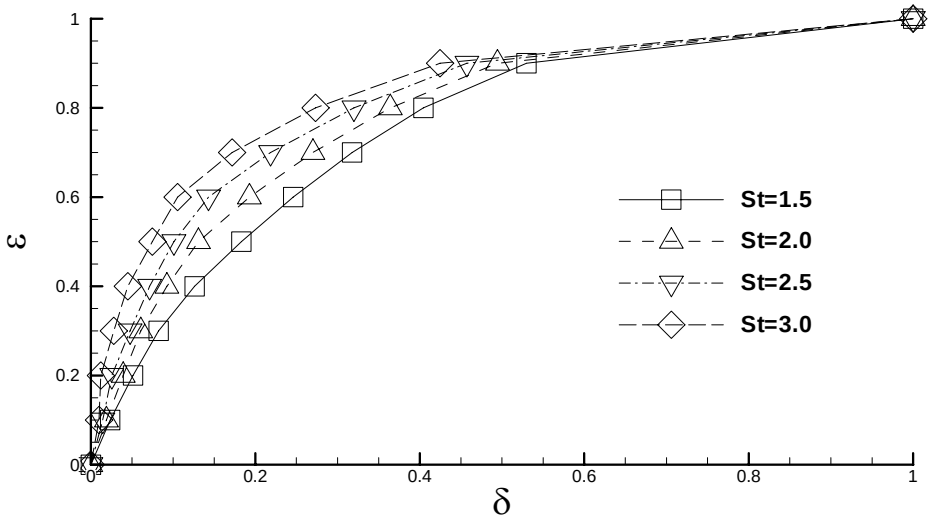

Figure **2-11**: Effect of global stoichiometry on maldistribution for inlet RH =67%.

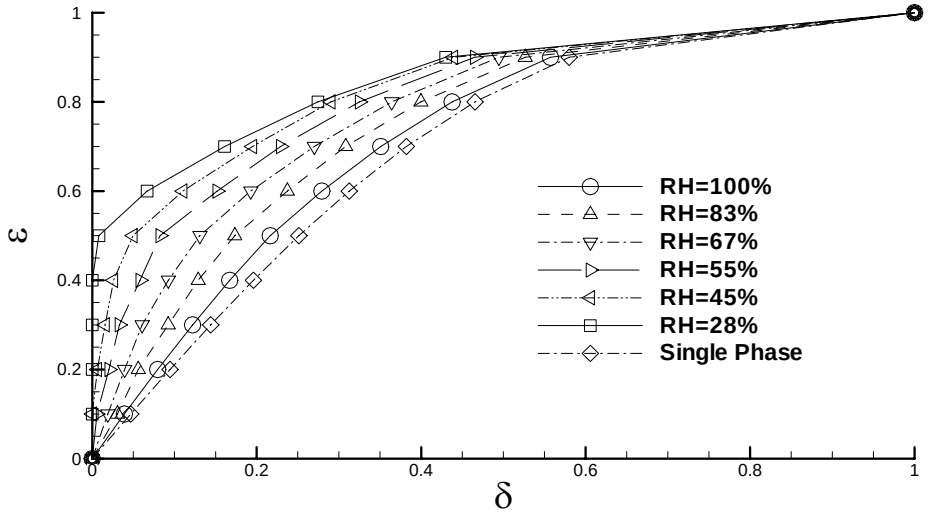

Figure **2-12**: Effect of air inlet relative humidity on flow maldistribution for $\overline{\xi}_c = 2.0$

.

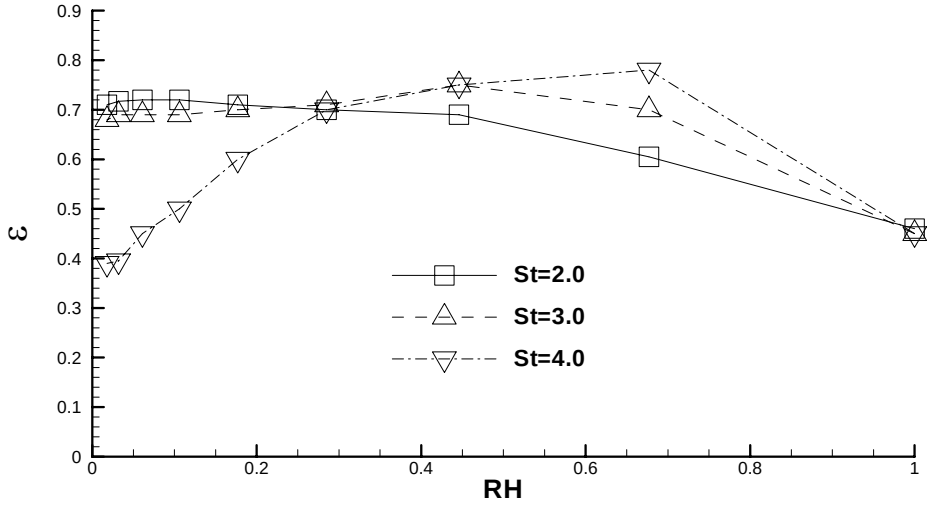

Figure **2-13**: Effect of Relative Humidity on flow maldistribution $(\delta = 0.2)$**.**

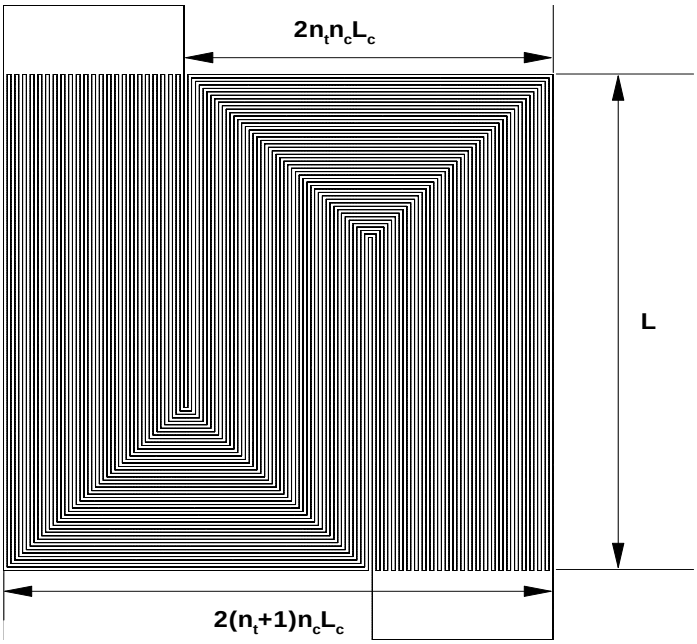

Figure **2-14**: A typical serpentine channel flow field.

Chapter 3

Two-Phase Flow and Maldistribution in Cathode Channels of a Polymer Electrolyte Fuel Cell

Introduction

A semi-analytical solution for two-phase flow and pressure drop through parallel channels of a PEM fuel cell has been shown in the previous chapter. The analytical model can capture the two-phase flow physics for simple parallel channel geometries. But higher dimensional effects and complex geometry, for example inlet and exit header for a multiple parallel channel PEFC, can not be modeled using this. The novel approach of treating fuel cell channels as a structured porous medium with straight capillary pores is continued here[38]. Following the M^2[41, 42] formulation a two-phase flow model is developed for the cathode channels of a PEFC. The electrochemical reactions are not computed but result of that is distributed in the channel space evenly using source terms.

Physical and Numerical model

Two-phase mixture flow and water transport in the channels are governed by the laws of momentum, mass and species conservation.

Mixture continuity equation:

$$\nabla \cdot \left(\rho \vec{u} \right) = S_m \tag{3.1}$$

Mixture momentum conservation:

$$\rho\vec{u} = -\frac{K}{\nu}\nabla P \tag{3.2}$$

Water species conservation:

$$\nabla\cdot(\gamma_c \vec{u} C^W) = \nabla\cdot(D_g^{W,eff}\nabla C_g^W) - \nabla\cdot\left[\left(\frac{mf_l^W}{M^W} - \frac{C_g^W}{\rho_g}\right)\vec{j}_l\right] + S_w \tag{3.3}$$

The mass source term in Eq. **3.1** is the net mass source in the cathode gas channels due to oxygen diffusing out of and water diffusing in to the channels. In reality product water and heat are injected into the channel from the GDL-channel interface and a proportional amount of oxygen is transported through the same interface. As we are modeling only the gas channel the excess mass is added to the continuity equation as a source term. The source term is calculated as,

$$S_m = (M^w S_w - M^{O_2} S_{O_2}) \tag{3.4}$$

M^w and M^{O_2} are the molecular weights of the water and oxygen respectively. The water and oxygen production rate (S_w and S_{O_2}) could be calculated from the Faraday relations as the following:

$$S_w = \frac{(1+2\alpha)IA_{membrane}}{2FV_{channel}} \text{ and } S_{O_2} = -\frac{IA_{membrane}}{4FV_{channel}} \tag{3.5}$$

where, α is the net water transport coefficient per proton which describes the combined effect of water diffusion and electro-osmotic drag and usually has a positive value. Assuming the net water transport coefficient to be equal to zero we get after some algebraic manipulation

$$S_m = \frac{M^{H_2} I A_{membrane}}{2FV_{channel}} \quad (\mathbf{3.6})$$

In the gas channels we neglect the effect of capillary and molecular diffusion as the flow is highly advection dominated. Simple order of magnitude analysis shows that the molecular diffusion Peclet number in the channel is ~10^{-4}, while the capillary diffusion is 3-4 orders of magnitude less than the molecular diffusion. Therefore the last two terms in the right hand side of the Eq. **3.3** are neglected. Also in steady state the unsteady term of Eq. **3.1**- Eq. **3.3** is neglected.

In Eq. **3.1** and Eq. **3.2**, the mixture density is defined using the M^2 formulation[8, 9]:

$$\rho = \rho_l s + \rho_g (1 - s) \quad (\mathbf{3.7})$$

Where ρ_l is the density of liquid water, ρ_g is the density of gas mixture and s is liquid saturation defined by

$$s = \frac{C^W - C^W_{sat}}{\rho_l / M^{H2O} - C^W_{sat}} \quad (\mathbf{3.8})$$

where C^W_{sat} is the saturation molar concentration at the cell temperature.

The kinematic viscosity of the mixture is defined as,

$$\nu = \left(\frac{k_{rl}}{\nu_l} + \frac{k_{rg}}{\nu_g} \right)^{-1} \quad (\mathbf{3.9})$$

where, ν_l and ν_g are the kinematic viscosities of water in liquid and vapor phase respectively, while k_{rl} and k_{rg} are the relative permeabilities of liquid and vapor phase respectively.

In Eq. **3.3** the convective correction factor is defined as:

$$\gamma_c = \frac{\rho}{C^W}\left(\frac{\lambda_l}{M^{H_2O}} + \frac{\lambda_g}{\rho_g} C^W_{sat}\right) \quad \textbf{(3.10)}$$

where the relative movements are defined as

$$\lambda_l = \frac{k_{rl}/v_l}{k_{rl}/v_l + k_{rg}/v_g} \text{ and } \lambda_g = 1 - \lambda_l \quad \textbf{(3.11)}$$

The relative permeability of different phases (i.e. k_{rl} and k_{rg}) could be modeled through numerical experiment [11]. Traditionally, for carbon-fiber based porous media the relative permeabilities of different phases were defined according to power law functions,

$$k_{rl} = s^{n_k} \quad \textbf{(3.12a)}$$

$$k_{rg} = (1-s)^{n_k} \quad \textbf{(3.12b)}$$

The value of the exponent n_k could be set to different values depending on the physical situations.

In a micro and mini-channels, a certain amount of water once accumulated could never be flushed out due to wall adhesion at the angles. This is called irreducible liquid saturation (s_{ir}). In a porous media this saturation reduces the pore size permanently. Therefore the relative permeabilities of different phases depend, not on the absolute liquid saturation but on the saturation corrected considering the irreducible part. The irreducible liquid saturation can be calculated from the empirical relations,

$$s_{ir} = \frac{1}{20 + 0.9Bo}\text{; Saez and Carbonell}^{43} \quad \textbf{(3.13)}$$

where the input is the Bond number (Bo). The Bond number is the ratio of body-force due to gravity in a channel to the surface tension force defined as,

$$Bo = \frac{\rho_l g d_h^2}{\sigma} \tag{3.14}$$

where, ρ_l is the density of the liquid water, g is the gravitational acceleration, d_h is the hydraulic diameter of the channel, σ is the surface tension coefficient. The hydraulic diameter is computed as,

$$d_h = 4\frac{\text{cross - section area}}{\text{channel perimeter}} \tag{3.15}$$

The irreducible liquid saturation is used to get a corrected form of the liquid saturation. We might call this corrected form the mobile liquid saturation. Both the liquid saturation and open space are decreased due to the irreducible liquid saturation. The ratio of these reduced quantities is defined as the mobile liquid saturation.

$$s_{mobile} = \frac{s - s_{ir}}{1 - s_{ir}} \tag{3.16}$$

In the Eq. **3.12** , liquid saturation is replaced with the newly defined mobile liquid saturation. But the saturation of the vapor water is kept the same as irreducible liquid saturation has no effect of the mobility of the vapor phase. So we are using the functions displayed in Eq. **3.17** as the relative permeabilities of liquid and gas phase respectively.

$$k_{rl} = \left(s_{mobile}\right)^{n_k} = \left(\frac{s - s_{ir}}{1 - s_{ir}}\right)^{n_k} \tag{3.17a}$$

$$k_{rg} = (1 - s_{mobile})^{n_k} \tag{3.17b}$$

The value of n_k is determined by numerical experiments against experimental data [38, 44].

Boundary Conditions

The cathode inlet flow is assumed to be dry (or at the most fully saturated). The inlet velocity (u_{in}) is calculated in terms of cathode stoichiometry (ξ_c), average current density (I_{avg}), inlet density (ρ_{in}), mole fraction of oxygen (C^{O_2}) and the cross-section areas of membrane and inlet (A_{mem} and A_{in} respectively) as the following,

$$u_{in} = \frac{\xi_c I_{avg} A_{mem}}{4FC^{O_2} A_{in}} \quad \textbf{(3.18)}$$

Where, F is the Faraday constant.

The molar concentrations at the inlet are determined by the inlet pressure and humidity according to the ideal gas law.

The exit boundary is assumed to be fully developed with,

$$\frac{\partial \vec{u}}{\partial n} = 0 \, , \, p = p_{ref} \, , \frac{\partial C^W}{\partial n} = 0 \quad \textbf{(3.19)}$$

In our case reference pressure is set at 2 Atm.

According to the assumption of Darcy's law the wall boundaries of the gas channel is free shear. Therefore, at all the walls we have,

$$\vec{u}.\hat{n} = 0 \, , \frac{\partial p}{\partial n} = 0 \, , \frac{\partial C^W}{\partial n} = 0 \quad \textbf{(3.20)}$$

Results and Discusion

Calibration

Numerically predicted pressure is compared with the experimental data for different value of the exponent n_k. Three representative cases are shown here (Figure **3-1**): I_{avg} = 0.8 A/cm^2, Stoichiometry= 4.0, I_{avg} = 0.5 A/cm^2, Stoichiometry= 3.0, I_{avg} = 0.2 A/cm^2, Stoichiometry= 2.0. These cases cover most of the operating range of PEFC. From the plot, n_k =5.0 is found to yield the best result.

Parallel Channel

The cathode channel flooding experiments are conducted using a test cell consisting of seven parallel channels of 1mm x 20 mm (shown in Figure **3-2**). Two dimensional computations are carried out first for a seven channel case without the GDL intrusion. Three current density (I_{avg} =0.8A/cm^2, 0.5A/cm^2, 0.2A/cm^2) and three stoichiometries (2.0, 3.0, 4.0) are chosen for the parametric study. The resulting nine cases cover most of the operating range of the PEFC. Although, higher current density operations are feasible with present technology, at high current density there is less chance of flooding. Therefore we set the upper bound of current density at 0.8A/cm^2.

At high current density and high stoichiometry (I_{avg} =0.8A/cm^2, Stoichiometry =4.0) several channels are completely dry (Figure **3-3**). The liquid front is pushed downstream in all the channels. For the channels closer to the inlet the flow resistance is

much higher due to the presence of liquid water in the exit manifold. Therefore the flow velocity is smaller in these channels and the liquid front appears upstream than other channels.

At medium current density and medium stoichiometry (I_{avg} =0.5A/cm^2, Stoichiometry =3.0) the liquid saturation distribution is more even, as shown in Figure **3-4**. Only the channel closest to the outlet is completely dry. This channel being close to the exit has a very small resistance to due to wet exit manifold. Therefore flow velocity is high in this channel and as a result it can blow all the liquid away, while in the other channels the liquid saturation front is much upstream.

At low current density and low stoichiometry the channels are almost totally flooded, as displayed in Figure **3-5**. At such low flow rate it is not possible to flush out liquid water from any of the channels.

The relative stoichiometry in different channels for two representative cases (I_{avg} =0.8A/cm^2, Stoichiometry =4.0 and I_{avg} =0.2A/cm^2, Stoichiometry =2.0) are plotted in Figure **3-6**. The channels are numbered starting from the nearest to the inlet. Liquid saturation is high for the channels close to the inlet and low for the channels far from the inlet. The channels close to the inlet experience the extra resistance due to the wet exit manifold and hence flow rate is low in those channels. Therefore, more liquid water is condensed in the channels near the inlet while in the far out channels could effectively flush out all the water. But interestingly the maldistribution decreases significantly between low current density low stoichiometry cases to high current density high stoichiometry case.

The same parametric study is performed with GDL intrusion in the gas channels. Here we assume 20% loss in the cross section area at the end channels due to the assembly procedure. The same range of parameters is chosen as before. The volumetric water source term and flow resistance is corrected at the end channels according to the intrusion.

The liquid saturation contour at I_{avg} =0.8A/cm^2, Stoichiometry =4.0 displayed in Figure **3-7** is completely different from the perfect channel case. The end channels are wet due to the effect of enhanced flow resistance. The resulting high flow rate could flush out the liquid water from the middle channels while the end channels register high liquid saturation. The maximum liquid saturation is higher in the case of intruded channel case than the perfect channels.

For I_{avg} =0.5A/cm^2, Stoichiometry =3.0 the liquid saturation as displayed in Figure **3-8** is much severe than the perfect channel case. The liquid saturation fronts are much upstream and the maximum liquid saturation is higher as well.

For I_{avg} =0.2A/cm^2, Stoichiometry =2.0, the liquid water as displayed in Figure **3-9** could be found in every channel. The liquid water front appears more upstream than any other channels. The liquid saturation fronts appear much upstream for the others channels when compared to the perfect channel case. The maximum liquid saturation is higher as well.

The relative stoichiometry in different channels for two representative cases (I_{avg} =0.8A/cm^2, Stoichiometry =4.0 and I_{avg} =0.2A/cm^2, Stoichiometry =2.0) are plotted in Figure **3-10**. The channels are number starting from the nearest to the inlet. But

interestingly the maldistribution decreases significantly between low current density low stoichiometry cases to high current density high stoichiometry case. The reason for that is, at low flow rate cases the flushing ability of the flow is reduced and so liquid water condenses in all the channels, ensuing two-phase flow in each of the channels. Once there is two-phase flow in all the channels the difference between flow resistances decreases and that finally results in less flow maldistribution. Although high liquid saturation in the end channels take these very close to getting clogged.

A comparison between the numerically predicted liquid saturation contour and the visualization experiment at I_{avg} =0.8A/cm^2, Stoichiometry =2.0, Dew Point Temperature 70^{o}C is displayed in Figure **3-11**. The numerical prediction matches very well with the experimental result for most of the channels. However, experiments have suggested that the flow in the gas channels is inherently unsteady while our present model is a steady state model.

Conclusions

It is important to have a two-phase model that can estimate the liquid saturation and pressure drop across the cathode channels. The two-phase flow in the channels is computed by M^2 model for the first time. The two-phase pressure drop coefficient predicted by M^2 model is found to be in good agreement with experimental measurements. Flow maldistribution among parallel channels is clearly captured by the present model, and effects of GDL intrusion at the edge channels are assessed. The predicted liquid saturation contours show qualitative agreement with experimental

observations via optical visualization. This agreement further bolsters the assumption of GDL intrusion in the channels. However, the ad-hoc assumption on the extent of intrusion may need to be further verified from the experiments.

Figures

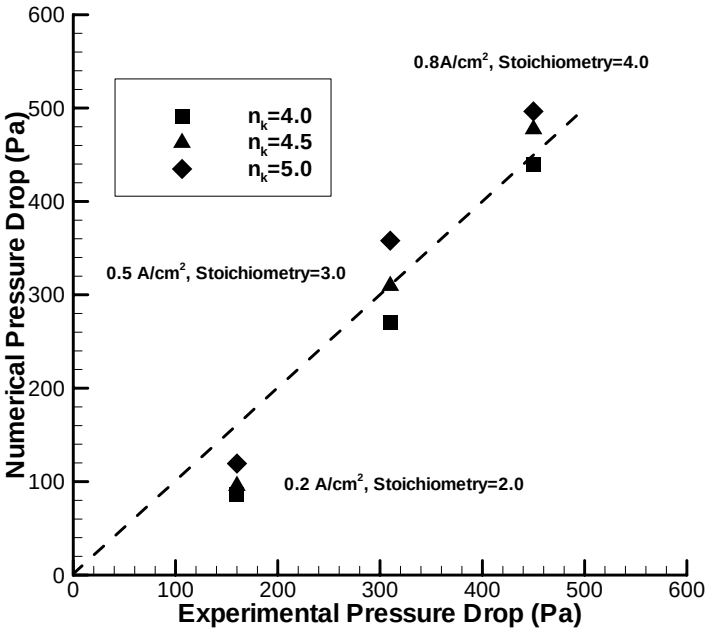

Figure **3-1**: Calibration of the Exponent.

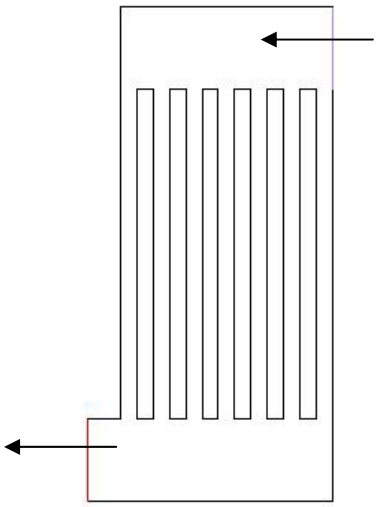

Figure **3-2**: The Computational Domain.

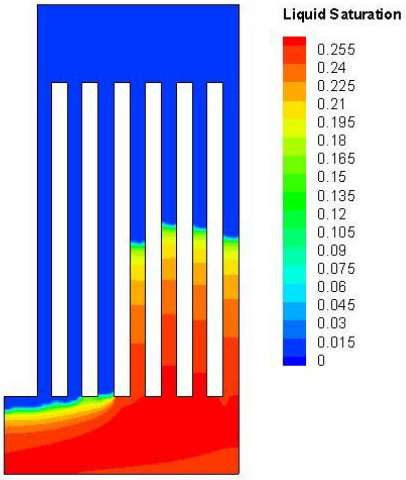

Figure **3-3**: I= 0.8A/ cm^2 and Stoichiometry = 4.0.

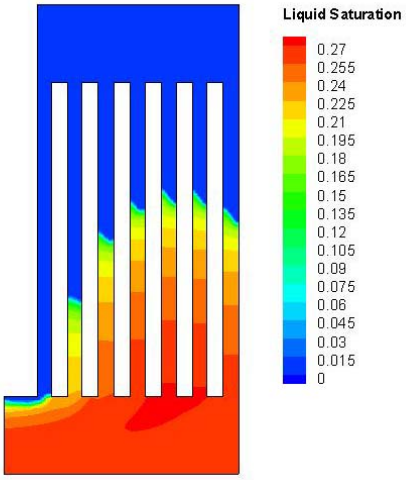

Figure **3-4**: I= 0.5A/ cm^2 and Stoichiometry = 3.0.

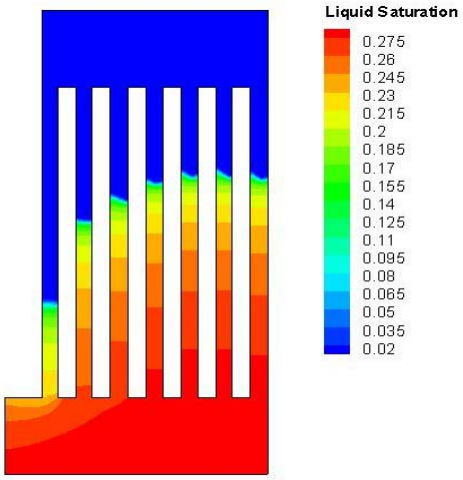

Figure **3-5**: I= 0.2A/ cm^2 and Stoichiometry = 2.0.

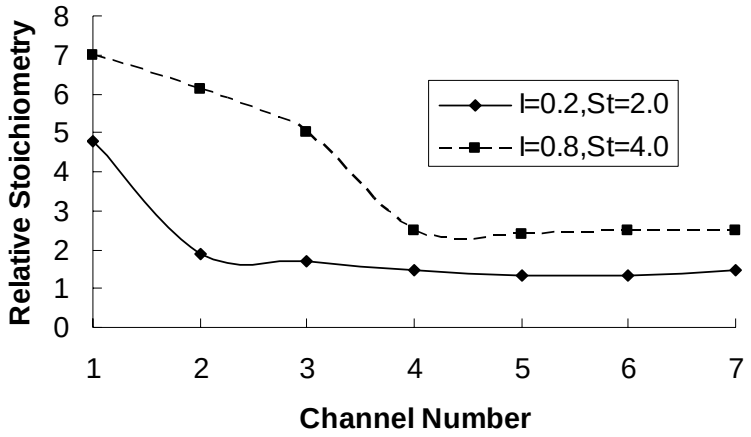

Figure **3-6**: Flow maldistribution in the parallel channels.

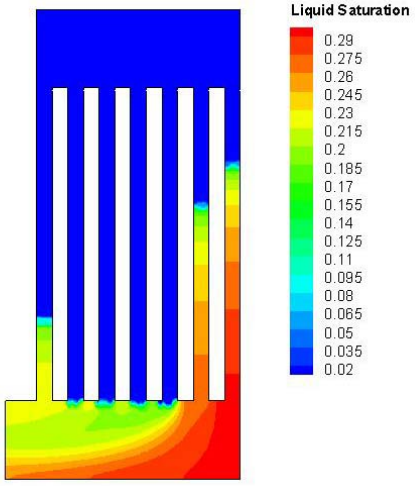

Figure **3-7**: I= 0.8A/ cm^2 and Stoichiometry = 4.0.

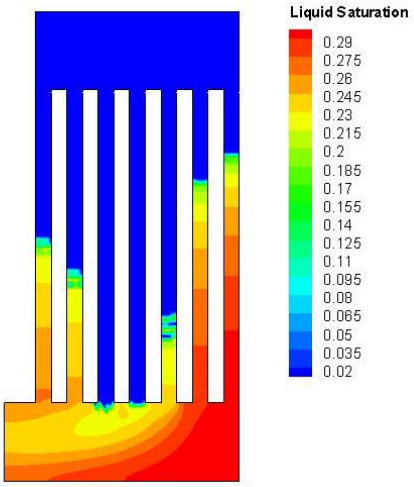

Figure **3-8**: I= 0.5A/ cm^2 and Stoichiometry = 3.0.

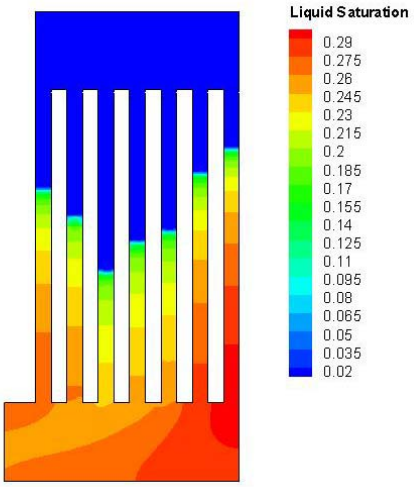

Figure **3-9**: I= 0.2A/ cm^2 and Stoichiometry = 2.0.

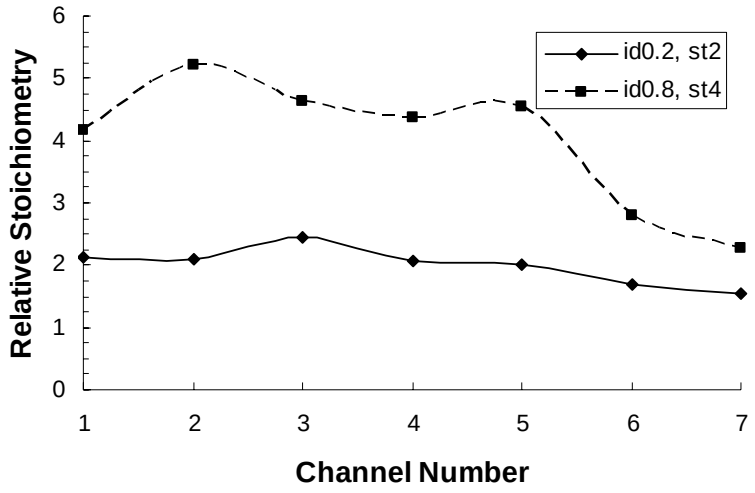

Figure **3-10**: Flow maldistribution in the parallel channels.

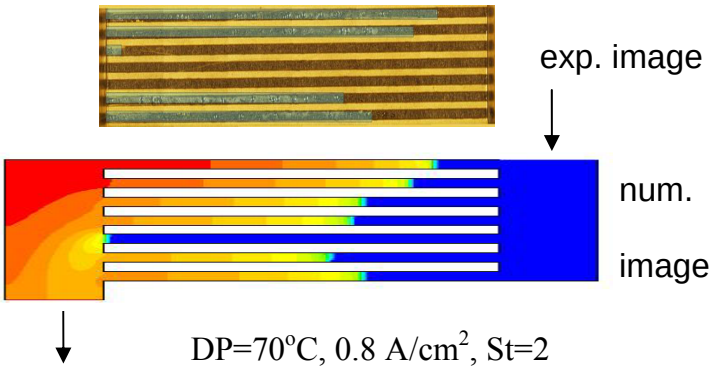

Figure **3-11**: Comparison with visualization experiment.

Chapter 4

Two-Phase Flow and Maldistribution in an Operating Polymer Electrolyte Fuel Cell

Introduction

A typical PEFC and its components are schematically displayed in Figure **4-1**. In the present work, we first couple a recently developed two-phase channel flow model with other two-phase models for the catalyst layer and GDL previously developed in our laboratory to form a complete two-phase model for an entire PEFC. The channel two-phase model[46, 67] is based on the framework of multiphase mixture model (M^2 model) and capable of predicting the liquid water volume fraction and pressure along the flow direction. Then, the complete model is validated against experimental data of wetted area ratio and pressure drop over a range of operating conditions. Finally, this complete two-phase model is employed to study the effects of GDL intrusion and manifold design on reducing flow maldistribution.

Mathematical Model

A PEFC consists of seven sub regions - anode gas channel, anode GDL, anode catalyst layer, ionomeric membrane, cathode catalyst layer, cathode GDL and cathode gas channel. In addition, the electron transport through bipolar plates may be important in some cases. The membrane is a solid state electrolyte with water and proton co-transport taking place through its ionomer phase.

Two-phase flow and transport in a PEFC are governed by the laws of momentum, mass, energy, species and charge conservation. Under non-isothermal, two-phase conditions the conservation equations of mass, momentum, energy, species and charge equations in the PEFC can be written as[65, 68, 69]:

$$\text{Mass: } \nabla \cdot (\rho \vec{u}) = 0 \tag{4.1}$$

$$\text{Momentum: } \frac{1}{\varepsilon^2} \nabla \cdot (\rho \vec{u}\vec{u}) = -\nabla P - \nabla \cdot (\tau) + S_u \tag{4.2}$$

$$\text{Energy: } \nabla \cdot (\gamma_T \rho C_p \vec{u} T) = \nabla \cdot (k_{eff} \nabla T) + S_T \tag{4.3}$$

$$\text{Species: } \nabla \cdot (\gamma_c \vec{u} C^k) = \nabla \cdot (D_g^{k,eff} \nabla C_g^k) - \nabla \cdot [(\frac{m f_l^k}{M^k} - \frac{C_g^k}{\rho_g}) \vec{j}_l] + S_k \tag{4.4}$$

$$\text{Charge (electrons): } \nabla \cdot (\sigma^{eff} \nabla \Phi_s) + S_{\Phi_s} = 0 \tag{4.5}$$

$$\text{Charge (Protons): } \nabla \cdot (k^{eff} \nabla \Phi_e) + S_{\Phi_e} = 0 \tag{4.6}$$

The source terms are tabulated in **Table 4-1**. Details about these equations and the source terms are available in the literature[65, 69]. The present modeling approach is to view all components in a PEFC as porous media. Specially, we model flow channels of typical dimension between 0.2 and 1 mm as a structured porous media or a bundle of straight capillary tubes. Hence, we apply the two-phase flow theory based on extended Darcy's law to describe two-phase flow and transport throughout an entire PEFC including the flow channels. Furthermore, for convenience of numerical implementation, the two-phase theory in porous media is formulated into M^2 model without making any additional assumptions. The validity of this porous medium approach for channel two-phase flow encountered in PEFCs has been explored in detail in earlier chapters.

Assuming a local thermodynamic equilibrium between the liquid and vapor phases in the two-phase region, the water concentration in the vapor phase could be taken

as equal to the saturation water concentration that solely depends on the temperature. Since the liquid phase consists of only water, the water mole fraction in the liquid is equal to unity. Therefore the total water concentration C^{H_2O} to be solved by Eq. **4.3** can be written as:

$$C^{H_2O} = sC_l^{H_2O} + (1-s)C_g^{H_2O} = s\left(\rho_l / M_{H_2O}\right) + (1-s)C_{sat}^{H_2O} \tag{4.7}$$

where s is the liquid water saturation or volume fraction. From Eq. **4.7**, the liquid saturation or volume fraction can be calculated from [65]:

$$s = \frac{C^{H_2O} - C_{sat}^{H_2O}}{\rho_l / M_{H_2O} - C_{sat}^{H_2O}} \tag{4.8}$$

Within the M^2 model framework, the kinematic viscosity of the two-phase mixture is defined as:

$$\nu = \left(\frac{k_{rl}}{\nu_l} + \frac{k_{rg}}{\nu_g} \right)^{-1} \tag{4.9}$$

where ν_l and ν_g are the kinematic viscosities of liquid and gas phases respectively, while k_{rl} and k_{rg} are the relative permeabilities of liquid and vapor phases respectively.

Water is the only species that could be present in both liquid and vapor states. Therefore, the correction factor takes into account contributions due to both phases for water conservation equation. Other species can be present in only the gas phase. The species correction factor (γ_c) can be derived as follows [28]:

$$\gamma_c = \begin{cases} \dfrac{\rho}{C^{H2O}}\left(\dfrac{\lambda_l}{M^{H2O}} + \dfrac{\lambda_g}{\rho_g} C_{sat}\right) \\ \dfrac{\rho\lambda_g}{\rho_g(1-s)} \end{cases} \tag{4.10}$$

The mobility of each phase $\lambda_l(s)$ and $\lambda_g(s)$ are defined in Eq. **4.11** and Eq. **4.12** in terms of the relative permeabilities of the liquid and gas and phases:

$$\lambda_l(s) = \frac{k_{rl}(s)/v_l}{k_{rl}(s)/v_l + k_{rg}(s)/v_g} \tag{4.11}$$

$$\lambda_g(s) = 1 - \lambda_l(s) \tag{4.12}$$

Two most important parameters to describe two-phase flows through a porous medium are relative permeability and capillary pressure functions. The relative permeabilities used in this work can be expressed as:

$$k_{rl} = s^{n_k} \tag{4.13}$$

$$k_{rg} = (1-s)^{n_k} \tag{4.14}$$

where exponent n_k varies depending on the flow conditions and porous medium microstructures. Different values have been used for n_k [28, 65, 70] depending on flow situations. More recently it was found[46] that in the PEFC flow channels the value of n_k equal to 5 results in the best match with experimental pressure drop data. Therefore in the present case, we use n_k equal to 5.0 in the channel and 4.0 otherwise.

Capillary pressure is usually expressed as Leverett function of the liquid saturation such that:

$$P_c = \sigma \cos(\theta_c)\left(\frac{\varepsilon}{K}\right)^{1/2} J(s) \qquad \textbf{(4.15)}$$

We use the Leverett $J(s)$ function given by [71]:

$$J(s) = \begin{cases} 1.417(1-s) - 2.120(1-s)^2 + 1.263(1-s)^3 & \text{for } \theta_c > 90^o \\ 1.417s - 2.120s^2 + 1.263s^3 & \text{for } \theta_c < 90^o \end{cases} \qquad \textbf{(4.16)}$$

The absolute permeability K for the flow channels can be computed by numerical experiments of simulating single-phase flow through the flow channels. In the case of GDL intrusion, the channel cross-sectional area decreases. This would result in reduction in the absolute permeability. Consider that the absolute permeability through a minichannel can be expressed by[46]:

$$K = c\frac{d_h^2}{32} \qquad \textbf{(4.17)}$$

where c is the shape factor describing various shapes of the channels and d_h is the hydraulic diameter of the channel. Thus, one can use the following approximate expression for the absolute permeability in the intruded channels:

$$K_{\text{int}\,ruded} = K_{un\,\text{int}\,uded}\left(1-\delta\right)^2 \qquad \textbf{(4.18)}$$

where δ is the fraction reduction in the channel height due to GDL intrusion.

Boundary Conditions

The inlet velocity (u_{in}) is calculated in terms of cathode stoichiometry (ξ_c), average current density (I_{avg}), active area of the membrane (A_{mem}), molar concentration of oxygen (C^{O_2}) and the cross-sectional area of channels (A_{in}) as the following:

$$u_{in} = \frac{\xi_c I_{avg} A_{mem}}{4FC^{O_2} A_{in}} \quad (\mathbf{4.19})$$

where F is the Faraday constant.

The molar concentrations of species at the inlet are determined by the inlet pressure and humidity according to the ideal gas law.

The exit boundary is assumed to be fully developed namely:

$$\frac{\partial \vec{u}}{\partial n} = 0 \, , \, p = p_{ref} \, , \frac{\partial C^k}{\partial n} = 0 \quad (\mathbf{4.20})$$

In this work the reference pressure is 2 Atm.

At all wall boundaries we have:

$$\vec{u}.\hat{n} = 0 \, , \frac{\partial p}{\partial n} = 0 \, , \frac{\partial C^k}{\partial n} = 0 \quad (\mathbf{4.21})$$

Numerical Procedures

The governing equations, Eq. **4.1 - 4.6**, along with their appropriate boundary conditions are discretized by the finite volume method and solved in a commercial flow solver, Fluent (version 6.1.22), by SIMPLE algorithm. The source terms and physical

properties are implemented using the user-defined functions (UDF) available with commercial CFD software Fluent 6.1. Overall species balance and charge balance are checked in addition to the equation residuals as important convergence criteria. The cell geometry and the simulation parameters are listed in Table **4-2** and Table **4-3**. In the simulations to be presented below, all species imbalances are less than 1% and residuals smaller than 10^{-5}.

Results and Discussion

Experimental Validation

The most important predictive capabilities of our model include the fraction of the wet GDL-channel interface and the total two-phase pressure drop through the flow channels. Prediction of these quantities is therefore validated against the recent experiments of Hussaini and Wang[10]. A seven parallel channel 14 cm^2 active area cell, shown schematically in Figure **4-1**, is used in these experiments. The channels are 1 mm x 0.5 mm in cross section and 100 mm in length. The membrane active area is 14 mm in width and 100 mm in length and the membrane is 30μm thick Gore composite membrane. The computational mesh for this cell consists of 0.15 million grid points.

The wet area on the GDL-channel interface (covered partially by liquid water), is quantified from the flow visualization experiment on the seven-channel PEFC. The ratio of the wet area to the total GDL-channel interface area is defined as the “wetted area ratio”. An average of the wetted area ratio over the entire cell including all the channels is

taken as the wetted area ratio for the PEFC at that operating condition. The wetted area ratio is a strong function of three operational parameters – the average current density, the air stoichiometry and the relative humidity at the cathode inlet. The computed wetted area ratio in the cathode side is compared with the experimental data over a range of these operating conditions in Figure **4-2** through Figure **4-4**. Figure **4-2** depicts the model-experimental comparison for relative humidities of 67%, 45% and 25% at I_{avg}=0.2A/cm^2 with cell temperature of 80^{o}C. Overall, good agreement is found. At a medium current density of 0.5A/cm^2, the match shown in Figure **4-3** is also reasonable except that the present model overpredicts at relative humidity of 67% for large air stoichiometry. The match between experimental results and numerical predictions shown in Figure 4 is again good at a high current density of 0.8A/cm^2. These comparisons shown in Figures 2 through 4 demonstrate that our model can predict the wetted area ratio reasonably well for a range of practical operating conditions.

The wetted area ratio less than unity, as displayed in Figure **4-2** through Figure **4-4**, physically implies that the flow channels are partially dry (free of any liquid water) and partially wet due to liquid water accumulation, and that there exists a dry-to-wet transition within the channel length[5, 11]. The results shown in Figure **4-2** through Figure **4-4** clearly indicate that the flow channels have a longer wet portion under high inlet humidity, lower air stoichiometry and lower current density, as expected.

The pressure drop along the cathode channels of the PEFC is compared between experimental measurements of Hussaini[72] and the present calculations, as shown in Figure **4-5**. Note that GDL intrusion to reduce cross-sectional areas of flow channels must be accounted for, as intrusion of soft GDL material into flow channels is inevitable

during assembly of PEFCs. While it is difficult to quantify the degree of GDL intrusion *in-situ*, we found 33% GDL intrusion at the edge channels yields a reasonable match with the experimental pressure drop data for all current densities, as shown in Figure **4-5**. The agreement is poor, particularly for the low current density of 0.2A/cm^2. This may be due to the inadequacy of the present M^2 model to describe significant two-phase flow occurring at low current densities. Future investigation is needed to improve model accuracy in this regime.

Flow Maldistribution and Its Effect on Cell Performance

While experimental validation has been carried out for system parameters, in this subsection we reveal the two-phase flow maldistribution in an operating PEFC and the impact on cell performance using the present model. All cases presented below use the cell temperature of 80^{o}C and relative humidity of 67%, most typical of automotive applications. The effect of GDL intrusion is studied for high current density (0.8A/cm^2) and low stoichiometry (2.0). GDL intrusion of 17% and 33% at the two edge channels are considered to investigate the variation of flow maldistribution and the pressure penalty. The area maldistribution due to GDL intrusion changes the distribution of liquid water among channels and furthermore, interacts with the non-linear characteristics of two-phase flow to result in significant non-uniform distribution of reactants. Results of perfectly symmetric and intruded flow channels are compared and analyzed.

The current density distributions at the center of the membrane for perfect channels, 17% intruded channels and 33% intruded channels are displayed in Figure **4-6**.

The contour shows somewhat symmetric current distribution over all seven channels for the prefect channel case. The slight non-uniformity among channels is caused by the fact that both inlet and outlet manifolds are included in the present computations. Flow resistance in the outlet manifolds of anode and cathode differs from that of the inlet manifold due to the presence of two-phase flow and changes with operating conditions. For the 17% intruded channels, there is an additional reduction in the flow cross-section of the two edge channels and the local current density there is lower. This uneven distribution in current density from channel to channel is more severe for the 33% intrusion. Clearly, this is caused by low reactant flows through the intruded channels. Furthermore, it is seen from Figure **4-6** that local current density is usually smaller over the area of a land separating two flow channels. Note that the two edge channels are bounded by a half land on the edge of the cell. The low current density regions resulting from flow maldistribution decreases cell performance as well as the utilization of precious-metal catalysts.

The pressure contours along the cathode channels are shown in Figure **4-7** for the same cases. The pressure penalty increases by about 10% for the 33% GDL intrusion. Interestingly, the predicted pressure drop for 33% intrusion is closest to the experimental measurement. The experimental pressure drop for this case is 460 Pa and numerically predicted pressure drop is 423 Pa. At the same time the pressure drop for perfect channels is much less than the experimental data. This suggests the presence of GDL intrusion in flow channels and the extent of area maldistribution likely to be close to 33%. The liquid volume fraction contours in the cathode channels for the same cases are displayed in Figure **4-8**. The dry-to-wet transition is clearly visible in all cases. With GDL intrusion,

the maximum liquid volume fraction occurs in the intruded channels and the liquid front is pushed considerably upstream. This is because the intruded channels feature larger flow resistance and hence lower gas velocity, thereby accumulating more liquid water. The presence of more liquid water further increases the flow resistance and reduces the gas flow through the channel. This feedback mechanism results in a 'U' shape of flow distribution across seven channels.

The liquid water saturation in the midsection of the cathode GDL for these three cases is plotted in Figure **4-9**. It is seen that the liquid saturation is much higher in the GDL, reaching about 30%. Maximum liquid water saturation appears over the lands at about the mid-length of the channels. For the unintruded channels (Figure **4-9**a) the liquid water saturation profiles exhibit a similar pattern. Interestingly, Figure **4-9**b and c show that the liquid water saturation in the GDL decreases in the vicinity of the intruded channels, possibly due to lower current density (see Figure **4-6**b and c). The effect of GDL intrusion on cell operation can be summarized by comparing Figures **4-7**, **4-8** and **4-9**. The current production is low over the intruded channels due to low reactant flowrate. As a result, water production is low and therefore the liquid saturation in the GDL is low over the intruded edge channels. Intuition suggests that the liquid water would be less in the intruded channels since less water is produced, but the ability of these channels to remove liquid water out of the cell is so low that more liquid water accumulates in the intruded channels.

The pressure contours along the anode channels are shown in Figure **4-10** for the same three cases. Pressure penalty also increases in the anode side due to the presence of two-phase flow. However, the magnitude of the anode pressure drop is about 20% of the

cathode due to much lower hydrogen flowrate than air. The liquid water volume fraction contours along the anode channels are displayed in Figure **4-11**. Not only is the dry-to-wet transition captured in the anode channels but there is also a wet-to-dry transition. The latter transition occurs because the anode outlet is facing the cathode inlet where relatively dry air is fed into the cell which re-evaporates the liquid water in the anode channels. It is seen that GDL intrusion has a severe effect in the anode.

The liquid water saturation in the midsection of the anode GDL for these three cases is plotted in Figure **4-12**. It is seen that the liquid saturation is much higher in the GDL than the anode channels. The maximum liquid saturation occurs over the lands in the middle of the cell, ranging from 23% to 25%. Once again, for the unintruded channels (Figure **4-12**a) the liquid saturation profiles are relatively symmetric from channel to channel, while there is clearly more liquid water in the GDL over the land area towards the center of the cell with intruded edge channels. This behavior of liquid water maldistribution resembles the cathode side.

Flow and liquid water maldistribution can be better depicted by liquid water volume fraction contours in the center of the channels along the in-plane direction. Figure **4-13** compares these contour plots for a middle channel and an edge channel for the three cases of interest. For the perfect channels the axial profile of liquid water is very similar between the two channels (Figure **4-13**a). Along the cathode channel, a dry-to-wet transition can be seen, while the cathode exit always remains wet. In the anode channels, however, there exists dry-wet-dry transition, the physics of which has been elaborately discussed in the literature [69, 73], albeit in the absence of two-phase flow in channels. Our results illustrate a profound effect of two-phase flow in channels on the liquid water

distribution in the PEFC. That is, the wet-to-dry transition in the cathode is predicted without channel two-phase flow but not with the consideration of channel two-phase flow. This is because the channel two-phase flow allows for accumulation of a large amount of liquid water, which then becomes difficult to dry up by dry gas from the anode inlet. For the same reason, however, the anode flow stream is prone to dryout because the anode flowrate is only about one fifth of that of the cathode side.

The effect of area maldistribution on liquid water distribution is more evident from Figure **4-13**b. It is shown that the amount of liquid water is much higher in the edge channel section for 17% GDL intrusion. The dry-to-wet transition in the cathode occurs further upstream in the edge channel with respect to the middle channel. For the case with 33% GDL intrusion these effects are further magnified as shown in Figure **4-13**c. The difference in the maximum liquid water volume fraction between the channels is quite substantial. The wetted area is much higher for edge channels as well. Schematic diagrams illustrating the dramatic effect of GDL intrusion on liquid water distribution are given in Figures **4-14**a and b for the edge (intruded) and middle (unintruded) channels, respectively.

The local stoichiometry in each of the seven channels, defined as $\xi_{avg} \frac{Q}{Q_{avg}}$ with Q being the local gas flowrate through a certain channel, is shown in Figure 15 to quantify the degree of flow maldistribution. Such plots for both cathode and anode sides are shown in Figure **4-15**. The channels are numbered starting from the inlet in each case. It can be seen that the flow maldistribution is relatively minor in perfect channels and arises solely from two-phase flow. When GDL intrusion is considered, severe

maldistribution of flow develops in the edge channels. Area reduction of 17% at the edge channels results in about 25% reduction in flowrate. Similarly, for 33% area reduction at the edge channels, the reactant flow decreases by almost 50%, while the flows through the other channels without GDL intrusion do not vary much. These observations are true for both the cathode and anode channels. In the present cases, the average flow stoichiometry over the entire cell is 2.0 in both anode and cathode. A reduction of 50% flow means that the local stoichiometry is less than 1.0, insufficient to sustain the average reaction rate and potentially leading to detrimental side reactions such as oxygen evolution and carbon corrosion.

Conclusions

A channel two-phase flow model has been integrated with the previously developed two-phase PEFC model based on the M^2 framework. The complete PEFC model considering two-phase flow in channels is employed to explore flow maldistribution in an operating PEFC for the first time. The wetted area ratio on the cathode GDL surface predicted by the present model matches quantitatively with experimental data over a range of current density, relative humidity and flow stoichiometry. In addition, the overall pressure drop prediction is found to be good.

The effect of GDL intrusion at the edge channels, as commonly observed in a fuel cell stack, is numerically studied. Severe flow and liquid water maldistributions are predicted due to GDL intrusion in the edge channels. Low flowrate of the intruded channels make these regions starved of reactants, thus reducing the cell performance and

durability. Innovative flow field designs are needed to mitigate flow maldistribution and ensuing adverse impact on cell performance and durability.

Tables

Table **4-1**: Source terms for the conservation equations in each sub-region.

	S_u	S_T	S_C^{H2O}	S_C (for reactants)	$S_{\phi s}$	$S_{\phi e}$
Channels	0	0	0	0	0	-
Gas diffusion layers	$-\frac{\mu}{K_{GDL}}\vec{u}$	$\frac{i_s^2}{\sigma^{eff}} + h_{fg}\dot{m}_l$	$-\dot{q}_{gs}^{H_2O}$	0	0	-
Catalyst layers	$-\frac{\mu}{K_{CL}}\vec{u}$	$j\left(\eta + T\frac{\partial U_0}{\partial T}\right) + \frac{i_e^2}{\kappa^{eff}} + \frac{i_s^2}{\sigma^{eff}} + h_{fg}\dot{m}_l$	$-\nabla\cdot\left(\frac{n_d}{F}i_e\right) - \frac{s_k j}{nF}$	$-\frac{s_k j}{nF}$	$-j$	j
Membrane	-	$\frac{i_e^2}{\kappa^{eff}}$	$-\nabla\cdot\left(\frac{n_d}{F}i_e\right)$	0	-	0

Note: Electrochemical reaction where $\sum s_k M_k^z = ne^-$

$\begin{cases} M_k \equiv \text{chemical formula of species } k \\ s_k \equiv \text{stoichiometry coefficient} \\ n \equiv \text{number of electrons transferred} \end{cases}$

In PEFC, there are
(Anode) H_2-$2H^+$=$2e^-$
(Cathode)$2H_2O$-O_2-$4H^+$=$4e^-$

Table **4-2**: Cell geometry and properties**.**

Description	Value
Cell length	100.0 mm
Gas channel depth	0.5 mm
Gas channel width	1.0 mm
Land width	1.0 mm
Anode/cathode GDL thickness	0.20 mm
Anode/cathode catalyst layers thickness	0.010 mm
Porosity of anode/cathode GDL, ε_{GDL}	0.6
Porosity of anode/cathode catalyst layers, ε_{CL}	0.6
Volume fraction of ionomer in Anode/Cathode catalyst layers, ε_e	0.18
Hydraulic permeability of anode/cathode GDL, K_{GDL}	3.0×10^{-14} m^2
Hydraulic permeability of membrane, K_{mem}	5.0×10^{-20} m^2
Contact angle of anode/cathode channel, GDL and catalyst layers, θ	60^o, 110^o,110°
Contact resistance between catalyst layer and GDL, R_{GDL}	$1.0\times10^{-6}\,\Omega\cdot$m^2
Anode/cathode inlet pressure, P_{in}	2.0 atm
Cell temperature, T_{cell}	80°C

Table **4-3**: Simulation parameters

Description	Value
Exchange current density × Ratio of reaction surface to catalyst layer volume in anode side, $ai_{0,a}^{ref}$	1.0×10^{9} A/m^3
Exchange current density × Ratio of reaction surface to catalyst layer volume in cathode side, $ai_{0,c}^{ref}$	2.0×10^{4} A/m^3
Activation energy for oxygen reduction reaction in cathode side, E_a	73269 J/mol
Reference hydrogen molar concentration, $c_{H_2,ref}$	40.88 mol/m^3
Reference oxygen molar concentration, $c_{O_2,ref}$	40.88 mol/m^3
Anodic and cathodic transfer coefficients for hydrogen oxidation reaction (HOR)	$\alpha_a = \alpha_c = 1$
Cathodic transfer coefficient for oxygen reduction reaction (ORR)	$\alpha_c = 1$
Dry membrane density, ρ^{mem}	2000 kg/m^3
Equivalent weight of electrolyte in membrane, EW	1.1 kg/mol
Faraday Constant, F	96487 C/mol
Universal Gas Constant, R_u	8.314 J/mol K
Surface tension, σ	0.0625 N/m
Liquid water density, ρ_l (80^{o}C)	972 kg/ m^3
Liquid water viscosity, μ_l	3.5×10^{-4} N·s/ m^2
Effective electronic conductivity in catalyst layers, σ_{CL}	1000 S/m
Effective electronic conductivity in GDL, σ_{GDL}	10000 S/m
Electronic conductivity in current collector, σ_{land}	20000 S/m
Catalyst coverage coefficient, n_c	2.0
Diffusivity correction factor, n	2.3

Figures

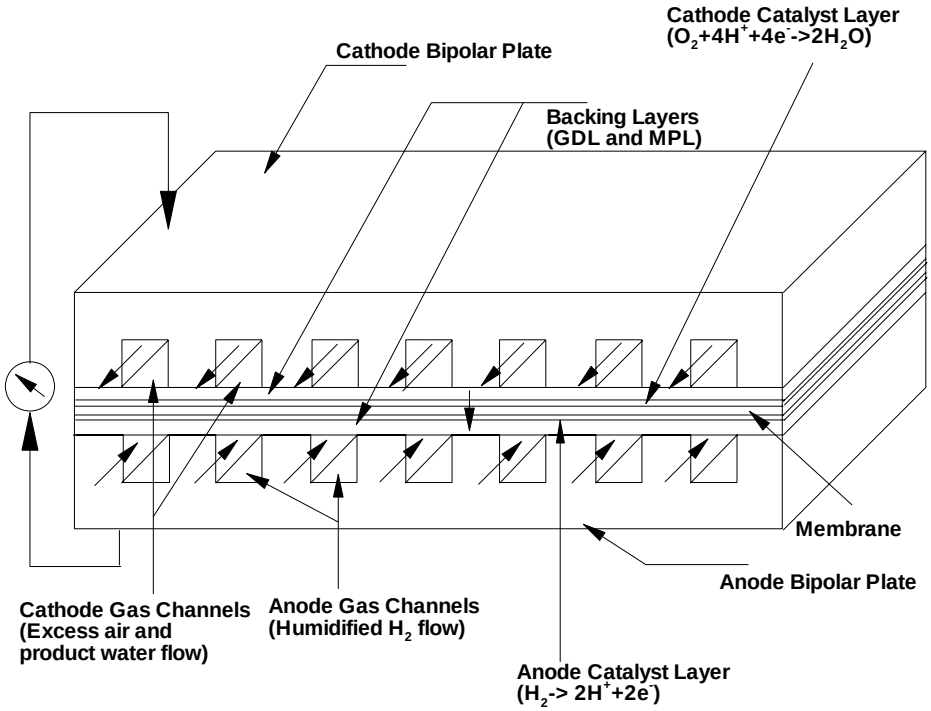

Figure **4-1**: Schematic of a multi-channel counter-flow PEFC.

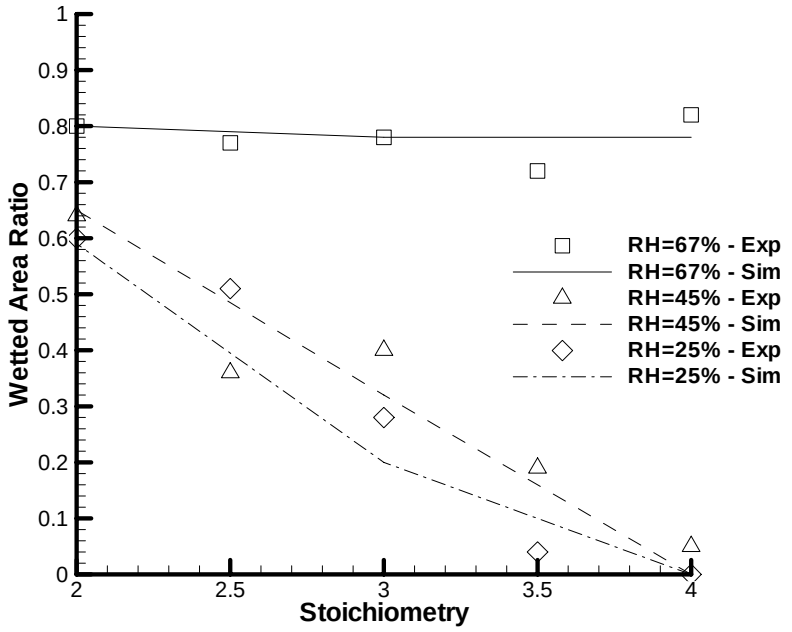

Figure **4-2**: Wetted area ratio versus air stoichiometry for I_{avg}=0.2A/cm^2.

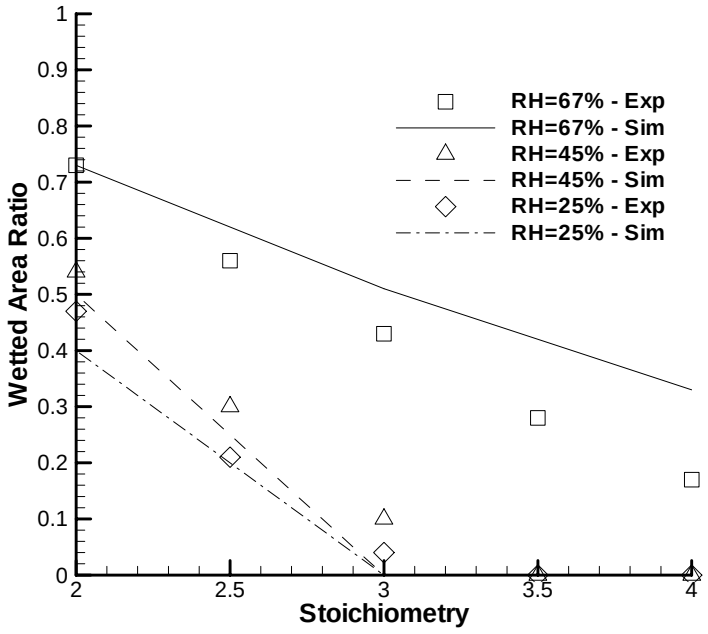

Figure **4-3**: Wetted area ratio versus air stoichiometry for I_{avg}=0.5A/cm^2.

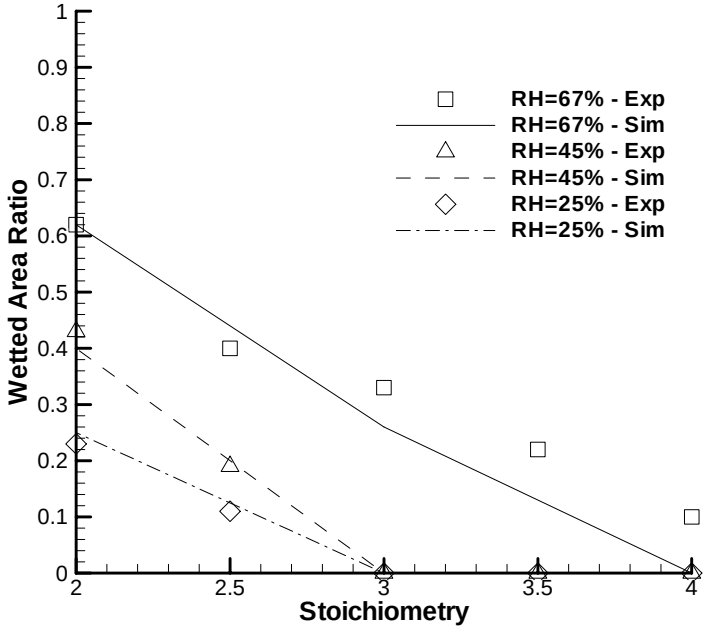

Figure **4-4**: Wetted area ratio versus air stoichiometry for I_{avg}=0.8A/cm^2.

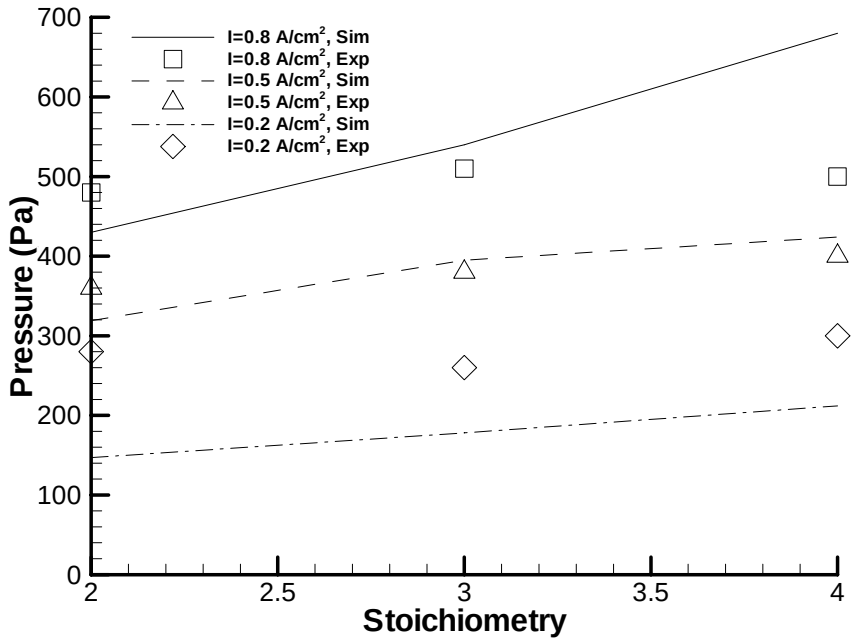

Figure **4-5**: Pressure drop validation with 33% GDL intrusion.

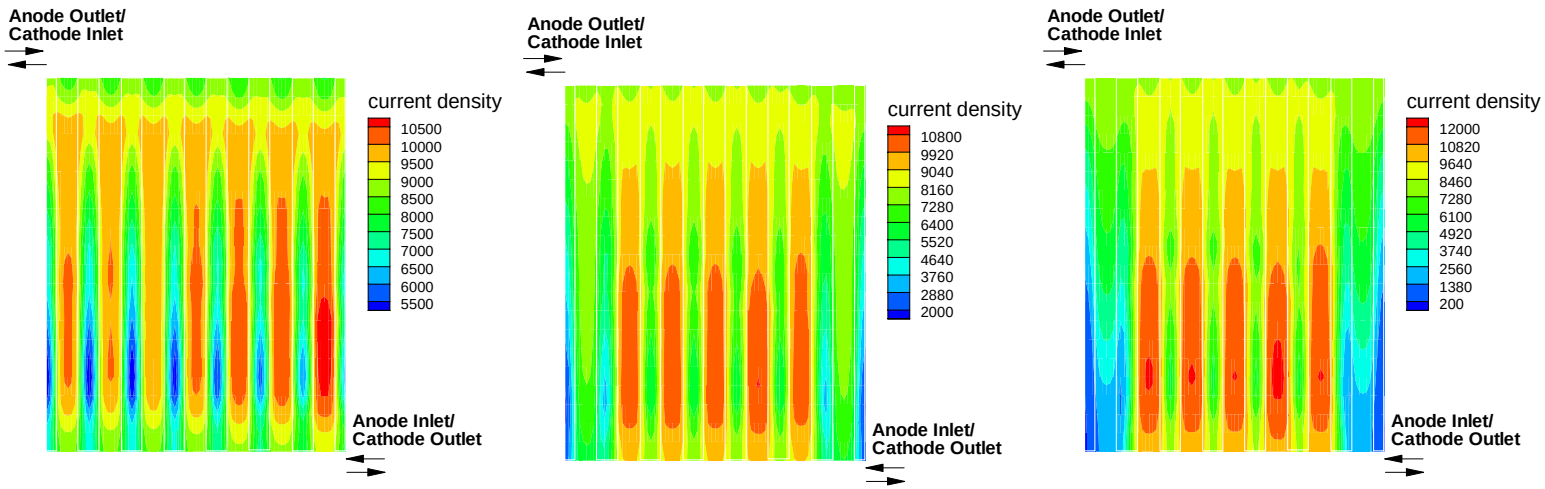

(a) no-intrusion. (b) 17% GDL intrusion. (c) 33% GDL intrusion.

Figure **4-6**: Current density (A/m^2) contours in the membrane.

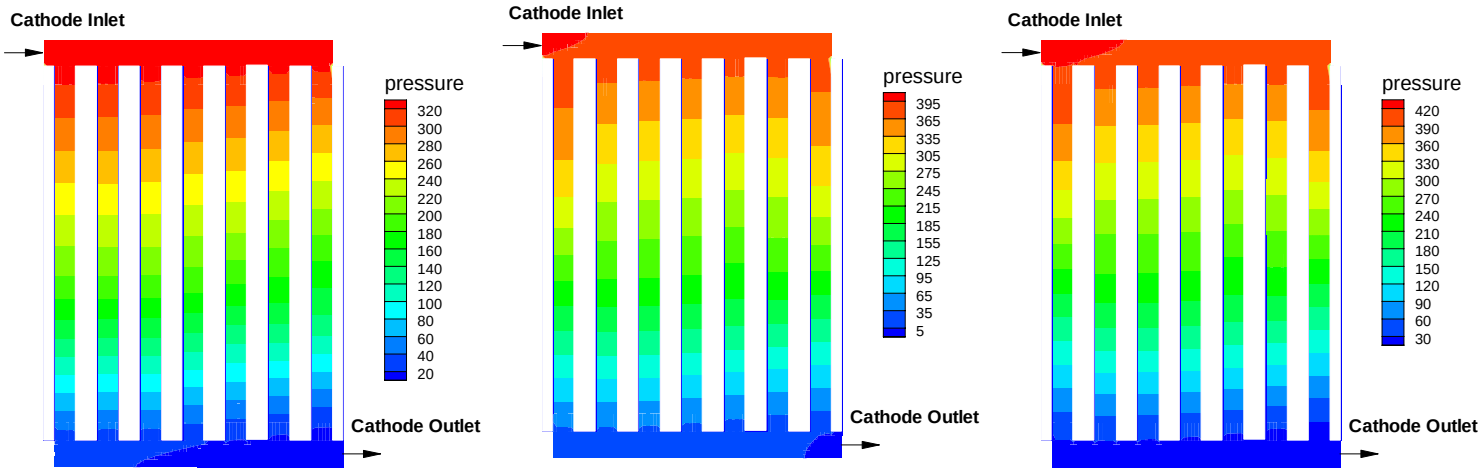

(a) no-intrusion. (b) 17%-intrusion. (c) 33%-intrusion.

Figure **4-7**: Pressure (Pa) contours at the mid-height of cathode channels.

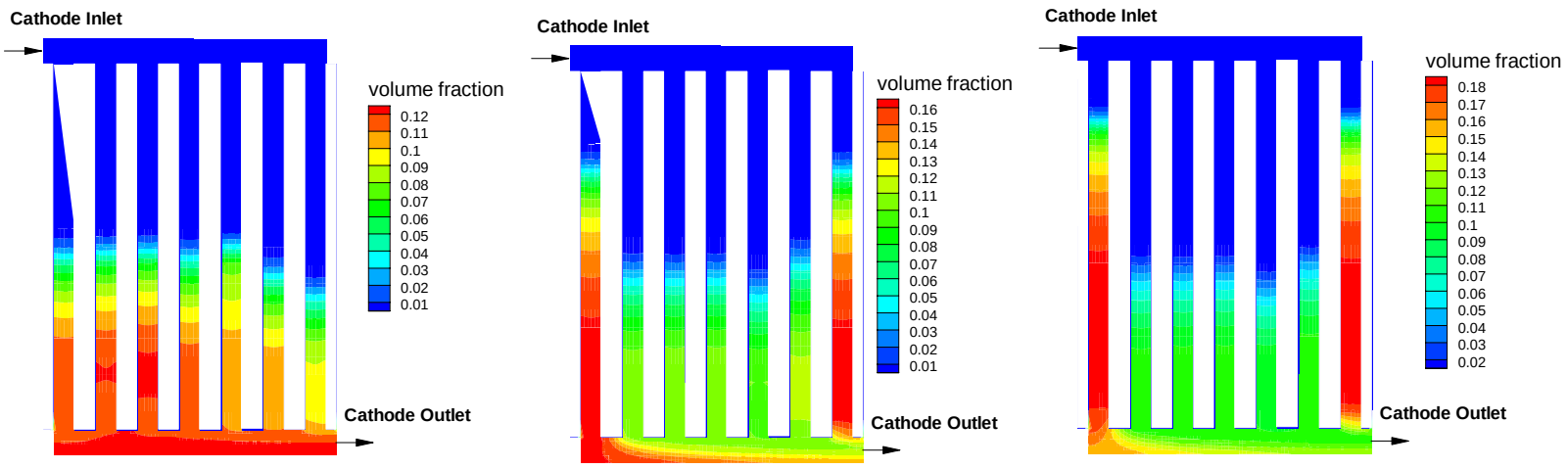

(a) no-intrusion. (b) 17%-intrusion. (c) 33%-intrusion.

Figure **4-8**: Liquid water volume fraction contours at the mid-height of cathode channels.

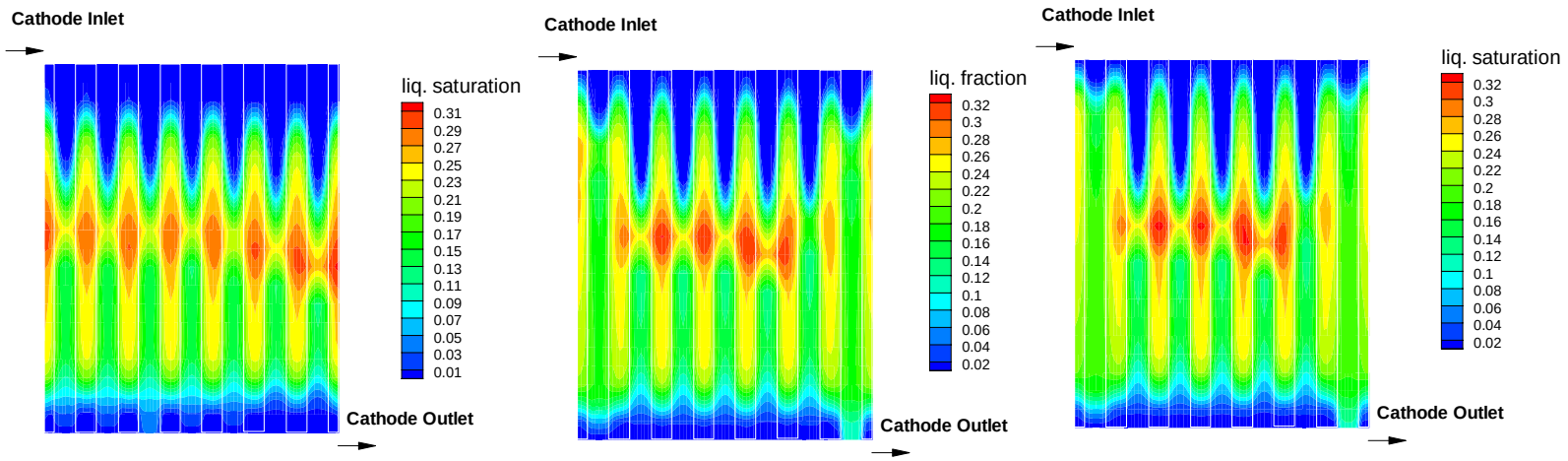

(a) no-intrusion. (b) 17% intrusion. (c) 33% intrusion.

Figure **4-9**: Liquid water saturation contours at the midsection of the cathode GDL.

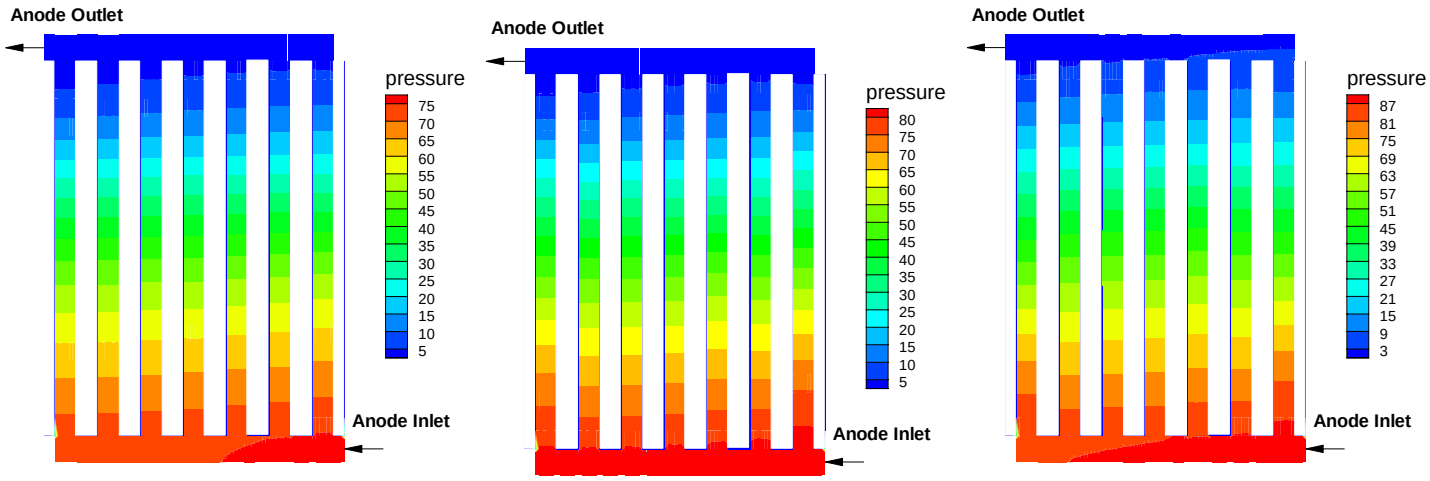

(a) no-intrusion. (b) 17%-intrusion. (c) 33%-intrusion.

Figure **4-10**: Pressure (Pa) contour at the section of anode channels.

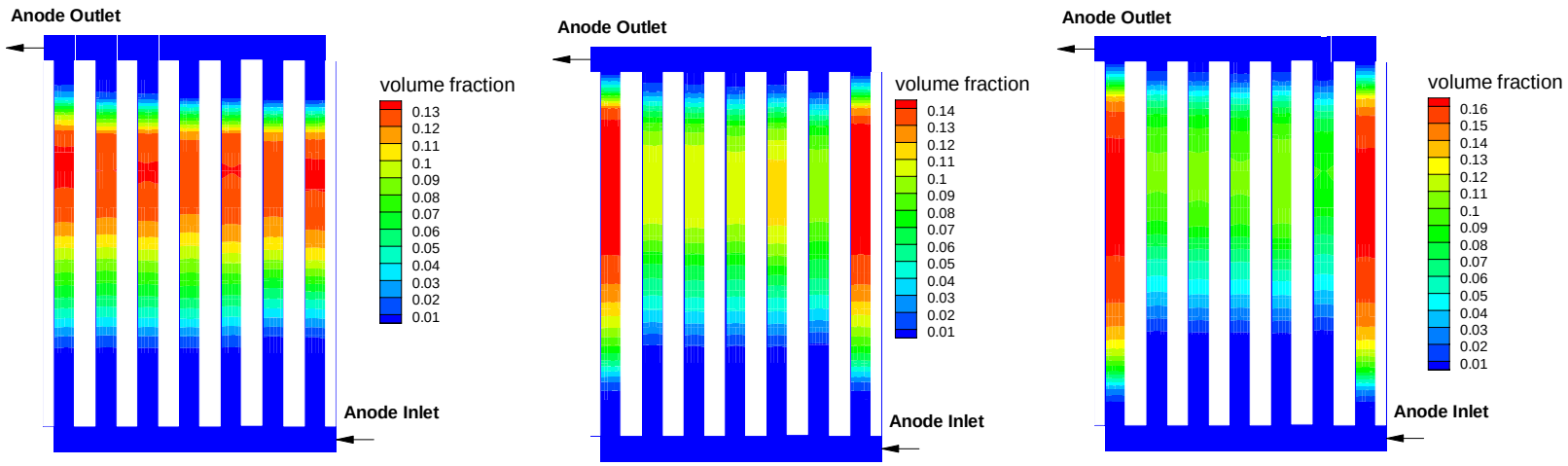

(a) no-intrusion. (b) 17%-intrusion. (c) 33%-intrusion.

Figure **4-11**: Liquid water volume fraction at the section of anode channels.

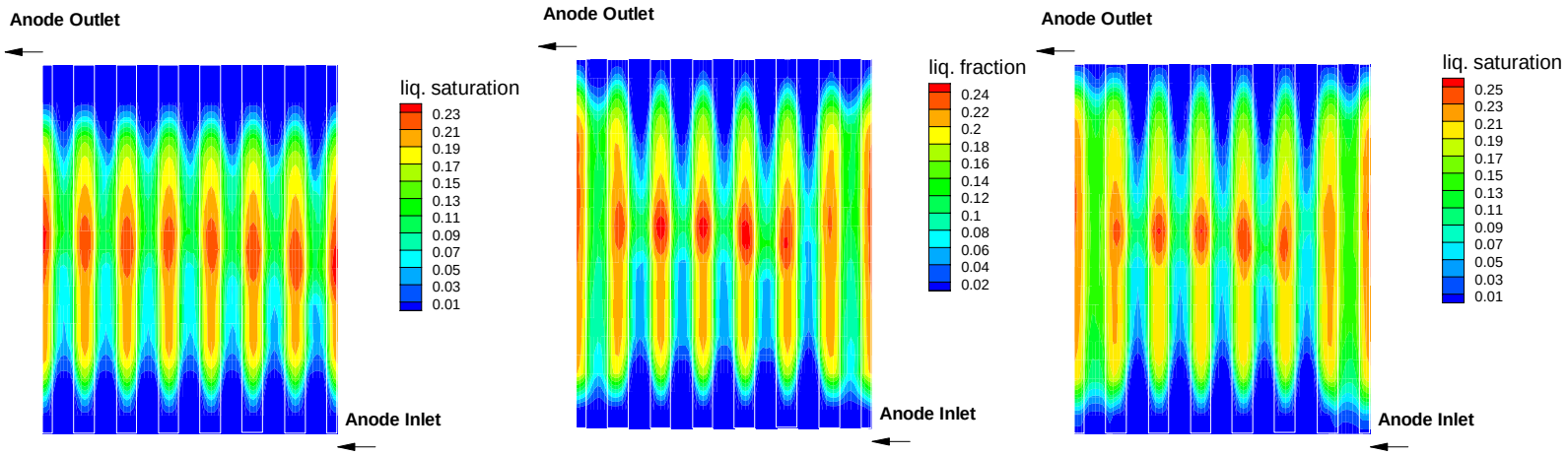

(a) no-intrusion. (b) 17% intrusion. (c) 33% intrusion.

Figure **4-12**: Liquid water saturation contours at the midsection of the anode GDL.

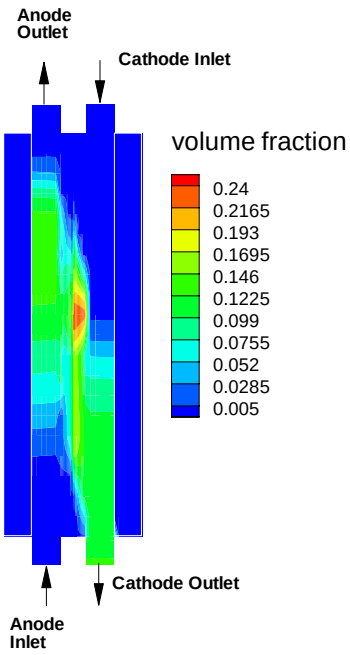

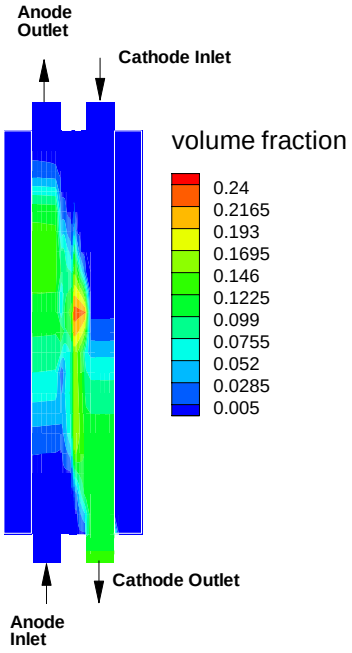

Edge channel Middle Channel

(a) no-intrusion.

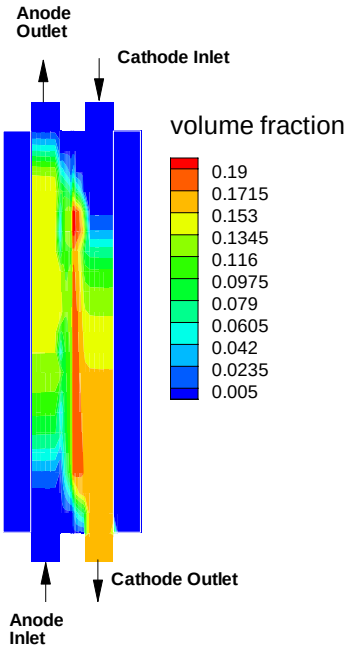

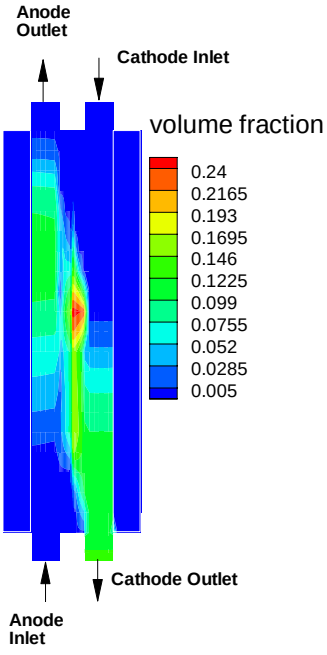

Edge channel Middle Channel

(b) 17%-intrusion.

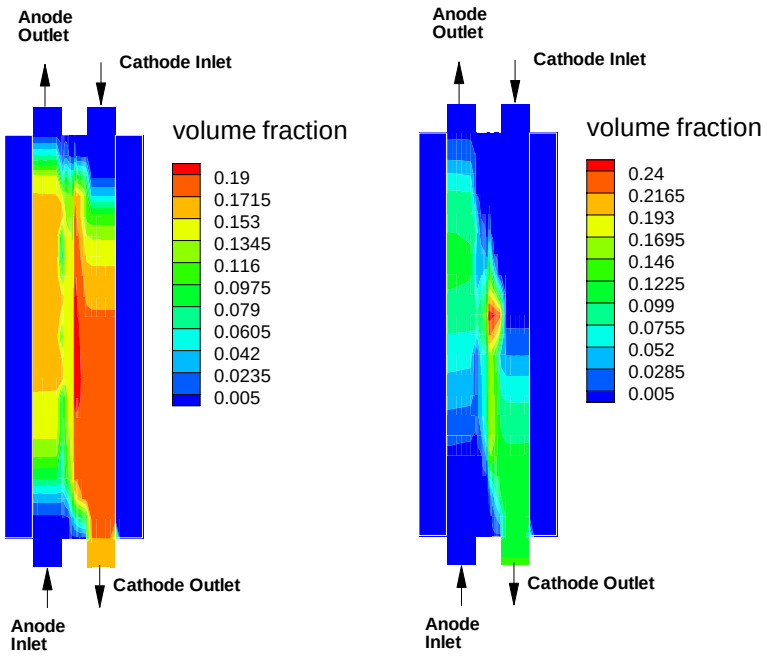

Edge channel Middle Channel

(c) 33%-intrusion.

Figure **4-13**: Liquid volume fraction contours across edge and middle channels.

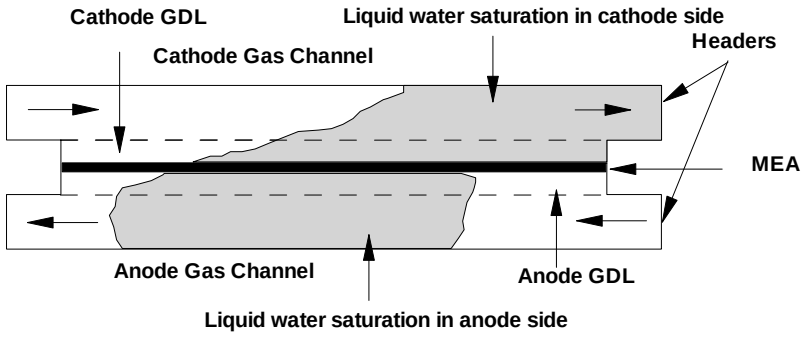

(a) middle channel

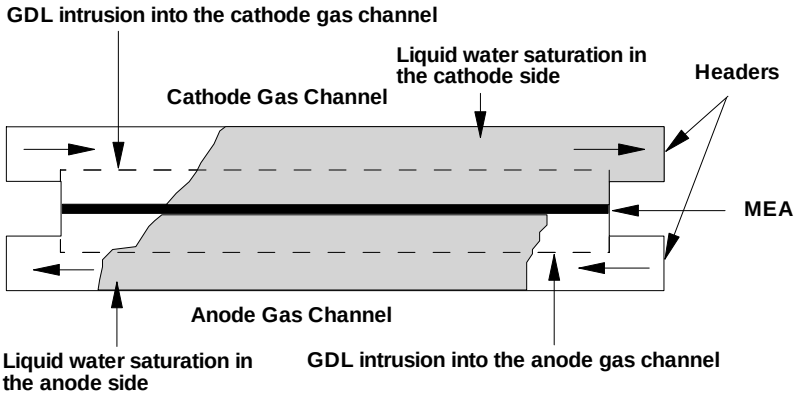

(b) edge channel with GDL intrusion

Figure **4-14**: Schematic of liquid water distribution in a PEFC.

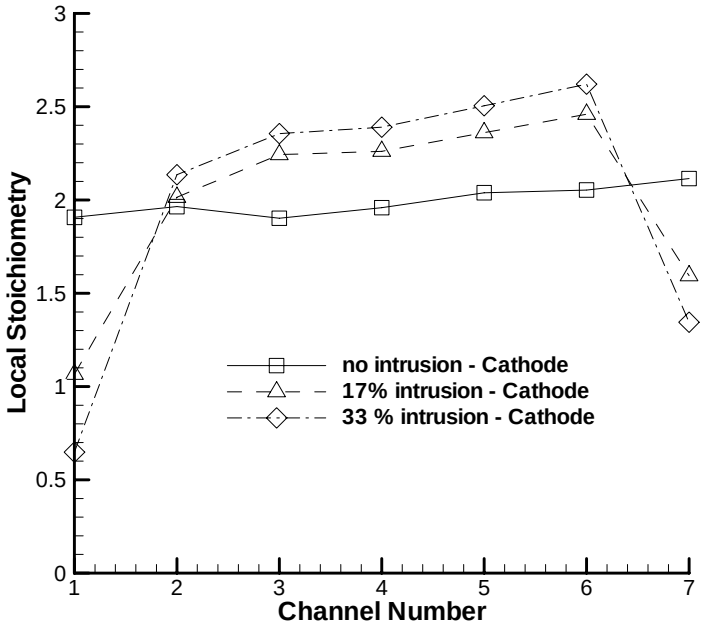

(a) cathode channels

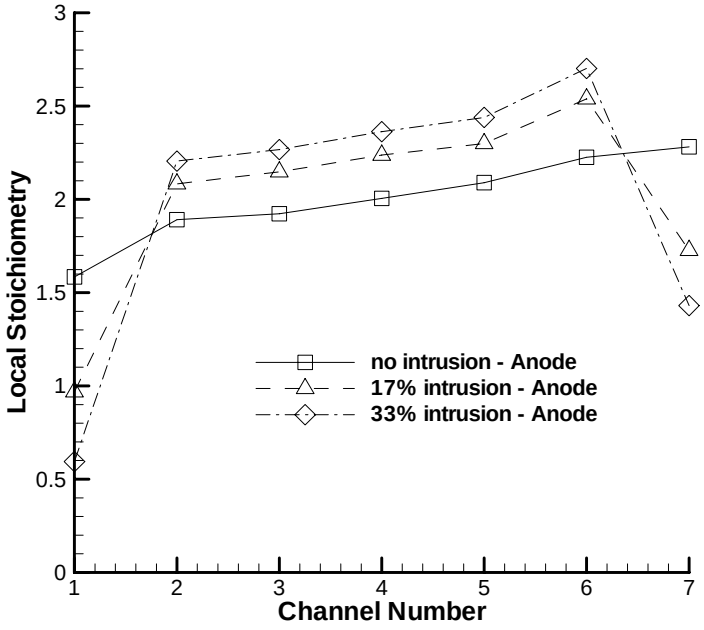

(b) anode channels

Figure **4-15**: Plots of local flow stoichiometry in different channels on the cathode and anode.

Chapter 5

Phase Change in a Polymer Electrolyte Fuel Cell

Introduction

High and stable polymer electrolyte fuel cell (PEFC) performance requires efficient removal of product water and heat from the reaction sites. The most important coupling between water and heat transport in PEFC is arguably the liquid-vapor phase change. The phase change phenomena, or evaporation/condensation, have not been directly explored. In this chapter we intend to shed light on physical characteristics of liquid-vapor phase change and their implications in PEM fuel cell operation. In the present work, a two-phase, non-isothermal numerical model is developed and used to elucidate the phase-change rate inside the cathode GDL of a PEFC.

Numerical Model

In the present work, we formulate a steady-state, non-isothermal, two-phase model following Wang and Wang.[31], in order to capture the phase-change rate in the cathode GDL of a PEFC. Conservation equations of mixture- mass, momentum, energy, species and potential equations are solved in our model and have been discussed in the previous chapter. Details about these equations and the source terms are available in the published literature[31, 69] and also listed in Table 4.1. The details of this model have been discussed in the previous chapter.

Once the liquid saturation value is known, we reconstruct the liquid velocity using Equation (14). In the M^2 (multiphase mixture) model, the mixture velocity is computed only. The individual phase velocities are reconstructed as follows[41]:

$$\rho_l u_l = j_l(s) + \lambda_l(s)\rho u \tag{5.1}$$

Since constant gas density has been shown by Wang and Wang [74] to yield about 10% inaccuracy under normal PEFC conditions, density and viscosity of liquid phase is taken to be constant in the present work.

The mass conservation equation at steady state could be written for liquid and gas phase as the follows [41]:

$$\nabla.(\rho_l u_l) = \dot{m}_l \tag{5.2}$$

$$\nabla.(\rho_g u_g) = \dot{m}_g \tag{5.3}$$

Here $\dot{m}_l$ and $\dot{m}_g$ are the interfacial mass transfer rates from liquid and gas phases respectively. In the absence of any external mass source or sink, the sum of these interfacial mass transfer rates over all the phases is zero. So, for the two-phase mixture,

$$\dot{m}_l + \dot{m}_g = 0 \tag{5.4}$$

Hence using Eq. **5.2** and Eq. **5.3** on Eq. **5.4** the mixture mass conservation equation could be reached. In the M^2 framework interfacial mass transfer from one phase to the other (in the form of evaporation or condensation) is computed from the divergence of the phase velocity. Change of phase is associated with release or absorption of latent heat. That effect included in the source term for energy equation.

For simplicity and to highlight phase change in GDL, mist flow is assumed in gas channels. Water is produced in the cathode catalyst layer (CCL) and it condenses there. Water in both liquid and vapor phase is transported to the cathode GDL. Because the temperature is lower in the GDL with respect to the CL, condensation is expected in the GDL close to the CCL. Condensation is also expected over the cooler land surface. Evaporation takes place in the GDL under the channel. For partially humidified flow in the cathode gas channel, the flow transports water in both liquid and vapor forms, while for fully humidified flow in the gas channels liquid water is transported into the channel by gas shearing.

Results and Discussion

Base Case

In the present study stoichiometry is fixed at 2.0 for both the anode and the cathode whereas the cell temperature is fixed at 80^{o}C and average current density at 1.0A/cm^{2}. The cell geometry and the simulation parameters are listed in **Table 5-1** and **Table 5-2** . A mesh consisting of 22,344 computational elements was used to compute the case study results, and the mesh sensitivity test has been performed and documented elsewhere [75]. In the simulations to be presented below, all species imbalances are less than 1% and residuals smaller than 10^{-5}. Fully humidified case is considered as the Base Case. Total heat generation in the cell is constant as the cell operating current density and operating temperature are fixed. Therefore, at steady state, total heat transfer from the cell is constant. Phase change in a cell depends on the local temperature gradient and

water concentration gradient. At constant heat transfer condition the temperature gradient is expected to be controlled by GDL thermal conductivity. Since the water production in the cell is constant, the water concentration gradient is controlled by the inlet relative humidity. To investigate the phase change in the cathode side of a PEFC – we consider the GDL thermal conductivity and inlet relative humidity as the two most important parameters controlling the phase-change rate.

The PEFC geometry used for case studies in the present work is shown in Figure **5-1**. Temperature, saturation and phase-change rate contours are plotted in the cross section (named Section A) of the PEFC in the through-plane direction, midway between the inlet and the outlet. Our cell operates in counter-flow configuration. Thus, near the cathode inlet electro-osmotic drag (EOD) dominates the back flow of water (from cathode side to the anode side). Along the cathode flow direction as liquid water saturation increases back flow of water becomes stronger and near the outlet it dominates over EOD resulting in dry-wet-dry flow channel [73]. These two opposing mechanisms of water transport are found to balance each other near the middle when cathode and anode have same level of inlet humidification [76]. Therefore midway between inlet and exit almost all the product water is removed through the cathode channel. Since the current density is kept constant, total water transport from cathode GDL to cathode channel is almost constant at Section A for all the cases.

Temperature and liquid saturation contours at Section A are plotted for the Base Case in Figure **5-2a**, whereas Figure **5-2b** illustrates the phase change rate contour in the cathode side.

Parametric study

i) Effect of inlet relative humidity

As our Base Case is the fully humidified condition the inlet relative humidity is decreased gradually to investigate the RH effect on phase change. Computations were carried out for inlet relative humidities of 67% (T_{inlet}=70^{o}C), 45% (T_{inlet}=60^{o}C) and 25% (T_{inlet}=50^{o}C) with other parameters being the same as those in the Base Case. At lower relative humidity, liquid saturation in the cell is lower.

Temperature and saturation contours at Section A for RH=67% are plotted in Figure **5-3**a. The temperature range in this case is the same as that in the Base Case. The range of liquid saturation does not show any difference from that in the Base Case. The difference from the Base Case is not apparent in the phase-change rate contours for the RH=67% case at Section A (see Figure **5-3**b). At Section A gas flow through the cathode channel is fully saturated for RH=67%. Therefore the contours look very similar to those in the fully humidified Base Case.

The difference becomes clearer in the case with RH=45%. Contours of temperature and saturation at Section A for RH=45% case are plotted in Figure **5-4**a. The temperature rise in the cell is about 0.5^{o}C lower in this case with respect to the Base Case. Liquid saturation contours at Section A for this case shows that the GDL over channel is almost dry at this length. But the maximum liquid saturation (which occurs over land) decreases only slightly. This indicates that the liquid shearing at the GDL-channel interface should be low since part of the GDL is almost dry. The phase-change rate contour at Section A (plotted in Figure **5-4**b) exhibits this trend. Due to low humidity

of the gas flow the catalyst layer is almost dry under the middle of the channel. Consequently, very little condensation takes place here.

As the inlet RH is further reduced to 25%, liquid saturation reduces significantly at Section A (shown in Figure **5-5**a) but the temperature distribution at this section remain about the same. MEA and GDL over the land are totally dry under this condition. Hence the phase-change rate also decreases (shown in Figure **5-5**b). Under this very low inlet RH no phase change takes place in the CCL under channel as all the product water could be transported in vapor form by molecular diffusion. Temperature in the CCL is lower under the land and hence water condenses in CCL and GDL. Although heat pipe effect is weakened by lower temperature gradient (also for the case of inlet RH= 45%), water still condenses on the cooler land surface. This liquid evaporates in the GDL near the wet-dry interface.

From the contours of phase change rate it is clear that condensation takes place chiefly in two locations in the cathode side – in the CCL and GDL adjacent to it (due to water production) and on the land surface (due to cooler temperature). Variation of phase-change rate and liquid saturation over the land is of special interest because this is a measure of the heat pipe effect in the cell. Liquid saturation and phase-change rate under the middle of the land adjacent to it is plotted along the channel for the four cases (RH=100%, RH=67%, RH= 45% and RH=25%) in Figure **5-6**. The positive values in Figure **5-6**b indicate condensation. Since GDL adjacent to the land is cooler, water can only condense here. Therefore, Figure **5-6b** indicates either condensation or no phase change at this location for all the cases. Fully humidified case shows high and almost uniform phase-change rate along the channel. For RH= 67%, phase-change rate under the

land decreases near the inlet and the exit. For RH=45% the GDL is dry near the inlet and outlet. Thus, condensation does not take place under land for some distance near inlet and outlet. At the mid-length of the channel the maximum vapor condensation over the land is smaller by 20% with respect to that in the Base Case due to smaller temperature difference from cathode CL to cathode bipolar plate.

Liquid saturation and phase-change rate profiles in the in-plane direction yield important insight. For partially humidified inlet flow, both the variables change along the flow direction as shown in Figure **5-6**. Variations of condensation and liquid saturation on the land surface were investigated at different flow lengths. Three lines are chosen to show these variations, which can be observed close to the inlet (Y*=0.25), midway between inlet (Y*=0.5) and close to the outlet (Y*=0.75). Along these lines liquid saturation and phase-change rate profiles are plotted for RH=100%, RH=67%, RH= 45% and RH=25% (Figure **5-7** a, b, c, d respectively). Liquid saturation is high under the middle of the land and reduces gradually under the channel. Phase-change rate is high under the land as condensation takes place. Under the channel, phase change is almost invisible. In the fully humidified case, cathode GDL is totally wet. Liquid saturation and phase-change rate is almost uniform along the flow direction (Figure **5-6**). Therefore, in-plane profiles of these quantities at different flow length almost coincide over each other (shown in Figure **5-7**a). Even for the case of inlet RH=67%, cathode GDL becomes totally wet for $0.25 < Y^* < 0.75$ (Figure **5-6**). So the in-plane profiles of liquid saturation and phase-change rate are almost identical (Figure **5-7**b). As the inlet RH is decreased to 45% fraction of cathode GDL near inlet and exit remain dry. No condensation takes place over the land in these portions (Figure **5-6**). When the inlet RH is further reduced (45%)

the cell becomes drier. Cathode side is not fully wet at Section A. Condensation on the land surface starts at 20% of the flow length away from the inlet (Figure **5-6**b). This phase change increases rapidly reaching maxima at the middle of the flow length and reduces rapidly after that and dries out about 80% of the flow length from inlet. The in-plane profiles (shown in Figure **5-7**c) show this clearly. In the sections close to inlet and exit liquid saturation is less and condensation takes place only under the center of the land. As the inlet RH is reduced even further (25%), cell runs in even more dry condition. Condensation on the cathode land surface occurs at the middle (Figure **5-6**b) while under the channel the GDL is totally dry (Figure **5-5**b). Near the inlet and the exit, cathode GDL is almost dry, with trace amount of liquid on the land surface (shown in Figure **5-7**d).

Another interesting observation from Figure **5-7** is that there is a distinct peak in the phase-change rate profile under land for RH=100% and 67% cases. Cathode GDL is totally wet in these cases. Liquid saturation is maximum under the middle of the land in all the cases and minimum under the middle of the channel. Therefore resistance to the gas flow due to heat pipe effect toward the land is greater under the middle of the land (as greater portion of the pores are blocked by liquid). But the in-plane variation of temperature in the land is negligible. Therefore, the driving temperature difference for the heat pipe effect remains almost same while the resistance to flow path increases under the middle of the land. Therefore the maxima of the phase-change rate shifts toward the channel following the path of least resistance as shown in Figure **5-8**. For the lower inlet RH cases however, this peak is less pronounced (RH=45%) or even non existent

(RH=25%). In these cases liquid saturation is much lower and therefore maxima of phase-change rate occurs under the middle of the channel.

ii) Effect of GDL Thermal Conductivity

The other parameter which has a strong effect on phase change rate is the GDL thermal conductivity. In the base case the GDL thermal conductivity is 3W/mK. As the GDL thermal conductivity is reduced to 2W/mK cell temperature increases with little change in the liquid saturation profile (shown in Figure **5-9**a). Although production and transfer of heat in this case is same as in the base case, fractional increase in temperature is less than fractional reduction in thermal conductivity. The phase change rate contour (shown in Figure **5-9**b) shows much higher value of condensation on the cathode land surface. This indicates stronger heat pipe effect and decreased effective thermal conductivity.

The same trend is observed in Figure **5-10**a and b where the GDL thermal conductivity is decreased to 1W/mk. Condensation on cathode land increases substantially. This shows that even greater fraction of total heat transfer is through heat pipe effect.

Increase in condensation under cathode land is shown in Figure **5-11**b. The liquid saturation close to the cathode land along the flow direction does not change appreciably with decreasing GDL thermal conductivity (Figure **5-11**a). Since the inlet RH is 100% in these cases, conditions are almost identical in the flow direction. Therefore variation of both liquid saturation and phase-change rate is very little along the channel. The same

could be found from the in-plane profiles of liquid saturation and phase-change rate at different locations in flow direction (shown in Figure **5-12**).

At the GDL-Land interface heat flux is mostly normal to the interface. Hence energy conservation could be performed near the GDL-Land interface in one dimension. In presence of very small advection, conductive heat flux and heat generation due to condensation of water is balanced near the GDL-Land interface in through plane direction. Therefore considering these fluxes on an elemental volume at x (close to GDL-Land interface and x is the through plane direction) of dimension Δx we get,

$$k_{gdl}^{eff}\left.\frac{\partial T}{\partial x}\right|_{x}+h_{fg}M_{W}D_{g}^{eff}\left.\frac{\partial C_{W}^{sat}}{\partial x}\right|_{x}=k_{gdl}^{eff}\left.\frac{\partial T}{\partial x}\right|_{x+\Delta x}+h_{fg}M_{W}D_{g}^{eff}\left.\frac{\partial C_{W}^{sat}}{\partial x}\right|_{x+\Delta x} \qquad (\mathbf{5.5})$$

Applying Taylor series with $\Delta x\to 0$, constant liquid saturation (s), porosity (ε) and considering that $\frac{\partial C_{W}^{sat}}{\partial x}=\frac{\partial C_{W}^{sat}}{\partial T}\frac{\partial T}{\partial x}$, we can get,

$$\frac{\partial}{\partial x}\left[\left(k_{gdl}^{eff}+h_{fg}M_{W}D_{g}^{eff}\frac{\partial C_{W}^{sat}}{\partial T}\right)\frac{\partial T}{\partial x}\right]=0 \qquad (\mathbf{5.6})$$

From Eq. **5.6** it is clear that the heat pipe effect increases the total thermal conductivity of the GDL. Also we can define a thermal conductivity due to phase-change. Summation of effective GDL thermal conductivity and phase-change thermal conductivity would give total thermal conductivity,

$$k_{gdl}^{eff}+h_{fg}M_{W}D_{g}^{eff}\frac{\partial C_{W}^{sat}}{\partial T}=k_{gdl}^{eff}+k_{fg}=k_{gdl}^{total} \qquad (\mathbf{5.7})$$

As the GDL thermal conductivity is decreased fraction of total heat transferred through heat pipe increases. This increases the temperature gradient and ultimately the cell temperature rise. The effective diffusivity of water vapor decreases as the liquid

saturation increases [77]. The relation between effective diffusivity of water and liquid saturation is shown in Eq. **5.8**

$$D_W^{eff} = D_W (1-s)^{2.3} \varepsilon^{4.0} \quad (\mathbf{5.8})$$

Therefore as the liquid saturation increases the heat pipe effect weakens. Due to the same reason, for fully (or highly) saturated conditions heat pipe shift toward the channel (as was found in Figure **5-7**) although minimum temperature occurs under the middle of land.

Conclusions

A single-channel PEFC is computed using steady, non-isothermal, two-phase model to investigate the phase-change in the cathode GDL. Inlet relative humidity and thermal conductivity of cathode GDL is found to have strong influence on the phase-change rate. Inlet RH effect is felt along the channel as lower humidity results in dry length near inlet and outlet. For fully humidified condition maximum condensation takes place about midway between the middle of the land and channel-land interface. High resistance due to liquid saturation under the middle of the land results in this shift. For lower liquid saturation (here lower inlet RH) maximum condensation coincides with maximum liquid saturation on the middle of the land. GDL thermal conductivity does not change the shape of the profile of phase-change rate. Decrease of thermal conductivity results in greater temperature gradient in the cathode GDL. Therefore cell temperature increases. Since the heat transfer coefficient due to phase-change remains constant – total thermal conductivity of the GDL reduces at a lower rate. Hence phase-change heat

transfer coefficient becomes a larger fraction of the total heat transfer coefficient. As a result condensation under the land increases significantly at lower GDL thermal conductivity.

Tables

Table **5-1**: Cell geometry and properties**.**

Description	Value
Cell length	100.0 mm
Gas channel depth	0.5 mm
Gas channel width	1.0 mm
Land width	1.0 mm
Anode/cathode GDL thickness	0.20 mm
Anode/cathode catalyst layers thickness	0.010 mm
Porosity of anode/cathode GDL, ε_{GDL}	0.6
Porosity of anode/cathode catalyst layers, ε_{CL}	0.6
Volume fraction of ionomer in Anode/Cathode catalyst layers, ε_e	0.18
Hydraulic permeability of anode/cathode GDL, K_{GDL}	1.0×10^{-12} m^2
Hydraulic permeability of membrane, K_{mem}	5.0×10^{-20} m^2
Contact angle of anode/cathode GDL and catalyst layers, θ	92^o, 92°
Anode/cathode inlet pressure, P_{in}	2.0 Atm
Cell temperature, T_{cell}	80°C

Table **5-2**: Simulation parameters

Description	Value
Exchange current density × Ratio of reaction surface to catalyst layer volume in anode side, $ai_{0,a}^{ref}$	1.0×10^{9} A/m^3
Exchange current density × Ratio of reaction surface to catalyst layer volume in cathode side, $ai_{0,c}^{ref}$	2.0×10^{4} A/m^3
Activation energy for oxygen reduction reaction in cathode side, E_a	73269 J/mol
Reference hydrogen molar concentration, $c_{H_2,ref}$	40.88 mol/m^3
Reference oxygen molar concentration, $c_{O_2,ref}$	40.88 mol/m^3
Anodic and cathodic transfer coefficients for hydrogen oxidation reaction (HOR)	$\alpha_a = \alpha_c = 1$
Cathodic transfer coefficient for oxygen reduction reaction (ORR)	$\alpha_c = 1$
Dry membrane density, ρ^{mem}	2000 kg/m^3
Equivalent weight of electrolyte in membrane, EW	1.1 kg/mol
Faraday Constant, F	96487 C/mol
Universal Gas Constant, R_u	8.314 J/mol K
Surface tension, σ	0.0625 N/m
Liquid water density, ρ_l (80^{o}C)	972 kg/ m^3
Liquid water viscosity, μ_l	3.5×10^{-4} N·s/ m^2
Effective electronic conductivity in catalyst layers, σ_{CL}	1000 S/m
Effective electronic conductivity in GDL, σ_{GDL}	10000 S/m
Electronic conductivity in current collector, σ_{land}	20000 S/m
Catalyst coverage coefficient, n_c	1.0
Diffusivity correction factor, n	2.3

Figures

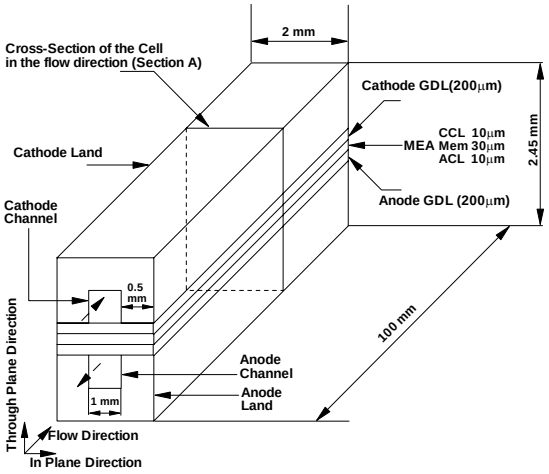

Figure **5-1**: Schematic of the computational cell showing the sections.

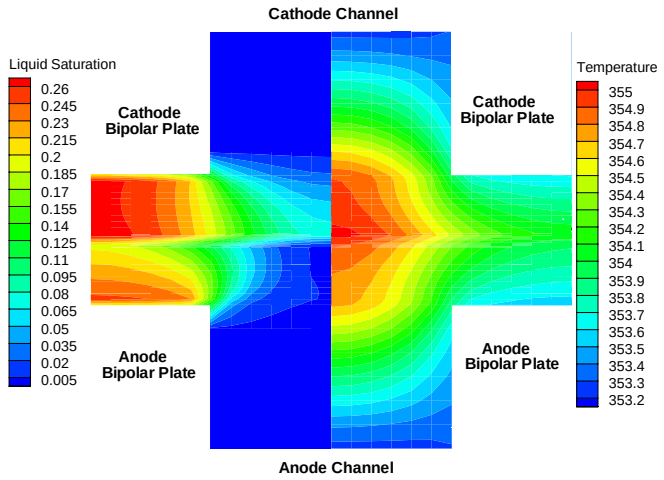

a: Liquid saturation and Temperature contours.

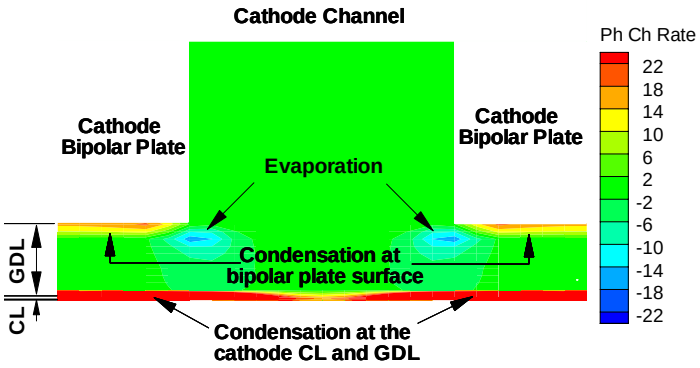

b: Phase change rate (kg/m^3s) contours in the cathode side.

Figure **5-2**: Base Case ($I=1.0A/cm^2$, Stoichiometry (A/C) =2.0, RH=100%) at Section B.

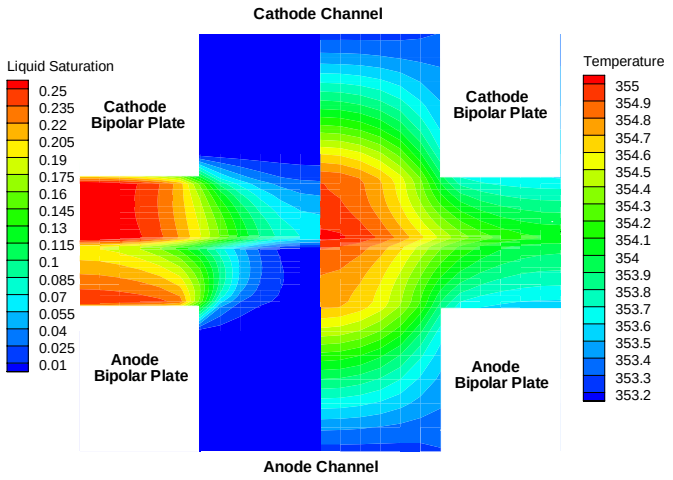

a: Liquid saturation and Temperature contours.

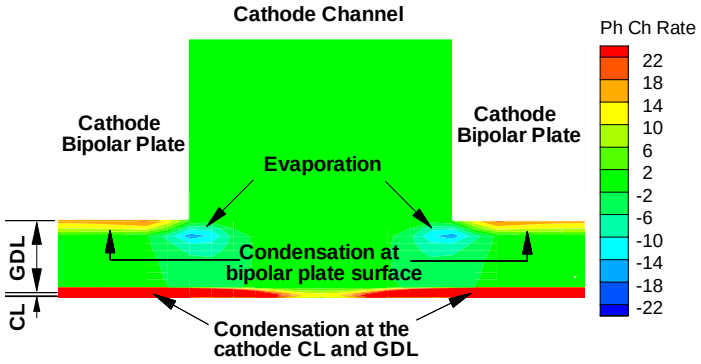

b: Phase change rate (kg/m^{3}s) contours in the cathode side.

Figure **5-3**: I=1.0A/cm^2, Stoichiometry (A/C) =2.0, RH=67% at Section B.

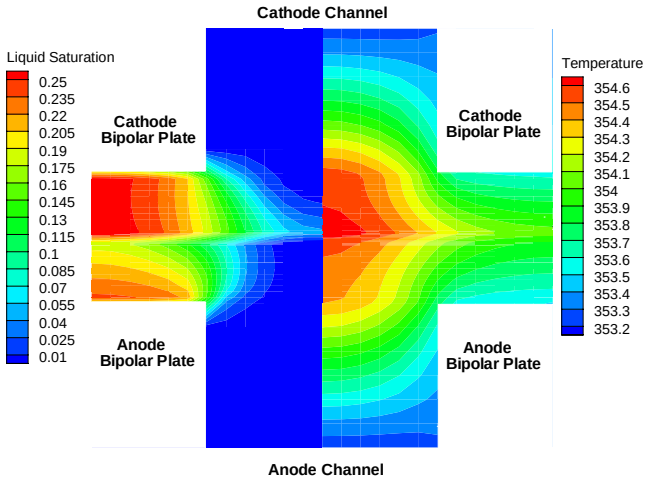

a: Liquid saturation and Temperature contours.

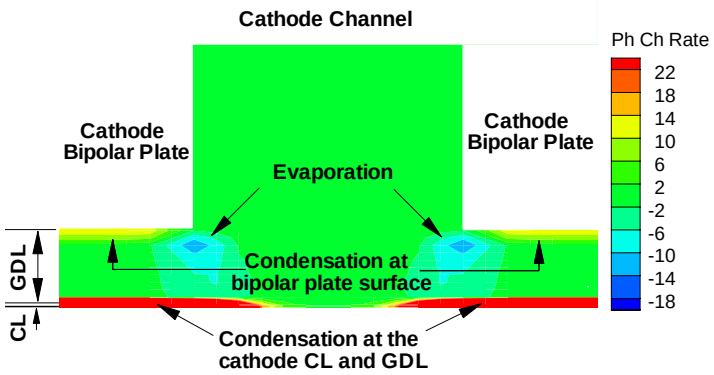

b: Phase change rate (kg/m^3s) contours in the cathode side.

Figure **5-4**: I=1.0A/cm^2, Stoichiometry (A/C) =2.0, RH=45% at Section B.

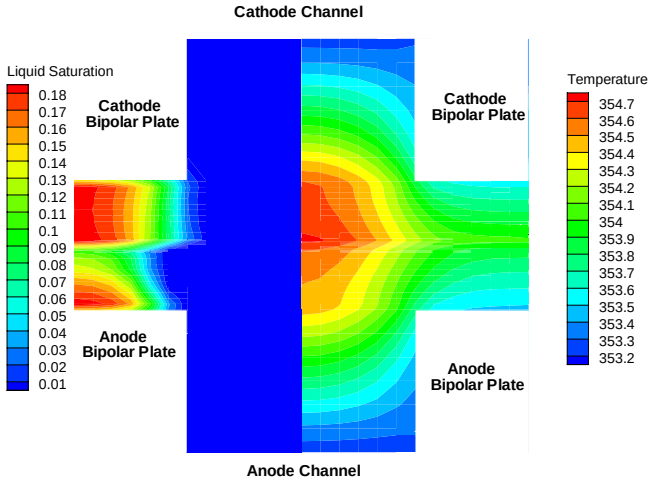

a: Liquid saturation and Temperature contours.

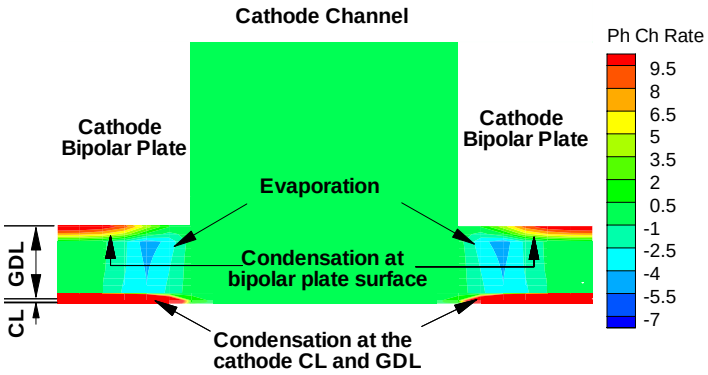

b: Phase change rate (kg/m^3s) contours in the cathode side.

Figure **5-5**: I=1.0A/cm^2, Stoichiometry (A/C) =2.0, RH=25% at Section B.

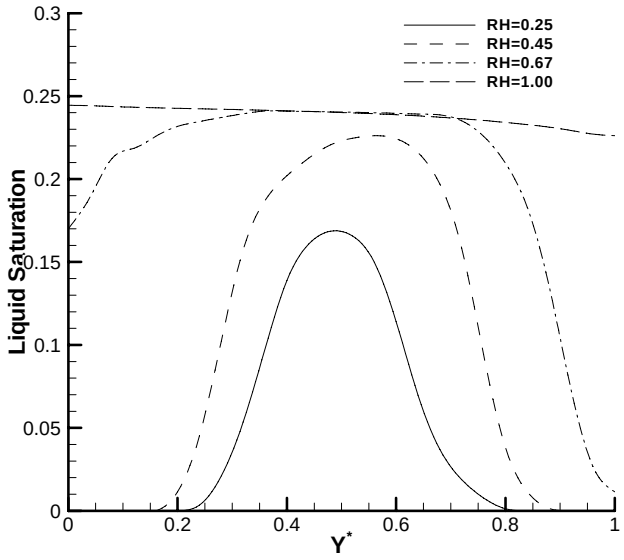

a: Liquid saturation

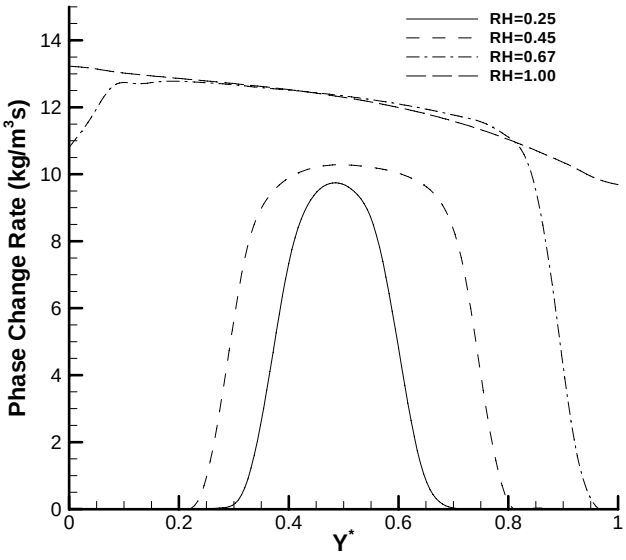

b: Phase Change Rate (Kg/m^3 s)

Figure **5-6**: Effect of Relatime Humidiy variation under the middle of the land along the channel.

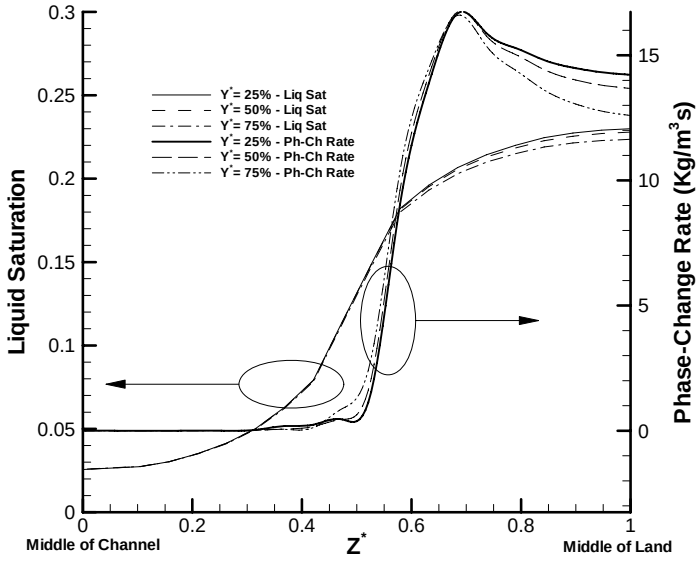

Figure **5-7a**: RH=100%.

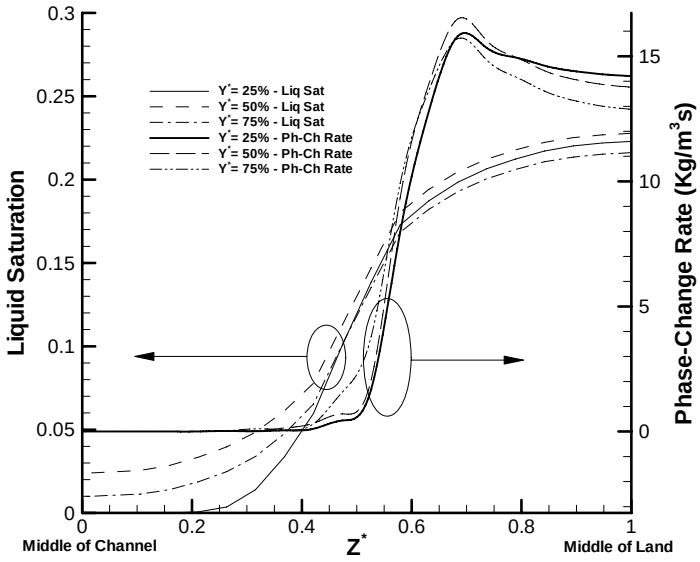

Figure **5-7b**: RH=67%.

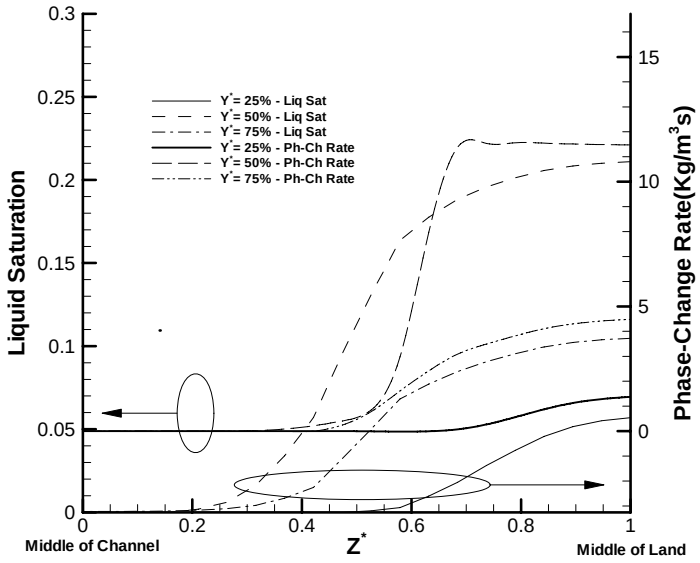

Figure **5-7c**: RH=45%.

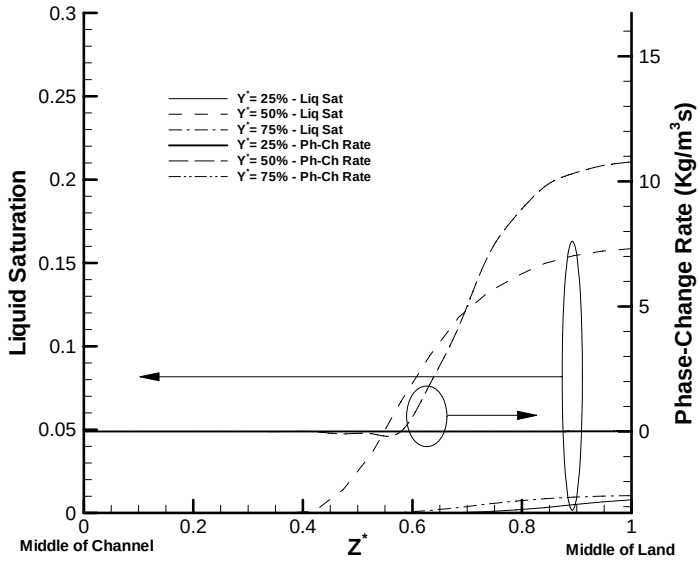

Figure 5-7d: RH=25%.

Figure **5-7**: Liquid Saturation and Ph-Ch Rate in the GDL near land and channel at different along-channel location (I=1.0A/cm^2, Stoichiometry (A/C) =2.0).

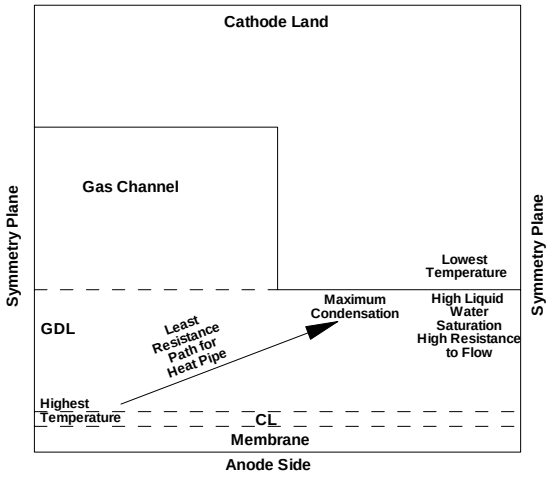

Figure **5-8:** Least resistance path for Heat Pipe.

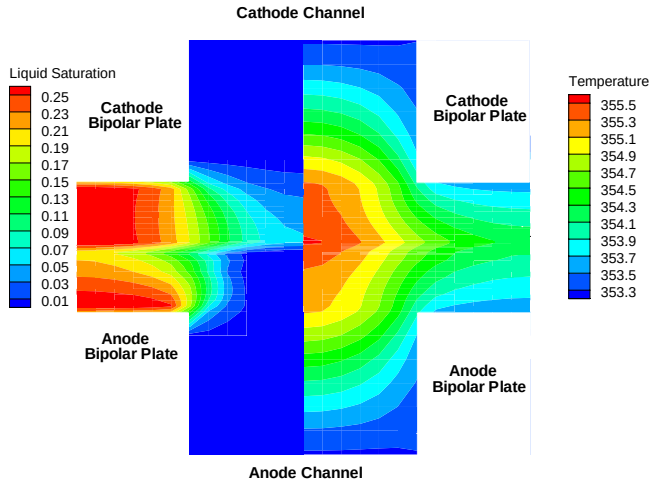

a: Liquid saturation and Temperature contours.

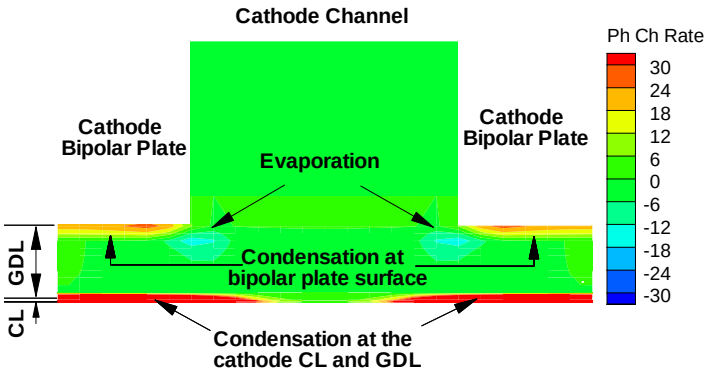

b: Phase change rate (kg/m^3s) contours in the cathode side.

Figure **5-9**: I=1.0A/cm^2, Stoichiometry (A/C) =2.0, RH=100% and K_{gdl}= 2.0 W/mK at Section B.

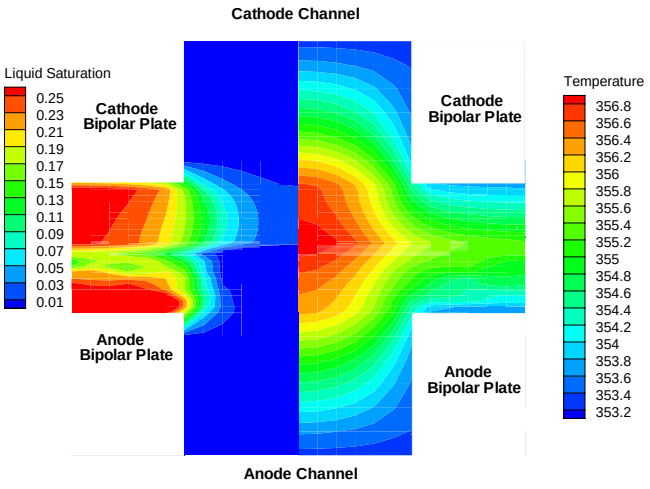

a: Liquid saturation and Temperature contours.

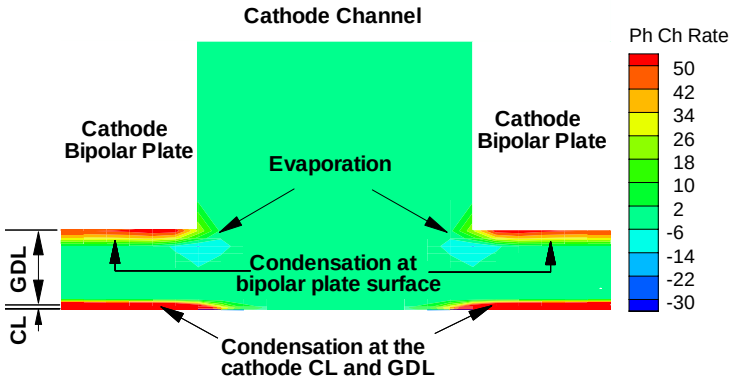

b: Phase change rate (kg/m^{3}s) contours in the cathode side.

Figure **5-10**: I=1.0A/cm^2, Stoichiometry (A/C) =2.0, RH=100% and K_{gdl}= 1.0 W/mK at Section B.

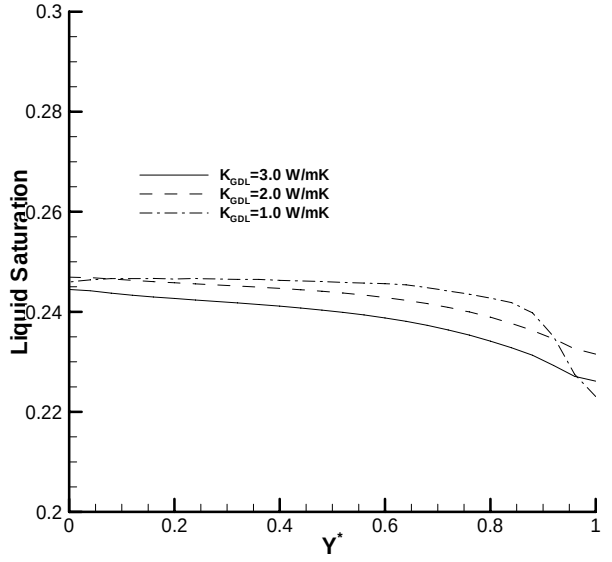

a: Liquid saturation

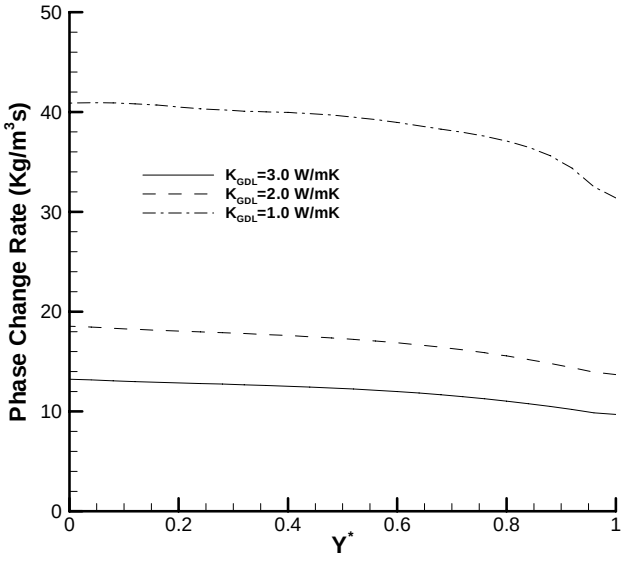

b: Phase Change Rate

Figure **5-11**: Effect of GDL thermal conductivity variation under the middle of the land along the channel.

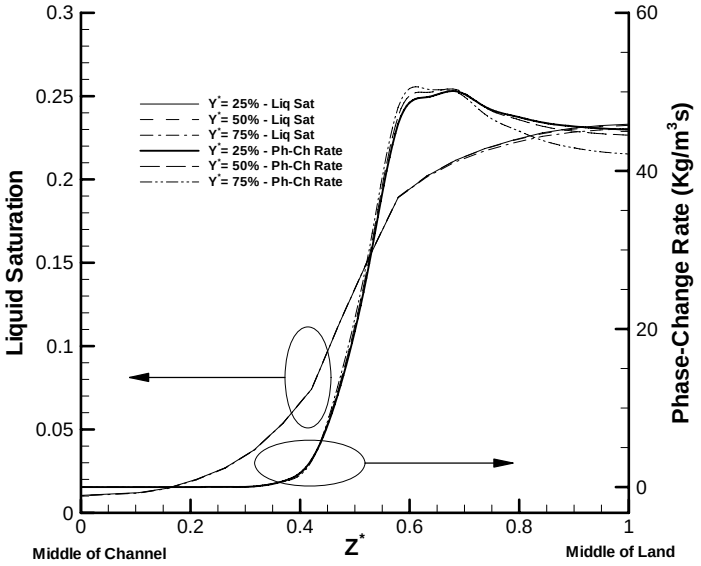

a: K_{gdl}= 1.0 W/mK.

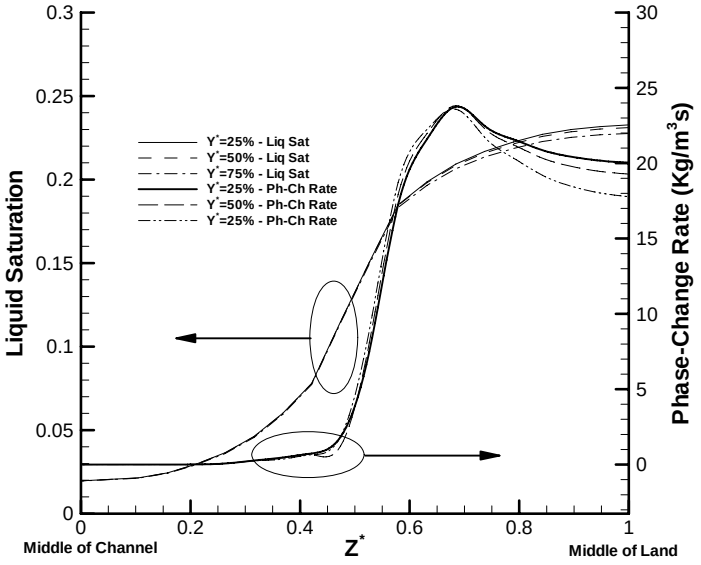

b: K_{gdl}= 2.0 W/mK.

Figure **5-12**: Liquid Saturation and Ph-Ch Rate in the GDL near land and channel at different along-channel location (I=1.0A/cm^2, Stoichiometry (A/C) =2.0, RH=100%).

Chapter 6

Conclusion and Future Work

Two-phase flow and maldistribution in the gas channels of a PEFC is modeled using a novel approach where the gas channels are considered as structured porous media. Since the flow is predominantly along the flow direction of the channel, first an analytical model is developed to model the flow maldistribution among a system of two parallel cathode gas-channels with GDL intrusion in one channel. A relation could be obtained between the flow maldistribution and GDL intrusion. It was found the different in dry lengths between channels is the most important factor in flow maldistribution among parallel channels. Therefore decreasing the relative humidity or increasing the stoichiometry of inlet may or may not result in lessening flow maldistribution depending on whether or not the difference in dry length is decreased.

The analytical model could handle only simple geometries and the common headers of gas channels were omitted here. Experiments have shown that the exit header of the cathode channels are highly wet and therefore has significant effect on flow maldistribution. A two-dimensional numerical model is developed for the cathode gas-channels. In this model only flow and water species equation is solved. The effect of electrochemical reactions on water species and flow was implemented through uniform source terms in the channels. The model could show liquid water distribution in the gas channels matching with experimentally found liquid water distribution. The extent of GDL intrusion could be calculated using numerical experiment also.

This stand-alone numerical model is then attached to the PEFC model, resulting in a complete three dimensional non-isothermal two-phase model for PEFC. The same model is used in the anode gas channels also. Wetted area of the GDL channel interface and pressure drop in the cathode side were validated for a wide range of parameters (inlet relative humidity, stoichiometry, average current density). The simulations were in good agreement with experiments. As a result of GDL intrusion the edge channels exhibit much higher liquid water and GDL over these channels are almost totally wet. But maximum liquid water could be found near the middle portion of the cell. This indicates that much less reaction is taking place in the catalyst layer over the edge channels, as the ability of the edge channels to transport is lower – liquid water once in these channels can not be flushed out. This conjecture was supported by the current density distribution in the membrane, which showed much less current over the intruded edge channels. This non-uniform catalyst utilization is due to limitation in reactant and product flow. At low stoichiometry operations this can lead to reactant starvation and ultimately corrosion of carbon support.

In a PEFC it is known that phase-change takes place but till now no effort has been made to investigate this phenomenon. A two-phase, non-isothermal model based on M^2 philosophy was used to study phase-change rate in the cathode GDL of a PEFC. In the cathode GDL condensation takes place under the cooler bipolar plate surface and evaporation takes place under the channel. Inlet relative humidity and GDL thermal conductivity are the two key factors controlling the phase-change rate. At lower inlet relative humidity phase change takes place near the middle of the channel. At lower GDL thermal conductivity the catalyst layer temperature increases while the bipolar plate

remains cool as it transports same amount of heat. Therefore the phase-change rate increases under the cooler land surface. This indicates a stronger “Heat-Pipe Effect” in the cathode GDL. Under these conditions a much higher fraction of total heat transfer occurs through phase change.

With the full PEFC model in steady state in hand the next logical step would be unsteady computation. Then, effect of two-phase flow in the channels could be studied over transients. Since the steady model is computationally expensive better computational schemes are necessary to make unsteady computation economical.

The present model gives an average liquid volume fraction in the channel while experiments suggest different flow regimes in channel e.g. mist, film, slug and annular. The present model can not differentiate between these flow regimes and the gas-liquid interface cannot be resolved. Therefore level-set methods could be applied to the channel two-phase flow to resolve the actual gas-liquid interface.

References

1. Frano Barbir, “PEM Fuel Cells: Theory and Practice”, Elsevier Academic Press, 2005.

2. Ryan O’Hayre, Suk-Won Cha, Whitney Colella and Fritz B. Prinz, “Fuel Cell Fundamentals”, John Wiley & Sons, 2006.

3. James Larminie and Andrew Dicks, “Fuel Cell Systems Explained”, Second Edition, John Wiley & Sons, 2003.

4. C.Y. Wang, *Chemical Reviews*, Vol. 104, pp4727-4766, 2004.

5. D.M. Bernardi, and M.W. Verbrugge, *J. Electrochemical Soc.,* vol. 139, pp. 2477 (1992).

6. T.E. Springer et al., *J. Electrochemical Soc.*, vol. 138, pp. 2334-2341 (1991).

7. T.E. Springer et al., *J. Electrochemical Soc.*, vol. 140, pp. 3513 (1993).

8. T.F. Fuller, and J. Newman, *J. Electrochemical Soc.,* vol. 140, pp. 1218 (1993).

9. T.F. Fuller, and J. Newman, in *Proceeedings of the Symposium on Fuel Cells, R.E. White and A. J. Appleby,* Editors, PV 89-14, pp. 25, The Electrochemical Society Proceedings Series, NJ (1989).

10. T.F. Fuller, and J. Newman, *ibid,* vol. 139, pp. 1332 (1989).

11. T.F. Fuller, *Ph.D. Thesis*, University of California Berkeley, CA (1992).

12. T.V. Nguyen, and R.E. White, *J. Electrochemical Soc.*, vol. 140, pp. 2178 (1993).

13. T.V. Nguyen, J. Hedstrom, and N. Vanderborgh, in *Proceeedings of the Symposium on Fuel Cells, R.E. White and A. J. Appleby,* Editors, PV 89-14, pp. 39, The Electrochemical Society Proceedings Series, NJ (1989).

14. S. Um and C. Y. Wang, *in Proc. of the ASME Heat Transfer Division*, Orlando, FL., Nov. 2000.

15. S. Um, C. Y. Wang and K. S. Chen, *J. of Electrochemical Soc.*, vol.147, pp4485 (2000).

16. S. Dutta, S. Shimpalee, and J.W. Van Zee, *Int. J. of Heat and Mass Transfer,* vol. 44, pp. 2029 (2001).

17. S. Dutta, S. Shimpalee, and J.W. Van Zee, *J. Appl. Electrochem.,*vol. 30, pp. 135 (2000).

18. F. Buchi and G.G. Scherer, *J. Electrochemical Soc.*, vol. 148, pp. A183 (2001).

19. A.A. Kulikovsky, *J. Electrochemical Soc.*, vol. 150, pp. A1432 (2003).

20. H. Meng and C. Y. Wang, *Chemical Engineering Science*, vol. 59, ppA3331 (2004).

21. U. Pasaogullari, and C. Y. Wang**,** *Electrochimica Acta*, vol. 49, pp4359 (2004).

22. X.G. Yang, F.Y. Zhang, A. Lubawy and C.Y. Wang, *Electrochemical & Solid-State Letters*, ppA408 (2004).

23. F. Y. Zhang, X. G. Wang and C. Y. Wang, *J. of Electrochemical Soc.*, vol. 153, pp. A225 (2006).

24. Z.H. Wang, C. Y. Wang and K. S. Chen, *J. Power Sources*, vol. 94 (1), pp. 40 (2001).

25. D. Natarajan, and T.V. Nguyen, *J. of Electrochemical Soc.*, vol. 148, pp. 1324 (2001).

26. J. H. Nam and M. Kaviany, *Int. J. Heat and Mass Transfer,* vol. 46, pp. 4595 (2003).

27. S. Mazumder and J.V. Cole, *J. of Electrochemical Soc.*, vol. 150, pp. A1510 (2003).

28. U. Pasaogullari and C.Y. Wang, *J. of Electrochemical Soc.*, vol.152, pp.A380 (2005).

29. E. Bigersson, M. Noponen and M. Vynnycky, *J. of Electrochemical Soc.*, vol.152, pp.A1021 (2005).

30. H. Meng and C.Y. Wang, *Journal of Electrochemical Society*, vol. 152, pp. A1733 (2005).

31. Y. Wang and C. Y. Wang, *Journal of Electrochemical Society*, vol. 153, pp. A1193 (2006).

32. K. Promislow, J. Stockie and B. Wetton, *Proc. R. Soc. A,* vol. 462, pp. 789, (2006).

33. S. Maharudrayya, S. Jayanti, A.P. Deshpande, *Journal of Power Sources*, Vol. 144, pp 94-106 (2005).

34. Eon Soo Lee et. al. , *Proceedings of FEDSM 2005, ASME Fluids Engineering Division Summer Meeting and Exhibition*, June 19 –23,2005, Houston ,Texas, USA.

35. F.Barrears, A. Lozano, L. Valiano, C. Marin, A. Pascau, *Journal of Power Sources*, Vol. 144, pp.54-66 (2005).

36. M. Chaouche, N. Rakotomalala, D. Salin and Y.C. Yortos, *Europhysics Letters,* vol. 21, pp. 19 (1993).

37. D. Or and M. Tuller, *Advances in Water Resources,* vol. 26, pp. 883 (2003).

38. C.Y. Wang, M. Groll, S. Rosler and C.J. Tu, *Heat Recovery System and CHP*, Vol. 14, No. 4, pp. 377-389,1994.

39. W.L. Olbricht, *Ann. Rev. Fluid Mech.*, Vol.28, pp.187-213, 1996.

40. U. Imke, *Chem. Eng. J.*, Vol.101, pp.295-302, 2004.

41. C.Y. Wang and P. Cheng, *Int. J. Heat Mass Transfer*, Vol.39, pp.3607-3618, 1996.

42. P. Cheng and C.Y. Wang, *Int. J. Heat Mass Transfer*, vol.39, pp.3619-3632, 1996.

43. A.E. Saez and R.G. Carbonell, *AIChE Journal*, vol . 31, pp.52-62, 1985.

44. F.A. Dullien, *Porous Media – Fluid Transport and Pore Structure*, 2nd Edition, pp. 373-378, Academic Press, 1992.

45. R. H. Brooks and A.T. Corey, *Hydrology Papers, Colorado State University*, vol. 3, 1964.

46. Y. Wang, Suman Basu, C.Y. Wang, *Journal of Power Sources,* Vol. 179, pp. 603-617, 2008.

47. J.M. Yin, C.W. Bullard and P. S. Hrnjak, *Heat Transfer Engineering*, vol. 23, pp 3, 2002.

48. K.A. Triplett, S.M. Ghiaasiaan, S.I. Abdel-Khalik, D.I. Sadowski, *International Journal of Multiphase Flow*, vol. 25, pp 377, 1999.

49. C.A. Damiandes and J.W. Westwater, Glasgow, 14 – 16 September, *Mechanical Engineering Publications*, London, pp. 1257, 1988.

50. T. Fukano and A Kariysaki, *Nuclear Engineering Des*., vol. 141, pp 59-68 (1993).

51. K.A. Triplett, S.M. Ghiaasiaan, S.I. Abdel-Khalik, A. Lemouel, B.N.McCord, *International Journal of Multiphase Flow*, vol. 25, pp 395, 1999.

52. G. Hestroni, A. Mosyak, Z. Segal and E.Pogrebnyak, *International Journal of Multiphase Flow*, vol. 29, pp. 341, 2002.

53. L. Jiang, M. Wong and Y. Zohar, *Journal of Microelectromechanical systems*, vol. 10, pp. 80, 2001.

54. S.G. Kandlikar, *Experimental Thermal Fluid Science*, vol. 26, pp. 389, 2002.

55. Prabhu Balasubramaniam and S.G. Kandlikar, *Heat Transfer Engineering*, vol. 26 (3), pp. 20, 2005.

56. S.G. Kandlikar and P. Balasubramniam, *Transaction of the ASME*, vol. 127, pp 820, 2005.

57. J. Lee and I. Mudawar, *International Journal of Heat and Mass transfer*, vol. 48, pp 928, 2005.

58. Pega Hrnjak, *Heat Transfer Engineering*, vol. 25(3), pp61, 2004.

59. Ralph L. Webb and Kilyoan Chung, *Heat Transfer Engineering*, vol. 26 (4), pp 3, 2005.

60. T. Chiba and T. Toshihara, U.S. Patent No. 5,979,547, 1999.

61. R. Haussman, U.S. Patent No. 6,199,401 B1, 2001.

62. C.Y. Wang, W.B. Gu, and B.Y. Liaw, *Journal of the Electrochemical Society*, **145**(10), pp. 3407, 1998.

63. H. Meng, *Journal of Power Sources*, vol. 168(1), pp. 218, 2007.

64. L. J. Bridge, PhD Thesis, University of British Columbia, September 2, 2006.

65. Y. Wang and C. Y. Wang, vol. 154(7), pp. B636, 2007.

66. K. Pruess, J. S. Y. Wang, and Y.W. Tsang, *Water Resources Research*, vol. 26 (6), pp. 1235, 1990.

67. S. Basu, C.Y. Wang and K.S. Chen, *ASME Journal of Fuel Cell Science and Technology*, in press (2008).

68. H. Meng and C.Y. Wang, *Journal of the Electrochemical Society*, vol. 151, pp. A358, (2004).

69. H. Ju, G. Luo and C. Y. Wang, *Journal of the Electrochemical Society*, vol. 154(2), pp. B218, 2007.

70. T. Berning and N. Djlali, *Journal of the Electrochemical Society*, vol. 150, pp. 1589 (2003).

71. U. Pasaogullari, and C. Y. Wang, *Journal of the Electrochemical Society*, vol. 151, ppA399 (2004).

72. I.S. Hussaini , *Personal Communications*.

73. G. Luo, H. Ju, and C. Y. Wang, *Journal of the Electrochemical Society*, vol. 154(2), pp. B316, 2007.

74. Y. Wang, and C. Y. Wang, *Journal of the Electrochemical Society*, vol. 152 (2), pp. A445, 2005.

75. S. Basu, C.Y. Wang and K.S. Chen, *Proceedings of Fuel Cell 08, 6th International Fuel Cell Science, Engineering and Technology Conference,* June 16-18, 2008, Denver, Colorado, USA.

76. G.Q.Lu, F.Q. Liu and C.Y. Wang, *Journal of Power Sources*, vol. 164, pp. 134, 2007.

77. J. Li, C.Y. Wang and A. Su, *Journal of the Electrochemical Society*, vol. 155(1), pp. B64, 2008.

VITA

Suman Basu

Suman Basu was born to Mr. Shyamal Kumar Basu and Mrs. Kumkum Basu on December 2nd 1978 in Kolkata, India. He received his undergraduate degree in Mechanical engineering from Jadavpur University, Kolkata in 2001. Subsequently he did his Master's in Mechanical Engineering from Indian Institute of Technology, Kanpur in 2003 and joined Fluent India Pvt. Ltd. in Pune, India. In 2005 he joined the Pennsylvania State University to pursue PhD in Mechanical Engineering and has since been working in the area of numerical modeling of two-phase flow and phase change in polymer electrolyte fuel cells.